Loop Optimization of Tensor Network Renormalization: Algorithms and Applications

by

Chenfeng Bao

A thesis
presented to the University of Waterloo
in fulfillment of the
thesis requirement for the degree of
Doctor of Philosophy
in
Physics

Waterloo, Ontario, Canada, 2019

© Chenfeng Bao 2019

Examining Committee Membership

The following served on the Examining Committee for this thesis. The decision of the Examining Committee is by majority vote.

External Examiner:	Erik Sorensen Professor, Department of Physics and Astronomy, McMaster University
Supervisor(s):	Neil Turok Adjunct Professor, Department of Physics and Astronomy, University of Waterloo
Internal Member:	Roger Melko Professor, Department of Physics and Astronomy, University of Waterloo
Internal-External Member:	David Gosset Associate Professor, Department of Combinatorics and Optimization, University of Waterloo
Other Member(s):	Anton Burkov Professor, Department of Physics and Astronomy, University of Waterloo

This thesis consists of material all of which I authored or co-authored: see Statement of Contributions included in the thesis. This is a true copy of the thesis, including any required final revisions, as accepted by my examiners. I understand that my thesis may be made electronically available to the public.

Statement of Contributions

Chapter 3 and Appendix D of this thesis consists of material from Reference [5], co-authored with Shuo Yang, Chenjie Wang, and Zheng-Cheng Gu.

Abstract

Loop optimization for tensor network renormalization (loop-TNR) is a real-space renormalization group algorithm suitable for studying 1+1D critical systems. While the original proposal by Yang *et al.* focused on classical models, we extend this algorithm with new techniques to enable accurate and efficient extraction of conformal data from critical quantum models. Benchmark results are provided for a number of quantum models, including ones described by non-minimal or non-unitary conformal field theories, showcasing both the strengths and limitations of loop-TNR. We discuss the subtle issue of non-analytic finite size effect in quantum lattice models and its impact on loop-TNR, and propose the use of virtual-space transfer-matrix to circumvent it, using the XY model as a demonstration. We then generalize loop-TNR to fermionic systems by incorporating Grassmann numbers, and benchmark the generalized algorithm on the t-V model.

Next, we demonstrate a non-trivial application of loop-TNR by studying the 1D domain wall between untwisted and twisted 2D lattice gauge theories of finite groups G. We numerically study such domain walls for $G = \mathbb{Z}_N$ (with $N < 6$) using loop-TNR, and discover a large class of gapless models. We also study the physical mechanism for these gapless domain walls and propose quantum field theory descriptions that agree perfectly with our numerical results. By taking advantage of the classification and construction of twisted gauge models using group cohomology theory, we systematically construct general lattice models to realize gapless domain walls for arbitrary finite symmetry group G. Such constructions can be generalized into arbitrary dimensions and might provide us a systematical way to study gapless domain walls and topological quantum phase transitions.

Acknowledgements

I thank Zheng-Cheng Gu for his invaluable supervision on this entire research project. His guidance, which goes all the way back to 2012, provided crucial research directions, especially on the work presented in Chapter 3. His deep physical insight opened my eyes to exciting fields of research and helped me a great deal with my study. His patience and encouragement helped me get through my low points.

I thank Shuo Yang and Chenjie Wang for their collaboration and helpful discussions that lead to the breakthrough in Chapter 3 after years of work. I also thank A. W. W. Ludwig, D. N. Sheng and Davide Gaiotto for early collaboration in this work. I thank my advisory committee members Neil Turok, Roger Melko, and Sung-Sik Lee for their valuable feedback.

I thank Perimeter Institute for the excellent work environment.

Thank you, my parents, for your constant support and care over the years. Thank you, Renfang, for being the sunshine in my life.

Table of Contents

List of Tables ix

List of Figures x

1 Introduction 1

1.1 Tensor networks . . . 3

1.2 Tensor network renormalization group . . . 4

2 Algorithms 9

2.1 Review of the loop-TNR algorithm . . . 9

2.2 Discretizing Euclidean time path integral . . . 12

2.3 Transfer matrix and conformal data . . . 15

2.3.1 Central charge and scaling dimensions . . . 15

2.3.2 Spins . . . 17

2.3.3 Computational considerations . . . 18

2.4 Benchmark results . . . 19

2.5 Non-analytic finite size effects and virtual-space transfer matrix . . . 25

2.6 Extension to fermionic systems . . . 29

2.6.1 Fermion coherent state path integral . . . 29

2.6.2 Grassmann tensor network renormalization . . . 31

2.6.3 Benchmark results . . . 33

3 Application: Gapless domain walls between topological phases **35**
3.1 Introduction . . . 35
3.2 A simple example: gapless domain wall between $\mathbb{Z}_2$ gauge model and twisted $\mathbb{Z}_2$ gauge model . . . 38
3.2.1 $\mathbb{Z}_2$ gauge model and twisted $\mathbb{Z}_2$ gauge model . . . 38
3.2.2 Operator algebra for the domain wall between toric code model and double semion model . . . 40
3.2.3 Gauge fixing and connections to domain wall models between SPT phases . . . 42
3.2.4 Effective Hamiltonian with the same operator algebra . . . 43
3.2.5 Numerical calculations . . . 45
3.2.6 A physical picture for the gapless nature of the domain wall . . . 48
3.3 Constructing lattice models of general gapless domain walls . . . 51
3.3.1 Constructing SPT phases using group cocycles . . . 51
3.3.2 Domain walls between general SPT phases . . . 52
3.3.3 $\mathbb{Z}_N$ domain wall models . . . 54
3.4 Conclusions and discussions . . . 63

Outlook **64**

References **65**

APPENDICES **72**

A Review of MPS algorithms **73**

B Calculus of Grassmann tensors **78**

C Group cohomology and bosonic SPT phases **81**
C.1 Algebraic definition of group cohomology . . . 81
C.2 Constructing bosonic SPT phases using group cohomology . . . 82

D Energy spectrum of Luttinger liquid theory **85**

List of Tables

2.1 Scaling dimensions of the Ising CFT 20

3.1 Best fit Luttinger liquid parameters for $\mathbb{Z}_N$ domain walls 58

3.2 Best fit Luttinger liquid parameters for $\mathbb{Z}_3$ domain walls 62

List of Figures

1.1 Examples of simple tensor network diagrams. 4
1.2 Block spin RG compared with TNRG 6
1.3 Tensor renormalization group 6
1.4 Corner double line tensors 8

2.1 Loop-TNR entanglement filtering 10
2.2 Basic loop-TNR 11
2.3 Tensor networks of a Euclidean path integral 14
2.4 2D CFT spacetime geometry 16
2.5 Spacetime geometry of successive renormalized tensors 18
2.6 Loop-TNR results for the Ising model 21
2.7 Loop-TNR results for the XY model 21
2.8 Loop-TNR results for the XXZ model 23
2.9 Loop-TNR results for the Haldane chain 24
2.10 Locations and conformal data of the Yang-Lee singularity 25
2.11 Spectrum of the XY model under different transverse field 27
2.12 Energies of the XY model vs. system size 28
2.13 Grassmann tensor networks for fermionic path integrals 31
2.14 Transfer matrices of a fermionic system 32
2.15 Loop-GTNR results for the t-V model 34

3.1 The toric code model and doubled semion model 39
3.2 Untwisted and twisted $\mathbb{Z}_2$ gauge models 41
3.3 Domain walls between topological phases 41
3.4 $\mathbb{Z}_2$ SPT models 43
3.5 Spectra of the Ising domain wall and the XXX model 45
3.6 Central charge and scaling dimensions of the Ising domain wall and the XXX model 47
3.7 Scaling dimensions of deformed Ising domain wall models 49
3.8 A triangular lattice with a branching structure 53
3.9 The domain wall of two SPT phases 54
3.10 Ground state entanglement entropy of $\mathbb{Z}_N$ domain wall models 56
3.11 Virtual energies of $\mathbb{Z}_N$ domain wall models 57
3.12 Virtual energies of deformed $\mathbb{Z}_3$ domain walls 59
3.13 An alternative branching structure on the domain wall. 59
3.14 Virtual energies of the $\mathbb{Z}_3$ domain wall model with alternative branching structure 61
3.15 Scaling dimensions of $\mathbb{Z}_2$ domain walls with random 3-coboundaries 61
3.16 Virtual energies of $\mathbb{Z}_3$ domain walls with random 3-coboundaries 62

A.1 MPS canonicalization 74

B.1 Grassmann tensor contractions 79

C.1 The graphical representation of an SPT ground state wave function 83
C.2 A lattice model for 2-dimensional SPT phase 84

Chapter 1

Introduction

The renormalization group (RG) is a powerful framework relating physical theories at different energy scales. It is a crucial concept in modern physics that reshaped our understanding of quantum field theory and statistical physics. Early ideas of RG appeared in the mid 20th century in both high energy physics and condensed matter physics, and the development culminated in Wilson's formulation [90] in the 1970s. At the core of RG is the observation that physical phenomena at low energy scale are insensitive to physics at high energy scale. A low energy effective theory can thus be constructed from its corresponding high energy theory or microscopic model by iteratively integrating out high energy degrees of freedom. What results is a flow diagram, the "RG flow", in an abstract theory space, connecting different effective theories at different energy scales. Fixed points in the RG flow explains universality (the striking coincidence of critical exponents in very disparate systems), and is foundational to our modern understanding of phase transition and critical behaviours. In high energy physics, the concept of RG flow is used to predict the systematic changing of interactions at different energy scales, and provides a more solid foundation for quantum field theory as an effective theory.

In the early days, Wilson's RG scheme was typically formulated in momentum space, and was performed by integrating out the so-called fast modes in a momentum shell. After a scale transformation for the slow modes and a proper field redefinition, the RG flow of a coupling constant can be computed by using perturbation theory and Feynman diagrams. Although Wilson's scheme is extremely powerful within the weak coupling limit, it does not give rise to any meaningful predictions for strong coupling physics. In recent decades, discoveries in condensed matter physics such as the fractional quantum Hall effect [73] have highlighted how exotic collective behaviours like fractionalization can arise from many strongly-interacting constituents. They have also brought attention to the inadequacy of

conventional weak coupling theories. Therefore, a non-perturbative RG scheme has been widely sought over the past decades as a new theoretical tool to study strongly-correlated systems.

Because most interactions are local in real space, the concept of real-space RG is very attractive for systems with strong interactions. The history of real-space RG can be traced back to the block spin RG scheme first proposed by Leo P. Kadanoff half a century ago [40]. The basic idea of block spin RG is to use the so-called block spin to describe the physical degrees of freedom for a coarse-grained system, and to compute the effective interactions among block spins. Even for strong interactions, the block spin RG scheme can capture the basic physics and allow us to compute the phase transition point approximately. Unfortunately, at a critical point, due to the divergence of correlation lengths, infinite long-range interactions among block spins will be generated, making it impossible to calculate critical exponents accurately.

To overcome shortcomings of the traditional Wilson-Kadanoff RG scheme, Wilson developed a new scheme, the so-called numerical RG (NRG), which selects and keeps only the most relevant low-energy subspace using numerical exact diagonalization. This successfully resolved the Kondo problem [91] and Wilson was awarded the Nobel Prize for his elegant idea. However, it was later realized that NRG is flawed in its treatment of boundaries [89], making accurate results unachievable for generic quantum models. About three decades ago, Steve White proposed a generalization of NRG, replacing the selection of the most relevant low-energy subspace with the most relevant subspace of the reduced density matrix for a subsystem. This new algorithm - the so-called density matrix renormalization group (DMRG) algorithm [87] - solved the boundary condition problem in NRG, and became the best numerical algorithm to study quantum systems with strong interactions, especially for 1+1D gapped systems.

More recently, an influx of ideas from quantum information into condensed matter physics brought us a whole class of variational ansatz known as tensor network states [61]. A quantum information analysis of DMRG pointed out that it is equivalent to using one particular class of tensor network states - the matrix product state (MPS) [78]. Remarkably, it was rigorously proved that the ground state of all 1+1D gapped quantum systems can be faithfully represented as an MPS with a finite bound dimension proportional to the correlation length of the system [77]. More generally, the effectiveness and limitations of tensor network states can be (partially) explained as the area law of entanglement entropy [19] started to be understood. This new understanding in turn enabled constructions of new tensor network states such as multiscale entanglement renormalization ansatz (MERA) [80]. MERA introduced RG to the domain of quantum entanglement and proves to be an efficient ansatz for gapless 1+1D systems.

Tensor networks are used to directly implement a real-space RG scheme when Levin and Nave proposed tensor renormalization group (TRG) [50]. Its core idea is to represent the partition function or path integral of a many-body system as a tensor network, and iteratively coarse grain the network to approximately encode local degrees of freedom of an larger and larger area into a single (or just a few) tensor(s). The result is the construction of an RG flow in the space of tensors, which will eventually reach a fixed point that is a tensor capturing the low energy physics of the system in the thermodynamic limit. This approach promises to be an efficient and accurate way to implement real-space RG, and received many improvements, extensions, and variations in the following years [16, 17, 20, 25, 27, 27, 29, 35, 36, 95–97], spawning a mini-field of tensor network renormalization group (TNRG)[1]. TNRG algorithms and ideas have been successfully applied to study problems in condensed matter physics [26, 52, 65, 66, 72, 82] and even quantum gravity [14, 15, 18].

In this thesis, we will look closely at one variant of TNRG - loop optimization of tensor network renormalization (loop-TNR) [97]. In the remainder of this chapter, we introduce some basic concepts of tensor networks and TNRG. In Chapter 2, we discuss algorithmic details of loop-TNR, especially when applied to quantum (including fermionic) systems. In Chapter 3, we apply loop-TNR to study and construct models of gapless domain walls between topological phases.

1.1 Tensor networks

A tensor network is a collection of many contracted small tensors representing one large tensor. When used to represent the coefficient tensor of a quantum state (operator), they are referred to as tensor network states (operators). The most famous tensor network state is the matrix product state (MPS)

$$\langle\{l_n\}|\Psi\rangle \equiv \Psi_{\{l_n\}} = \sum_{\{i_n=1,\ldots,\chi_n\}} A^1_{i_0 l_1 i_1} A^2_{i_1 l_2 i_2} \ldots . \tag{1.1}$$

It is customary to represent such expressions in diagrams. We represent each rank[2]-r tensor by a solid shape with r lines attached to it. Each line represents an index, and is often called a bond or a leg. Legs are connected whenever indices are contracted. Each free end

[1] We use the term TNRG to refer to the general class of algorithms that implement real-space RG using tensor networks, whereas similar terms like TRG or tensor network renormalization (TNR) are reserved for specific algorithms by convention in the literature.

[2] When talking about the "rank" of a tensor, we mean the number of indices the tensor has, not to be confused with the dimension of a linear operator's image.

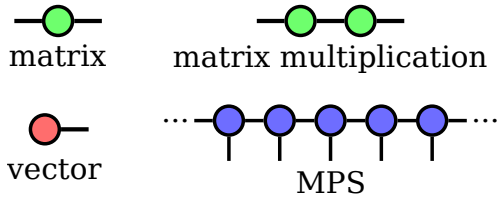

Figure 1.1: Examples of simple tensor network diagrams.

of a leg represents a free uncontracted index. Following these rules, we draw the diagrams of MPS and some other simple tensors in Fig. 1.1. We call the contracted internal bonds (i_n's) virtual bonds, and uncontracted external bonds (l_n's) physical bonds. The range of an index is referred as the bond dimension, usually denoted by χ.

For a given tensor, the set of tensors in a particular tensor network decomposition scheme is not unique, because we can always insert pairs of inverse matrices in-between neighbouring tensors. Take the MPS for example,

$$\begin{aligned}\Psi_{\{l_n\}} &= \sum_{\{i_n\}} \dots A^m_{i_{m-1}l_m i_m} A^{m+1}_{i_m l_{m+1} i_{m+1}} \dots \\ &= \sum_{\{i_n\}} \sum_{i'_m p} \dots A^m_{i_{m-1}l_m i_m} B_{i_m p} B^{-1}_{p i'_m} A^{m+1}_{i'_m l_{m+1} i_{m+1}} \dots .\end{aligned} \tag{1.2}$$

We can then use $\widetilde{\mathbf{A}}^m \equiv \mathbf{A}^m \cdot \mathbf{B}$ and $\widetilde{\mathbf{A}}^{m+1} \equiv \mathbf{B}^{-1} \cdot \mathbf{A}^{m+1}$ in place of $\mathbf{A}^m$ and $\mathbf{A}^{m+1}$ to get the same $\mathbf{\Psi}$. This freedom is generally refereed to as the gauge freedom of a tensor network. It is often utilized to transform a tensor network into a more suitable or efficient form.

A high rank tensor can be alternatively viewed as a matrix (vector), if its indices are grouped into two (one) groups each acting like a single index. We will denote this by putting indices in the same group into parentheses, e.g. we can view the rank-4 tensor T_{ijkl} as a matrix $T_{(ij)(kl)}$ or $T_{i,(jkl)}$ etc.

1.2 Tensor network renormalization group

A TNRG algorithm is one that implements a real-space RG scheme using tensor networks. To introduce the general workings of TNRG, we shall compare it with the original real-space RG method - block spin RG [40, 60].

Consider a 2D classical system of spins $\{s_i\}$ with Hamiltonian $H(\{s_i\})$. A block spin RG transformation $\mathcal{R}$ replaces each local block of a few spins with a single effective spin s'_i (Fig. 1.2a,b), and finds an effective Hamiltonian

$$H'(\{s'_i\}) \equiv \mathcal{R}[H(\{s_i\})] \tag{1.3}$$

such that partition functions computed from H and H' are as close as possible

$$Z = \sum_{\{s_i\}} e^{-\beta H} \approx \sum_{\{s'_i\}} e^{-\beta H'}. \tag{1.4}$$

TNRG starts by representing the partition function as the tensor trace of a tensor network (Fig. 1.2c)

$$Z = \mathrm{tTr} \otimes_i \mathbf{T}, \tag{1.5}$$

then implements an RG transformation by finding new tensors

$$\mathbf{T}' \equiv \mathcal{R}(\mathbf{T}) \tag{1.6}$$

such that a smaller network of them reconstructs the original partition $Z \approx \mathrm{tTr} \otimes_i \mathbf{T}'$ as close as possible (Fig. 1.2c-e). Repeatedly applying $\mathcal{R}$ should lead to a fixed point Hamiltonian (for block spin RG) or tensor (for TNRG) that encodes macroscopic properties or critical behaviours of the system.

Block spin RG generally assumes that each renormalized effective spin s'_i has the same degrees of freedom as an original spin s_i, but has no inherent restrictions on the range of interactions a renormalized Hamiltonian H' can have. In contrast, in TNRG, renormalized spin live on links between tensors (Fig. 1.2c-e), whose degrees of freedom can grow freely with the bond dimension χ of tensors, but interactions are limited to a very short range by nature of the tensor network's geometry. In practical implementations, both block spin RG and TNRG have limited spin degrees of freedom (bond dimension χ) and limited interaction range, which introduce approximation errors. However, progressively increasing the bond dimension of tensors in TNRG is straightforward, and much simpler than increasing interactions range in block spin RG (which basically requires redesigning the algorithm). The flexibility of tensor networks also makes TNRG more adaptable to quantum systems (by using Suzuki-Trotter expansion[69]) and easier to improve.

In the original TRG algorithm, a square tensor network is first deformed into a square-octagon lattice by decomposing each local tensor into two rank-3 tensors using truncated

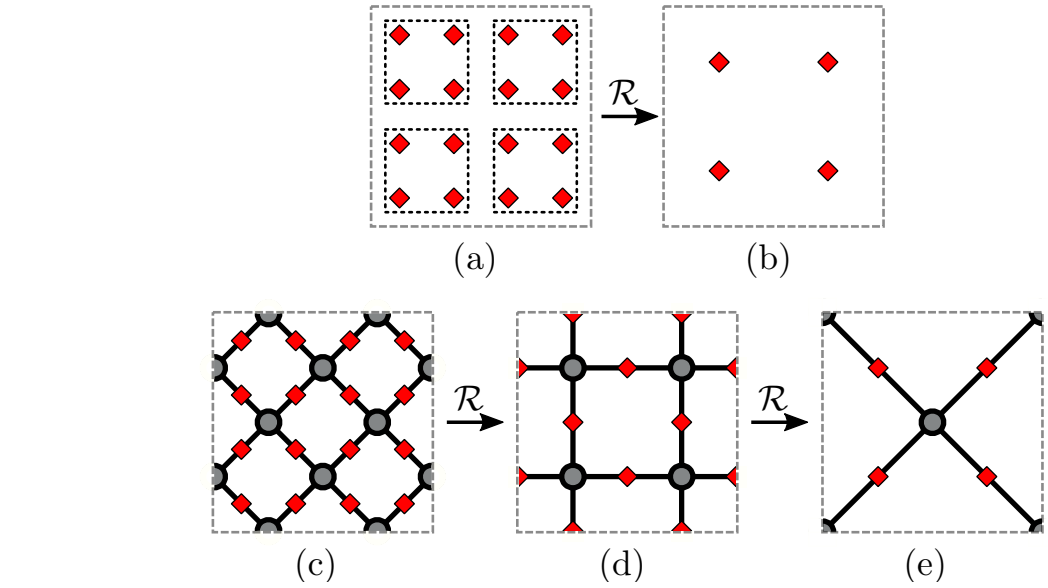

Figure 1.2: Comparison of block spin RG (a-b) and TNRG (c-e) on a region of 4×4 spins. Red diamonds represent spins, and grey circles represent tensors in TNRG.

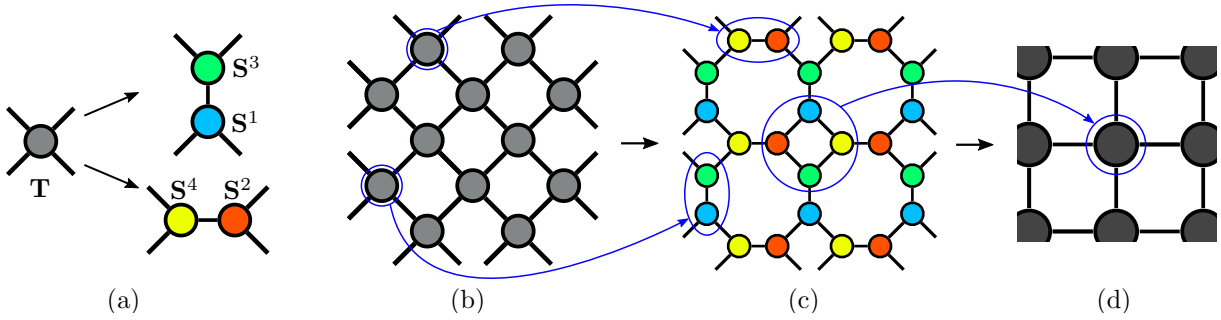

Figure 1.3: (a) Tensor decomposition using SVD. (b) A square tensor network representation of the partition function of a 2D classical system. (c) A square-octagon tensor network obtained from a square network by decompositions. (d) A coarse-grained square tensor network.

singular value decomposition (SVD) (Fig. 1.3a), i.e.

$$
\begin{aligned}
T_{ruld} \equiv M^a_{(ru)(ld)} \overset{\text{SVD}}{=\!=} \sum_i U^a_{(ru)i} \Lambda^a_i [V^a_{(ld)i}]^*, \quad T_{ruld} \equiv M^b_{(ul)(dr)} \overset{\text{SVD}}{=\!=} \sum_i U^b_{(ul)i} \Lambda^b_i [V^b_{(dr)i}]^*, \\
S^3_{rui} \equiv U^a_{(ru)i} \sqrt{\Lambda^a_i}, \quad S^1_{ldi} \equiv \sqrt{\Lambda^a_i} [V^a_{(ld)i}]^* \quad \text{for } i \leq \chi, \\
S^4_{uli} \equiv U^b_{(ul)i} \sqrt{\Lambda^b_i}, \quad S^2_{dri} \equiv \sqrt{\Lambda^b_i} [V^b_{(dr)i}]^* \quad \text{for } i \leq \chi,
\end{aligned}
\tag{1.7}
$$

where $\{\Lambda^a\}$ and $\{\Lambda^b\}$ are sorted in descending order, so that

$$
T_{ruld} \approx \sum_i S^3_{rui} S^1_{ldi}, \quad T_{ruld} \approx \sum_i S^4_{uli} S^2_{dri} \tag{1.8}
$$

is an optimal solution to the cost function

$$
E = \left\| \mathbf{T} - \mathbf{S}^3 \cdot \mathbf{S}^1 \right\|^2 \quad \text{and} \quad E = \left\| \mathbf{T} - \mathbf{S}^4 \cdot \mathbf{S}^2 \right\|^2 \tag{1.9}
$$

under the constraint that all bond dimensions are no larger than χ. Then a new rank-4 tensor $\mathbf{T}'$ is built by contracting four $\mathbf{S}$ tensors (Fig. 1.3d), halving the number of tensors in the network compared to the original. This simple algorithm is very efficient with a computational cost of only $\mathcal{O}(\chi^5)$. It can effectively squeeze local correlation / entanglement of a non-critical system into a small fixed point tensor and reveal the structure of its low energy physics.

One of TRG's limitations is its lack of entanglement filtering, and as a result, its fixed point tensors are not unique. Notably, TRG cannot simplify a tensor of the corner double line form

$$
T^{\text{CDL}}_{ruld} \equiv T_{(r_1 r_2)(u_1 u_2)(l_1 l_2)(d_1 d_2)} = M^1_{r_2 u_1} M^2_{u_2 l_1} M^3_{l_2 d_1} M^4_{d_2 r_1}, \tag{1.10}
$$

whereas we can see by inspecting the diagram in Fig. 1.4 that a tensor network composed of corner double line tensors should simplify to a product of scalars. This limitation is addressed by tensor entanglement filtering renormalization (TEFR) [29], which can correctly simplify CDL tensors and effectively eliminate local entanglement of non-critical systems to produce unique (up to gauge freedom) fixed point tensors. This improvement allows TEFR to be an important tool in the discovery of symmetry protected topological (SPT) phases [29].

Further improvement in techniques of entanglement filtering leads to the development of tensor network renormalization (TNR) [20] and loop-TNR [97]. These new algorithms are able to effectively filter entanglement and produce semi-stable fixed point tensors even for critical systems. As we will see in Chapter 3, this advancement enables loop-TNR to be the central tool in our identification and construction of gapless domain wall between 2+1D topological phases.

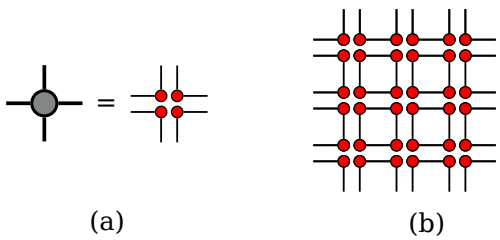

Figure 1.4: (a) A corner double line tensor. (b) A tensor network composed of CDL tensors, whose internal closed loops can be simplified to scalars.

Chapter 2

Algorithms

Loop-TNR is a TNRG algorithm that can effectively filter out local correlation/entanglement in both non-critical and critical 2D classical and 1+1D quantum lattice systems. It can produce a semi-stable fixed point tensor from which we can extract the conformal data of the underlying conformal field theory (CFT) describing the low energy physics of critical systems. However, earlier literature on loop-TNR and TNRG methods in general focused mostly on classical systems and minimal models when it comes to extracting conformal data, with limited algorithmic details and few benchmark results on quantum systems. In this chapter, we discuss the algorithmic details of applying loop-TNR to 1+1D quantum systems. We start with a review of loop-TNR in its simplest form in Sec. 2.1. In Sec. 2.2, we discuss how to represent the path integral of a quantum system as an isotropic tensor network. In Sec. 2.3, we explain the details of extracting conformal data from a transfer matrix, especially how the spacetime geometry of a quantum system can be determined, and how a non-rectangular geometry can be utilized to efficiently compute conformal spins. In Sec. 2.5, we address the subtle issue of non-analytic finite size effects only present in quantum systems and methods to avoid it. In Sec. 2.6, we extend loop-TNR to fermionic systems with the introduction of Grassmann numbers. Finally, we provide benchmark results on some more interesting quantum models in Sec. 2.4.

2.1 Review of the loop-TNR algorithm

Given a 2D square tensor network with bond dimensions at most χ, and assuming it is formed with by at most two different types of tensors $\mathbf{T}^a, \mathbf{T}^b$ on two square sub-lattices

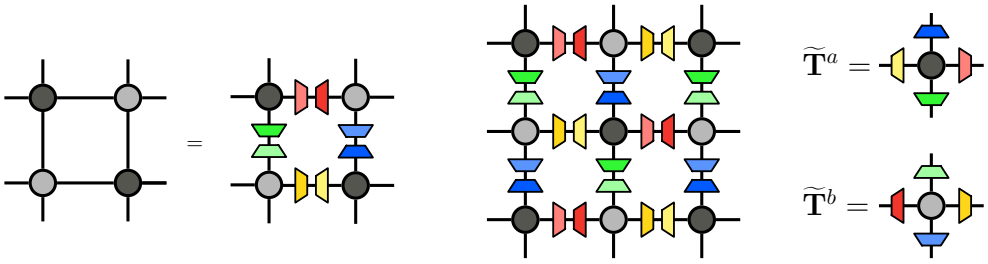

Figure 2.1: Entanglement filtering. (a) Find four pairs of projectors to canonicalize a PBC-MPS. (b) Insert paris of projectors into every link in the tensor network. (c) Define new tensors $\widetilde{\mathbf{T}}^a, \widetilde{\mathbf{T}}^b$ to replace $\mathbf{T}^a, \mathbf{T}^b$.

(Fig. 2.2a), loop-TNR achieves a real-space renormalization group scheme by iterating over four steps:

1. **Entanglement filtering**

   Divide the tensor network into square blocks of four tensors each. Treat each block as an MPS with periodic boundary condition (PBC), and use an iterative algorithm to find four pairs of projectors that act on the internal bonds and can (pseudo-)canonicalize this MPS (Fig. 2.1a). Insert these four pairs of projectors into all bonds in the entire network, according to their respective bond types (Fig. 2.1b). Define $\widetilde{\mathbf{T}}^a$ ($\widetilde{\mathbf{T}}^b$) as $\mathbf{T}^a$ ($\mathbf{T}^b$) contracted with one projector on each leg (Fig. 2.1c), and use $\widetilde{\mathbf{T}}^a$ ($\widetilde{\mathbf{T}}^b$) to replace $\mathbf{T}^a$ ($\mathbf{T}^b$) in the original tensor network. This canonicalization procedure filters out local entanglement in the tensor network, and helps stabilize following computations. This step has a computational cost of $\mathcal{O}(n\chi^5)$, where n is the number of iterations in the MPS canonicalization algorithm, which typically ranges from 5 to 50 in practice.

2. **Truncation and loop optimization**

   Similar to the original TRG algorithm, we decompose each (rank-4) tensor in the network into two rank-3 tensors, so the network becomes a square-octagon lattice (Fig. 2.2b), and attempt to reduce the dimensions of these newly formed bonds. Unlike TRG, which minimizes the local error in each tensor by using truncated SVD, loop-TNR minimizes the error of the eight-legged loop as shown in Fig. 2.2d:

$$E = \left\| \mathbf{T}^a \cdot \mathbf{T}^b \cdot \mathbf{T}^a \cdot \mathbf{T}^b \; - \mathbf{S}^1 \cdot \mathbf{S}^2 \cdot \mathbf{S}^3 \cdot \mathbf{S}^4 \cdot \mathbf{S}^5 \cdot \mathbf{S}^6 \cdot \mathbf{S}^7 \cdot \mathbf{S}^8 \right\|^2 \tag{2.1}$$

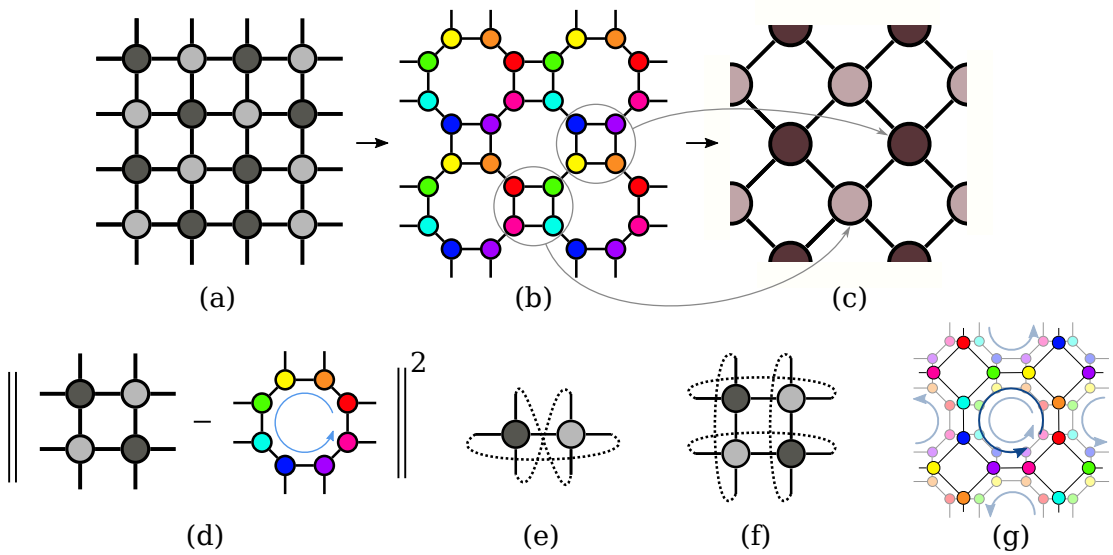

Figure 2.2: (a) A square tensor network composed of two kinds of tensors. (b) A square-octagon tensor network obtained by decomposition. (c) A coarse-grained tensor network. (d) The cost function of loop-TNR. It can be minimized by alternating least square, indicated by the circular arrow. (e) & (f) Gauge independent scalars constructed from local tensors. (g) Two square-octagon tensor networks from two successive loop-TNR iterations stacked together, where each blue circular arrow indicates an optimization loop.

where $\mathbf{S}^i$'s have bond dimensions capped at χ. Optimization can be achieved by the method of alternating least squares, in the same way PBC-MPS's are usually optimized. Initial values of $\mathbf{S}^i$'s can be assigned using TRG's truncated SVD. It also helps to (pseudo-)canonicalize the MPS of $(\mathbf{S}^1 \dots \mathbf{S}^8)$ before and during the optimization for better performance, stability, and entanglement filtering. The computational cost of this step is $\mathcal{O}(n\chi^6)$, where n is the number of iterations in alternating least squares, which typically ranges from 50 to 200 in practice.

3. **Coarse-graining**

   Contract the four $\mathbf{S}^i$ tensors around each square into a new rank-4 tensor, defined as the new $\mathbf{T}^a$ or $\mathbf{T}^b$ (Fig. 2.2c). The network becomes a square lattice with two types of tensors again, but rotated 45 degrees. The computational cost of this step is $\mathcal{O}(\chi^6)$.

4. **Normalization**

We can normalize the new tensors by basically any gauge independent norms of local tensors. The most computationally efficient choice would be the tensor trace $\left|\mathrm{tTr}(\mathbf{T}^a \cdot \mathbf{T}^b)\right|$ as shown in Fig. 2.2e, with a cost of $\mathcal{O}(\chi^3)$. Another frequent choice is $\left|\mathrm{tTr}(\mathbf{T}^a \cdot \mathbf{T}^b \cdot \mathbf{T}^a \cdot \mathbf{T}^b)\right|$ as shown in Fig. 2.2f, which although has a higher cost of $\mathcal{O}(\chi^6)$, is more physically relevant as it relates to the partition function or the norm of a wave function.

The network goes back to its original shape after every two iterations, but with each new local tensor being a coarse-grained approximation of four previous ones. High quality long wavelength physics can often be captured from local tensors after just 10 iterations (i.e. 2^{10} original tensors) with moderate bond dimensions (e.g. $\chi \approx 32$).

We note that there are inequivalent ways to divide the square network in Fig. 2.2a into blocks of four tensors or to decompose it into a square-octagon network. It is important to choose the division and decomposition geometry such that every octagon optimization loop in the current iteration is concentric with an optimization loop in the previous iteration (Fig. 2.2g). Such decomposition geometry consistently produces more accurate results than alternatives.

Out of the four steps outlined above, only the first step "entanglement filtering" relies on the assumption that the tensor network has only two types of tensors on two sub-lattices as in Fig. 2.2a. However, though usually beneficial, this step is not strictly necessary. We can safely skip it if the initial tensor network has a different form. Entanglement filtering can be done via canonicalization during loop optimization, and still achieves proper RG flow. In practice, for most typical square networks, the network will turn into the form in Fig. 2.2a after only one or two iterations. More generally, loop-TNR can even be used to efficiently coarse-grain non-square (e.g. hexagon) tensor networks with minor modifications.

A review of MPS canonicalization and approximation algorithms used in loop-TNR is included in Appendix A.

2.2 Discretizing Euclidean time path integral

To use loop-TNR on the the Euclidean time path integral/evolution operator of a 1+1D quantum system, we need to turn the latter into a suitable tensor network. Consider a 1D quantum lattice system with a d-dimensional local Hilbert space at each site and a dimensionless Hamiltonian of the form $H = \sum_n H_n$, where each H_n is a local two-body interaction term that acts on site $n, n+1$. Because $[H_n, H_m] = 0$ whenever $|m-n| \geq 2$, the

Euclidean time evolution operator can be approximated using Suzuki-Trotter expansion[69]

$$S(\beta) \equiv e^{-\beta H} \approx \left[e^{-\epsilon H_{\mathrm{e}}} e^{-\epsilon H_{\mathrm{o}}}\right]^{M}, \quad \epsilon = \beta/M \ll 1 \tag{2.2}$$

where

$$H_{\mathrm{e}} = \sum_{n \text{ even}} H_n, \qquad H_{\mathrm{o}} = \sum_{n \text{ odd}} H_n. \tag{2.3}$$

Each local term in the evolution operator can be represented by a rank-4 tensor with dimensions (d, d, d, d)

$$A_{(l'_n l'_{n+1}),(l_n l_{n+1})} = \langle l'_n l'_{n+1} | e^{-\epsilon H_n} | l_n l_{n+1} \rangle. \tag{2.4}$$

Matrix elements of the evolution operator reads

$$\langle \{l'_n\} | S(\beta) | \{l_n\} \rangle \approx \sum_{\{l_n^{2M-1}\}} \cdots \sum_{\{l_n^1\}} \prod_{i=0}^{M-1} S^e_{\{l_n^{2i+2}\}\{l_n^{2i+1}\}} S^o_{\{l_n^{2i+1}\}\{l_n^{2i}\}} \tag{2.5}$$

where $l_n^0 \equiv l_n, l_n^{2M} \equiv l'_n$ and

$$\begin{aligned} S^e_{\{l'_n\}\{l_n\}} &\equiv \langle \{l'_n\} | e^{-\epsilon H_{\mathrm{e}}} | \{l_n\} \rangle = \prod_n A_{(l'_{2n} l'_{2n+1}),(l_{2n} l_{2n+1})}, \\ S^o_{\{l'_n\}\{l_n\}} &\equiv \langle \{l'_n\} | e^{-\epsilon H_{\mathrm{o}}} | \{l_n\} \rangle = \prod_n A_{(l'_{2n-1} l'_{2n}),(l_{2n-1} l_{2n})}. \end{aligned} \tag{2.6}$$

Now we have a 2D square tensor network (Fig. 2.3a) that is highly anisotropic due to the smallness of ϵ. This makes any local square blocks of tensors very close to an identity operator, which is difficult to approximate with a lower rank matrix. To make the network more isotropic, and the operator it represents further away from the identity, we proceed to compress multiple horizontal layers of tensors into one layer, increasing the effective time step for each layer to a larger value of β'. First, use SVD to decompose each tensor $\mathbf{A}$ into two rank-3 tensors (Fig. 2.3a-b)

$$A_{(ij),(kl)} \equiv A'_{(ik),(jl)} \overset{\text{SVD}}{=\!=} \sum_p U_{ik,p} \Lambda_p V^*_{jl,p} = \sum_p S^a_{ikp} S^b_{jlp}, \tag{2.7a}$$

$$S^a_{ikp} \equiv \sum_p U_{ik,p} \sqrt{\Lambda_p}\,, \quad S^b_{jlp} \equiv \sum_p \sqrt{\Lambda_p} V^*_{jl,p}. \tag{2.7b}$$

Next, contract alternating $\mathbf{S}^a$ and $\mathbf{S}^b$ tensors in neighbouring layers (Fig. 2.3b-c)

$$T^a_{ruld} = \sum_p S^a_{dpr} S^b_{pul}, \quad T^b_{ruld} = \sum_p S^b_{dpl} S^a_{pur} \tag{2.8}$$

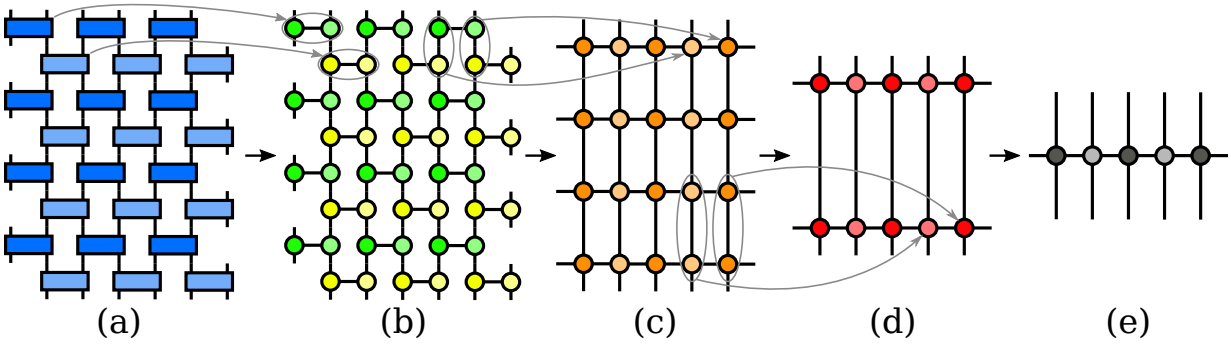

Figure 2.3: (a) A tensor network for the Trotter-approximated Euclidean time evolution operator. (b) A decomposed tensor network of $\mathbf{S}^a$ and $\mathbf{S}^b$. (c) A reorganized square network of $\mathbf{T}^{a,0}$ and $\mathbf{T}^{b,0}$. (c-e) Iteratively combining horizontal layers of tensors using iMPS algorithms.

The network now becomes multiple layers of matrix product operators (MPO) (Fig. 2.3c), which can also be viewed as MPS's by folding their upper and lower physical legs into one side. We then iteratively compress every two adjacent layers into one (Fig. 2.3c-e)

$$T^{a,i+1}_{ruld} = \sum_p T^{a,i}_{r_1 p l_1 d} T^{a,i}_{r_2 u l_2 p}, \quad T^{b,i+1}_{ruld} = \sum_p T^{b,i}_{r_1 p l_1 d} T^{b,i}_{r_2 u l_2 p}, \tag{2.9}$$

where $r \equiv (r_1, r_2)$, $l \equiv (l_1, l_2)$, and $T^{a,0}_{ruld} \equiv T^a_{ruld}, T^{b,0}_{ruld} \equiv T^b_{ruld}$ are the original tensors in (2.8). After each step, we treat each layer as an infinite MPS (iMPS), and perform canonicalization and truncation, to keep the bond dimension from becoming too large. After $\log_2(\beta'/\epsilon)$ iterations, the effective time step has reached the desired value. Typically, if the Hamiltonian is reasonably normalized (e.g. $\max\{\text{eigenvalues of } H_n\} \approx 1$), the network should become reasonably isotropic and well-suited for loop-TNR for an β' close to unity.

More precisely, we want the space-time region represented by a local tensor ($\mathbf{T}^a$ or $\mathbf{T}^b$) to have about equivalent lengths in space and in time, or in other words, a speed of light (in the corresponding field theory) close to unity in unit of tensors. We will discuss the calculation of space-time geometry in the next section. In practice, a trial run of loop-TNR (usually with a small χ) is done first with a reasonable guess of ϵ and β' to compute an approximate value of speed of light. We then adjust ϵ and β' accordingly for a second run of loop-TNR (with a larger χ) for higher quality results.

A further complication is that, even with a speed of light close to unity, during the first few iteration of loop-TNR when finite size effects are still strong, local tensors may still be anisotropic enough to have very different truncation errors for decompositions in the two

orthogonal directions (Fig. 2.2a-b). In this case, to achieve the best efficiency and accuracy, it is best to use different and dynamically adjusted bond dimensions for decompositions in each direction, so that errors in the two directions are closer to each other.

2.3 Transfer matrix and conformal data

We can extract long wavelength physics of the system from the renormalized tensors after some iterations of loop-TNR. The most interesting case would be computing the conformal data of a critical system. Using the exponential map and radial quantization, a 2D conformal field theory (CFT) on a plane is mapped to a cylinder [21], where 1D space is along the periodic azimuthal direction and time is along the axial direction (Fig. 2.4a). A transfer matrix $\mathcal{T}$ of the CFT is a translation operator on the cylinder, whose eigenvalues tell us energies and momenta of the theory on the cylinder, or the central charge c, scaling dimensions $\{\Delta_i\}$ and spins $\{s_i\}$ of the CFT on the plane. For a properly normalized transfer matrix that sweeps through a parallelogram region like in Fig. 2.4b, its eigenvalues $\{\lambda_i\}$ take the form of

$$\lambda_i = \exp\left[-2\pi \mathrm{Im}(\tau)(\Delta_i - \frac{c}{12}) + 2\pi i \mathrm{Re}(\tau)\, s_i\right] \tag{2.10}$$

where τ is the modular parameter of the torus formed by identifying opposite sides of the parallelogram, i.e.

$$\tau = \frac{w_x^b + i w_y^b}{w_x^a + i w_y^a}, \tag{2.11}$$

with $\mathbf{w}^a, \mathbf{w}^b$ being vectors describing directions and extent of space and the translation.

2.3.1 Central charge and scaling dimensions

In the simplest case, the transfer matrix is just a time evolution operator. To construct this operator, consider when the tensor network has gone through an even number ($2m$) of loop-TNR iterations, so its horizontal and vertical bonds are parallel to space and imaginary time directions of the original quantum lattice system respectively (Fig. 2.4c). Take a $w \times h$ rectangular block of tensors, and contract their horizontal bonds on the two ends but keep

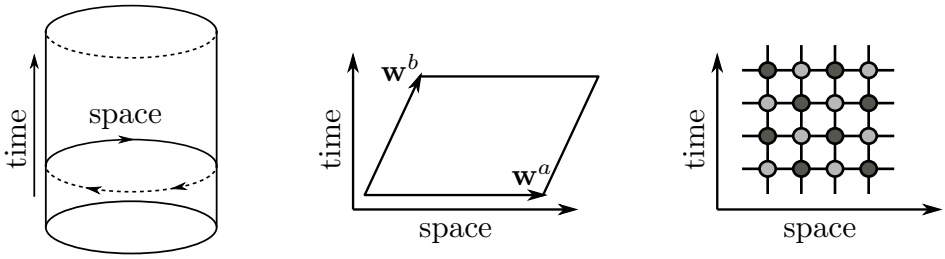

Figure 2.4: (a) The cylindrical spacetime geometry of a radially quantized CFT. (b) A parallelogram shaped spacetime region swept by a general transfer matrix. $\mathbf{w}^a$ represents the periodic space, and $\mathbf{w}^b$ represents the translation. (c) A block of renormalized tensors after $2m$ loop-TNR iterations representing a patch of spacetime region.

the vertical bonds open

$$(\mathcal{T}^{2m}_{w,h})_{(i_1\ldots i_w),(j_1\ldots j_w)} = \quad (2.12)$$

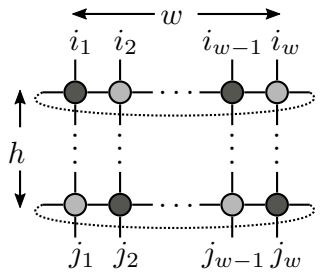

Its eigenvalues take the form of

$$(\lambda^{2m}_{w,h})_i = \exp(-hE_i) = \exp\left[-2\pi v\frac{h}{w}(\Delta_i - \frac{c}{12}) - \varepsilon wh\right] \quad (2.13)$$

where v is the speed of light in unit of tensors, E_i's are scaled energies, and ε is the scaled ground state energy density of the infinite system.

Comparing (2.13) with (2.10), we note that the modular parameter $\tau^{2m}_{w,h} = ivh/w$, and that there is an extra term εwh coming from the normalization of $\mathcal{T}$. To determine this normalization, simply compute two transfer matrices of different width $w = 2, 4$ to solve for ε. We shall assume $\varepsilon = 0$ in all following discussions, as it is a non-universal constant.

To determine $\tau^{2m}_{w,h} = ivh/w$, construct another transfer matrix $\widetilde{\mathcal{T}}^{2m}_{w,h}$ using the same renormalized tensors, but this time with open horizontal bonds and contracted vertical

bonds

$$(\widetilde{\mathcal{T}}^{2m}_{w,h})_{(i_1\ldots i_h),(j_1\ldots j_h)} =$$ 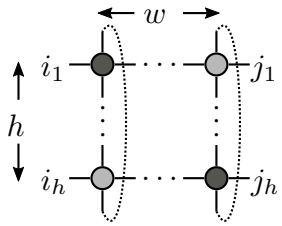

(2.14)

Note that $\widetilde{\tau}^{2m}_{w,h} = -1/\tau^{2m}_{w,h}$, because the two transfer matrices cover the same rectangular region of spacetime except switched roles (and direction) of space and time, hence eigenvalues of $\widetilde{\mathcal{T}}^{2m}_{w,h}$ take the form

$$(\widetilde{\lambda}^{2m}_{w,h})_i = \exp(-w\widetilde{E}_i) = \exp\left[-2\pi\frac{w}{vh}(\Delta_i - \frac{c}{12})\right]. \tag{2.15}$$

Together with the fact that $\Delta_0 = 1$ (corresponding to the identity operator in the CFT), we now have enough equations to solve for all of τ, c and Δ_i's.

2.3.2 Spins

We need a non-zero $\mathrm{Re}(\tau)$ to compute spins of the CFT from a transfer matrix. The most straightforward way to do this is to include a spatial translation directly, such that

$$\mathcal{T} =$$ 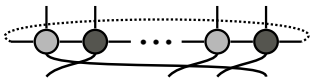 (2.16)

i.e. shifting bonds on one side of the transfer matrix. However, the imaginary exponent has a periodicity of 2π, meaning that spins can only be computed unambiguously up to a maximum absolute value of $|1/2\mathrm{Re}(\tau)|$. A transfer matrices built like (2.16) either has a large $\mathrm{Re}(\tau)$ (e.g. $1/2$), or has a high computational cost due to its large width.

To work around this problem, we consider the tensor network after an odd number $(2m+1)$ of loop-TNR iterations. At this stage, the network not only appears rotated compared to its original shape, but each local tensor also represents a diamond shaped spacetime region rather than a rectangular one (Fig. 2.5). Using the relation between modular parameters

$$\tau^{2m+1}_{w,w} = \frac{\tau^{2m}_{w,w} - 1}{\tau^{2m}_{w,w} + 1}, \tag{2.17}$$

we see that, for example, $\mathrm{Re}(\tau^{2m+1}_{2,2}) \approx -0.105$ for $\tau^{2m}_{2,2} = 0.9i$, which is enough to calculate spins up to an absolute value of 4 and only for a moderate computational cost.

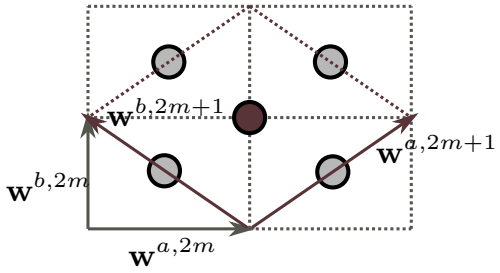

Figure 2.5: Renormalized tensors after $2m$ ($2m$+1) loop-TNR iterations as denoted by grey (dark red) circle(s) and their corresponding spacetime regions indicated by dotted lines. Legs of the tensors are omitted. (2.17) can be derived from the geometric relation between $\mathbf{w}^{a,2m}, \mathbf{w}^{b,2m}$ and $\mathbf{w}^{a,2m+1}, \mathbf{w}^{b,2m+1}$ shown here.

2.3.3 Computational considerations

Physical quantities computed from a tensor network should be independent of the tensor network's gauge freedom. This requirement when applied to eigenvalues of the transfer matrix means that (2.12) must have width and height of even numbers, because the tensor network in a normal loop-TNR implementation has two types of tensors on two sub-lattices. The smallest possible transfer matrix constructed this way is $\mathcal{T}^m_{2,2}$, which can be sparse diagonalized with a computational cost of $\mathcal{O}(n\chi^5)$, where n is the number of iterations in the sparse diagonalization algorithm (e.g. the Arnoldi algorithm).

The largest eigenvalues of the transfer matrix, corresponding to the smallest scaling dimensions and low energy physics of the system, generally have good numerical accuracy. Eigenvalues become less accurate as they become smaller and eventually indistinguishable from random noise at the smallest end, because of truncation errors in the RG process. To improve the accurate range of eigenvalues, it desirable to construct wider transfer matrices with larger dimensions. The second smallest transfer matrix constructed by (2.12) is $\mathcal{T}^m_{4,2}$, but its sparse diagonalization already has a computational cost of $\mathcal{O}(n\chi^8)$, much larger than the rest of the loop-TNR algorithm.

This cost can be reduced by using renormalized tensors $\mathbf{T}^{a,m+1}, \mathbf{T}^{b,m+1}$ from the next loop-TNR iteration (but before they are normalized in step 4 of Sec. 2.1). Specifically,

define

$$\mathcal{A}^m_{(i_1i_2i_3i_4)(j_1j_2j_3j_4)} \equiv$$ 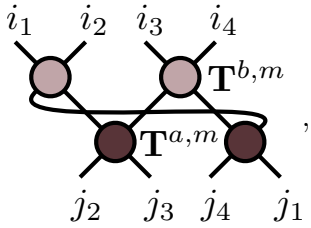

, (2.18)

and we can show that $\mathcal{A}^{m+1}$'s lowest eigenvalues approximate those of $\mathcal{T}^m_{4,2}$'s by decomposing $\mathbf{T}^{a,m}, \mathbf{T}^{b,m}, \mathbf{T}^{a,m+1}$ and $\mathbf{T}^{b,m+1}$ into the rank-3 $\mathbf{S}^i$ tensors and rearranging $\mathbf{S}^i$'s. Sparse diagonalization of $\mathcal{A}$ has a computation cost of only $\mathcal{O}(n\chi^6)$, comparable to the rest of the algorithm. Although this procedure includes more approximations, it still produces significantly increased range of accurate eigenvalues with a small computational overhead in practice.

We further note that the efficient diagonalization of $\mathcal{T}^m_{4,2}$ is what enables us to efficiently determine the proper conformal normalization (i.e. ε) of the transfer matrix in Sec. 2.3.1. Without this optimization, conformal normalization can still be efficiently found using the alternative method of calculating tensor traces, as was done in [29], but the method described in Sec. 2.3.1 gives a more accurate value of the central charge in practice, especially for quantum systems.

Finally, we come back to the comment made in Sec. 2.2 that loop-TNR works best when the spacetime region represented by a local tensor has about equal length in space and in time, or in terms of the modular parameter, $\tau^m_{2,2} \approx i$. After one run of loop-TNR which gives the modular parameter $\tau^{2m}_{2,2} = it$, we can precisely adjust it to i in the next run by dividing the initial time step ϵ in the Suzuki-Trotter expansion by t. If we want to calculate spins, then the target value for $\tau^{2m}_{2,2}$ should be something close to but not equal to i, and adjust ϵ accordingly.

2.4 Benchmark results

Transverse field Ising model

The 1D transverse field Ising model (TFIM) is defined by

$$H = -\sum_n \sigma^x_n \sigma^x_{n+1} - h \sum_n \sigma^z_n. \tag{2.19}$$

Ising CFT	Classical Ising model				TFIM
Exact	TRG [29] $\chi = 120$	TNR [20] $\chi = 24$	Loop-TNR [97] $\chi = 24$	Gilt-TNR [35] $\chi = 120$	Loop-TNR $\chi = 24$
0.125	0.124993	0.1250004	0.12500011	0.12500015	0.125012
1	1.0002	1.00009	1.000006	1.00002	0.999999
1.125	1.1255	1.12492	1.124994	1.12504	1.124957
1.125	1.1255	1.12510	1.125005	1.12506	1.124969
2	2.002	1.9992	1.9997	2.0002	1.999872
2	2.002	1.99986	2.0002	2.0002	1.999957
2	2.003	2.00006	2.0003	2.0003	2.000059
2	2.002	2.0017	2.0013	2.0004	2.000323

Table 2.1: Scaling dimensions computed from the TFIM compared with that from the 2D classical Ising model and the exact Ising CFT values.

It has a critical point at $h = 1$ described by the Ising CFT. We compute the central charge c, scaling dimensions Δ's and spins s's at this critical point using loop-TNR with $\chi = 24$. The lowest scaling dimensions computed from $\mathcal{T}_{2,2}^{14}$ are listed in Table 2.1 and compared with earlier results obtained from the classical Ising model and exact CFT values. Similar accuracy is observed compared with earlier results. More conformal data obtained from $\mathcal{T}_{4,2}^{2m}$ is plotted in Fig. 2.6.

XY model

The spin-1/2 XY model is defined by

$$H = -\sum_n (\sigma_n^x \sigma_{n+1}^x + \sigma_n^y \sigma_{n+1}^y) \tag{2.20}$$

It is described by the massless free fermion CFT, or equivalently, the compactified boson at radius $\rho = \sqrt{2}$[1]. We compute its conformal data with loop-TNR at $\chi = 32$ and 42, and plot the results in Fig. 2.7. Being a non-minimal model with a larger central charge $c = 1$, the XY model is evidently more numerically challenging. We see that the $\chi = 32$ results deteriorate in accuracy as early as the 12th iteration. However, the efficiency of loop-TNR allows us to increase bond dimension to $\chi = 42$ to achieve much better results, and still complete 20 loop-TNR iterations within 12 hours[2].

[1] We choose the normalization such that the self-dual radius is $\rho = 1$ throughout this thesis.

[2] We used a computing node with 24 cores of Intel(R) Xeon(R) 2.40GHz CPU.

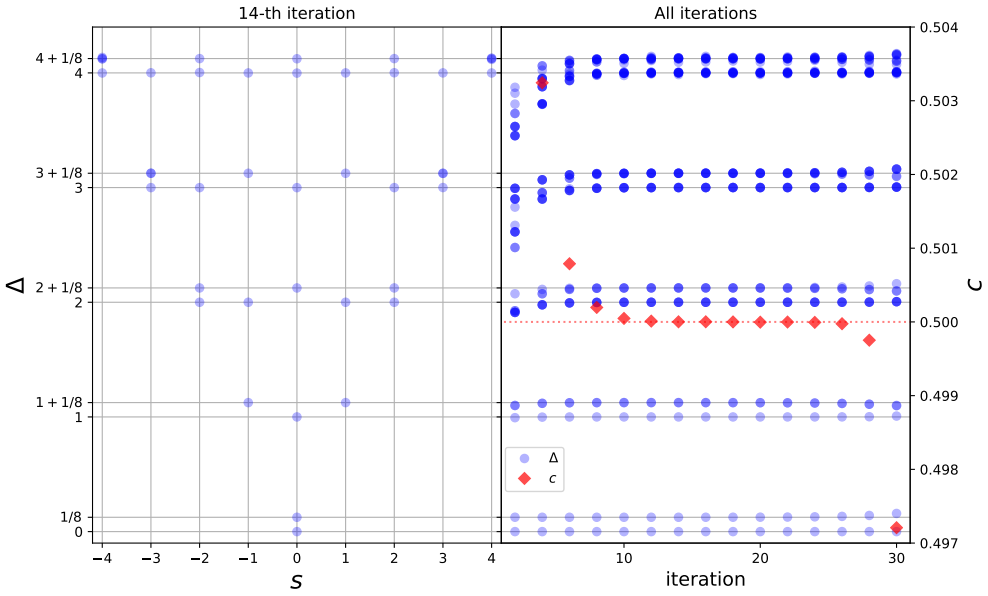

Figure 2.6: Conformal data extracted from the TFIM using loop-TNR at $\chi = 24$ and the transfer matrix $\mathcal{T}_{4,2}^{2m}$, compared with exact values as marked by horizontal lines.

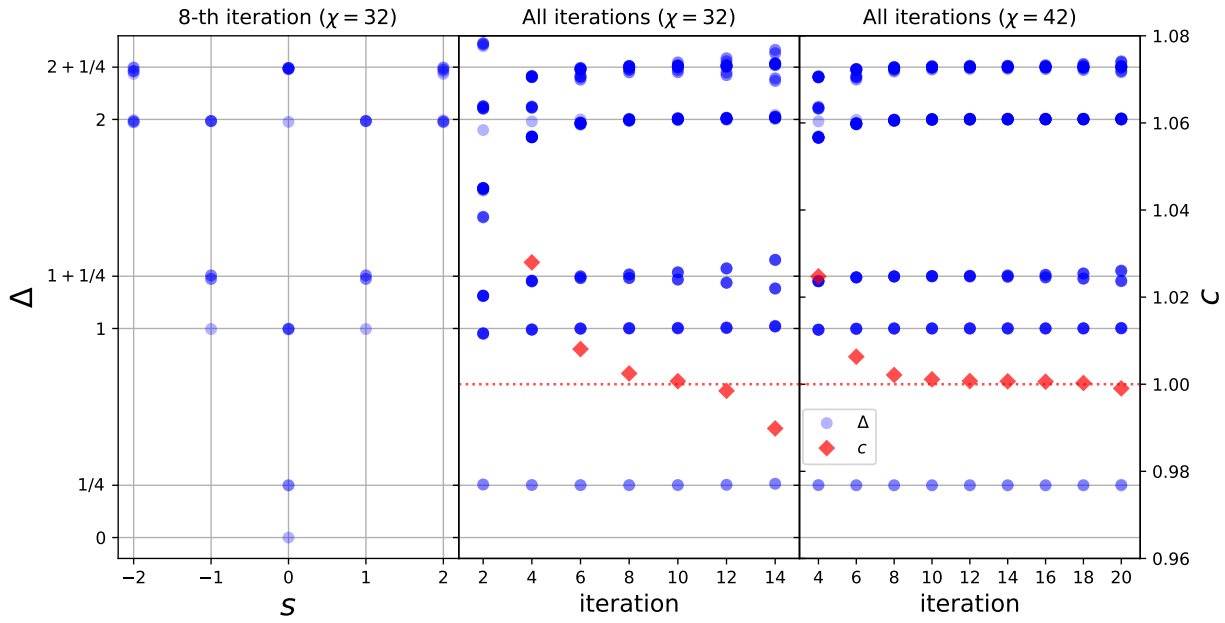

Figure 2.7: Conformal data extracted from the XY model using loop-TNR at $\chi = 32$ and 42 and the transfer matrix $\mathcal{T}_{4,2}^{2m}$, compared with exact values as marked by horizontal lines.

XXZ model

The spin-1/2 XXZ model

$$H = \sum_n [\sigma_n^x \sigma_{n+1}^x + \sigma_n^y \sigma_{n+1}^y - \cos(g\pi)\sigma_n^z \sigma_{n+1}^z] \tag{2.21}$$

is known to be described by the compactified boson CFT at radius $\rho = g$ for $0 < g \leq 1$. We compute their scaling dimensions using loop-TNR at $\chi = 42$ and transfer matrix $\mathcal{T}_{4,2}^{18}$. Results are plotted in Fig. 2.8a and compared with exact values predicted by CFT. We observed excellent agreement for $0.1 < g < 0.8$. When $g < 0.1$, the system gets close to the ferromagnetic phase, which has quadratic rather than linear dispersion and is infinitely degenerate. The high density of low energy states overwhelms the limited size of renormalized tensors, therefore accuracy suffers. When $g > 0.8$, numerical accuracy is still good per se, but the isotropic XXX model contains marginally irrelevant operators whose effects decay only logarithmically in system size. After 18 loop-TNR iterations, we are still seeing significant finite size effects. We show the computed scaling dimensions at all iterations in Fig. 2.8b, where we can see the values slowly converging. However, after about 20 iterations, truncation errors accumulated from all iterations start to drive the system away from the critical point, hence full convergence cannot be obtained.

The marginal operator in the XXX model can be tuned by adding a next-nearest neighbour interaction term [39]

$$H = \sum_n [\sigma_n^x \sigma_{n+1}^x + \sigma_n^y \sigma_{n+1}^y + \sigma_n^z \sigma_{n+1}^z] + J_2 \sum_n [\sigma_n^x \sigma_{n+2}^x + \sigma_n^y \sigma_{n+2}^y + \sigma_n^z \sigma_{n+2}^z]. \tag{2.22}$$

At $J_2 \approx 0.2422$, the marginal operator vanishes, and we can easily obtain accurate scaling dimensions. We plot the loop-TNR results for this Hamiltonian in Fig. 2.8c, and find excellent agreement with CFT predictions.

The Haldane chain

The Haldane chain is a spin-1 system defined as

$$H = \sum_n \left[\mathbf{S}_n \cdot \mathbf{S}_{n+1} + U(S_n^z)^2 + B S_n^x \right]. \tag{2.23}$$

It has an SPT phase near $(U, B) = (0, 0)$ and a trivial spin polarized phase when $U \gg 1$. The transition between these two phases is second order at $U \approx 1, B = 0$. Using loop-TNR, we locate this critical point more precisely at $U \approx 0.967(2)$, and compute its scaling dimensions, plotted in Fig. 2.9. The numerical results are well matched by the compactified boson CFT at radius $\rho = 0.6153(3)$.

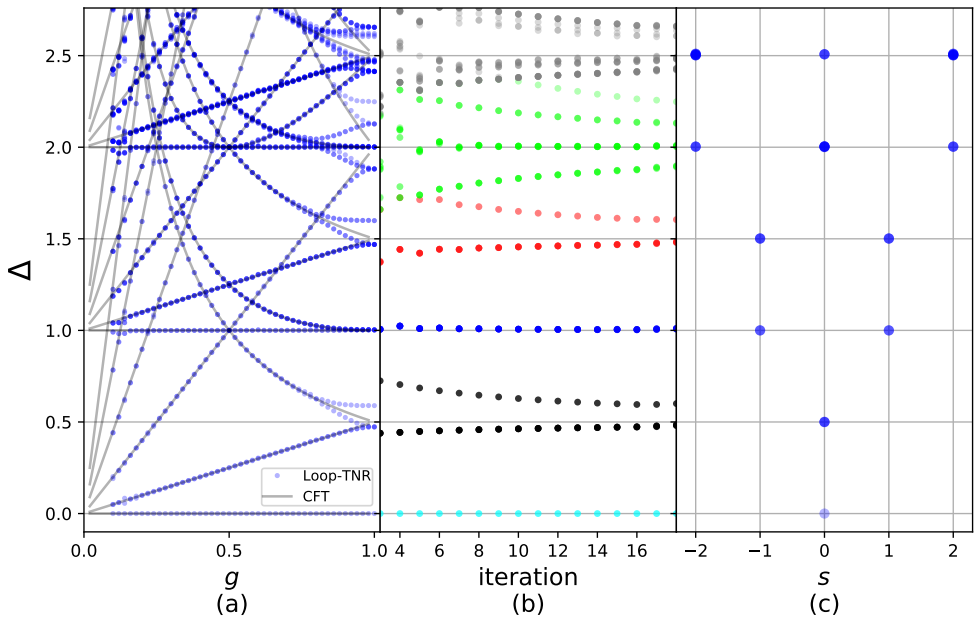

Figure 2.8: (a) Scaling dimensions of the XXZ model computed from $\mathcal{T}^{18}_{4,2}$ compared with CFT exact values. (b) Scaling dimensions of the XXX model plotted against loop-TNR iteration. Data points are coloured based on their expected convergent values, which are marked by horizontal lines. (c) Scaling dimensions of the XXX model with next-nearest-neighbour interaction that cancels marginal operators, plotted against conformal spin, with CFT values marked by horizontal lines.

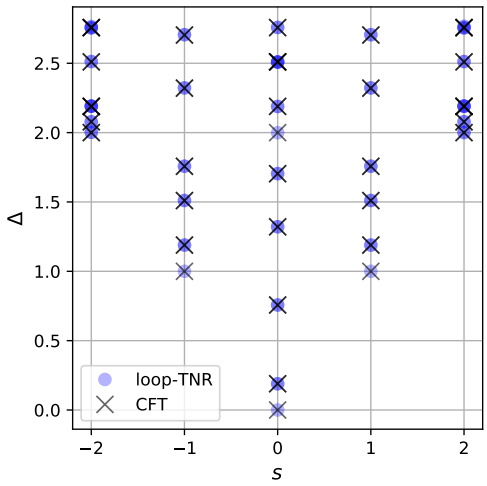

Figure 2.9: Scaling dimensions and spins of the Haldane chain at $(U, B) = (0.967, 0)$ computed using loop-TNR with $\chi = 42$, compared with best-fit CFT values.

Yang-Lee edge singularity

The Yang-Lee edge singularity may be described as a line of critical points of the Ising model under an imaginary magnetic field

$$H = -\sum_n \left[\sigma_n^z + \lambda \sigma_n^x \sigma_{n+1}^x + ih\sigma_n^x\right]. \tag{2.24}$$

Its locations are plotted in Fig. 2.10a [81]. Being a non-unitary minimal model, it has negative central charge and scaling dimensions (of primary fields)

$$c = -\frac{22}{5}, \quad \Delta = 0, -\frac{2}{5}. \tag{2.25}$$

This invalidates our usual assumption that the lowest energy state corresponds to the identity operator. We define the effective central charge c_{eff} and effective scaling dimension Δ_{eff} to be values of the central charge and scaling dimensions as computed following the normal unitarity assumption. Then

$$-\frac{c_{\text{eff}}}{12} = -\frac{c}{12} + \Delta_{\text{min}}, \quad \Delta_{\text{eff}} = \Delta - \Delta_{\text{min}}, \tag{2.26}$$

where Δ_{min} is the smallest scaling dimension in the theory. For Yang-Lee singularity, $\Delta_{\text{min}} = -2/5$, and we find

$$c_{\text{eff}} = \frac{2}{5}, \quad \Delta_{\text{eff}} = 0, \frac{2}{5}, \ldots \tag{2.27}$$

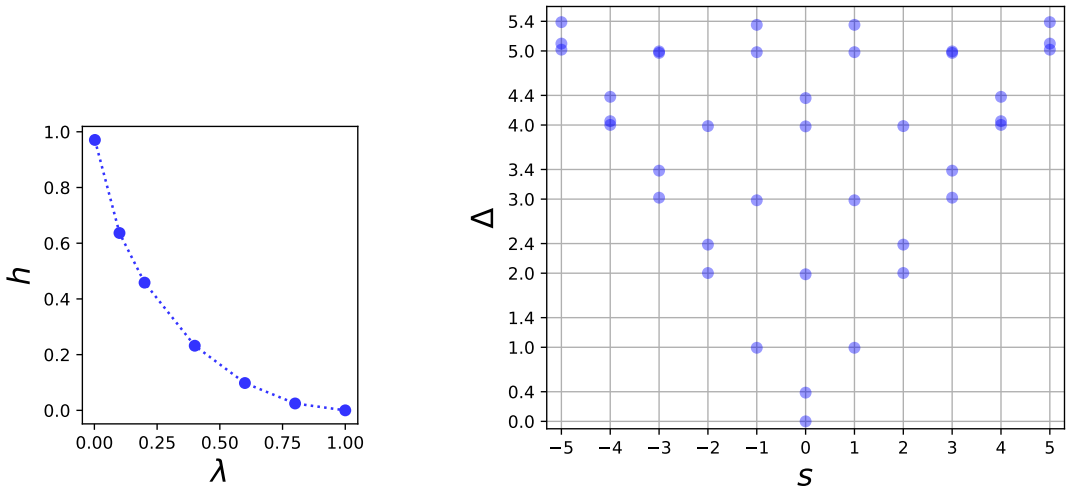

(a) (b)

Figure 2.10: (a) Location of Yang-Lee singularity [81]. (b) Effective scaling dimensions and spins of the Yang-Lee singularity computed using loop-TNR with $\chi = 48$, compared with exact values marked by horizontal lines.

We compute conformal data of the model at $(\lambda, h) = (0.4, 0.23202)$ using loop-TNR at $\chi = 48$. We obtained effective central charge $c_{\text{eff}} = 0.399528$, and spins and effective scaling dimensions plotted in Fig. 2.10b.

2.5 Non-analytic finite size effects and virtual-space transfer matrix

In the Sec. 2.3, we implicitly assumed that any finite patch of our renormalized tensor network is a proper discretized representation of the field theory path integral. It is under this assumption that we can establish the correspondence between conformal data and eigenvalues of transfer matrices constructed from renormalized tensors in any orientation. This assumption also underlies the common expectation that finite size effects of a lattice system should diminish as system size or real-space RG iteration increases. Unfortunately, this assumption is not always valid. As first studied in [94] in details, the discreteness of the lattice may introduce so-called non-analytic finite size effects to the model, resulting in oscillatory and incommensurate structures. They limit the direct correspondence between

the lattice model and its field theory to only a subset of system sizes. For all other system sizes, non-analytic finite size effects do not diminish as the system becomes larger, and become hindrance to numerical calculation of field theory properties.

As a simple example, we consider the XY model with periodic boundary condition defined by

$$H = -\frac{1}{2}\sum_n (\sigma_n^x \sigma_{n+1}^x + \sigma_n^y \sigma_{n+1}^y) + h\sum_n \sigma_n^z. \tag{2.28}$$

This model can be solved exactly using the Jordan-Wigner transformation, and known to be described by the massless free fermion CFT for all $h \in (-1, 1)$. In Fig. 2.11, we plot its low energy states against lattice momentum for a system of 600 sites at $h = 0, \cos(\pi/4)$ and $\cos(\pi/6)$. It is evident from the plot that some folding (i.e. defining lattice momentum using a coarser n-site ($n > 1$) translation operator) is necessary to combine the several "towers" of states into a single tower to make the correspondence with the CFT, and the lattice size need to be compatible with the folding. More precisely, for $h = \cos(p/q)$ where p, q are coprime integers, the system size must be an integral multiple of q for the low energy states to be compatible with the CFT description. In Fig. 2.12a, we plot scaled energies against system sizes N for $h = \cos(\pi/30)$, and observe that energies oscillate steadily with a period of $q = 30$, and indeed only coincide with CFT predictions when $N \bmod q = 0$. Underlying this phenomenon is the fact that a smooth field operator is only obtained after averaging over q sites for the XY model. When $N \bmod q \neq 0$, extra sites act like a defect operator, shifting energies of the system. We refer to [94] for more details.

In the context of loop-TNR of quantum lattice systems, this requirement on system size means that for a transfer matrix to produce results in direct correspondence with CFT predictions, it must be constructed from a block of tensors whose width is an integral multiple of q in terms of the initial local tensors $\mathbf{T}^{a,0}, \mathbf{T}^{b,0}$. This condition is automatically satisfied in loop-TNR if q is a power of 2, and still easy to satisfy if q only contains a few other small factors such as 3. If q contains some more large factors or is simply unknown, then it is impractical to satisfy this condition in general. However, we note that $\widetilde{\mathcal{T}}^{2m}_{w,h}$ in (2.14) is special among all the transfer matrices we constructed in Sec. 2.3, in that its width can be extended "free of cost" because of its open horizontal bonds. Specifically,

$$\widetilde{\mathcal{T}}^{2m}_{qw,h} = (\widetilde{\mathcal{T}}^{2m}_{w,h})^q, \quad (\widetilde{\lambda}^{2m}_{qw,h})_i = [(\widetilde{\lambda}^{2m}_{w,h})_i]^q. \tag{2.29}$$

In practice, this means that we can treat any $\widetilde{\mathcal{T}}^{2m}_{w,h}$ as a proper transfer matrix of the CFT as long as we ignore its superfluous imaginary exponent, whatever its width is.

We call $\widetilde{\mathcal{T}}^{2m}_{w,h}$ the *virtual space transfer matrix* of the original 1D quantum lattice system, denoted simply by $\widetilde{\mathcal{T}}$, and $\mathcal{T}^{2m}_{w,h}$ the *real space transfer matrix*, denoted by $\mathcal{T}$. $\widetilde{\mathcal{T}}$ effectively

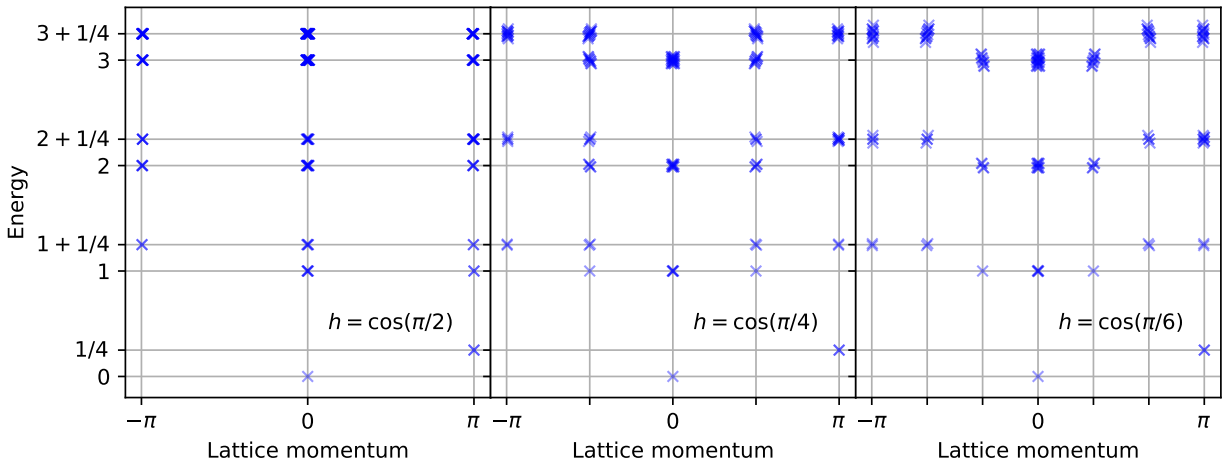

Figure 2.11: Spectrum of the XY model at system size $N = 600$ under transverse field of strength $h = \cos(\pi/q)$ with $q = 2, 4, 6$. We see states scattered along different values of lattice momentum. Folding is required to map them to the CFT tower of states around $s = 0$.

defines another related quantum system in a virtual space (aka Trotter space or quantum space), with $\widetilde{E}_i = -\mathrm{Re}(\ln \widetilde{\lambda}_i)$ as its (scaled) energies, which we will call *virtual energies* of the original system. Because the virtual space extends along the direction of the Euclidean time of the original lattice model, which is inherently continuous, we do not expect similar non-analytic finite size effects that are results of the discreteness of the lattice. We plot the real and virtual energies of the XY model in Fig. 2.12b-c to illustrate the latter's effectiveness at capturing the underlying CFT.

To better understand the difference between virtual space and real space transfer matrices, notice that given a finite block of the tensor network representing the path integral of a quantum lattice system, the resulting $\mathcal{T}$ is the transfer matrix of a finite size system with potentially zero temperature, whereas $\widetilde{\mathcal{T}}$ is the transfer matrix of a finite temperature system potentially in the thermodynamic limit, i.e.

$$\lim_{n\to\infty} \mathrm{Tr}(\mathcal{T}^n) = Z(N < \infty, T = 0), \quad \lim_{n\to\infty} \mathrm{Tr}(\widetilde{\mathcal{T}}^n) = Z(N \to \infty, T > 0). \tag{2.30}$$

It is then natural that $\widehat{\mathcal{T}}$ can capture thermodynamic properties of the system better than $\mathcal{T}$, without UV details from the lattice. We note that this property of the virtual space transfer matrix has been exploited before in transfer matrix DMRG [7, 84] to compute finite temperature properties of quantum systems in the thermodynamic limit.

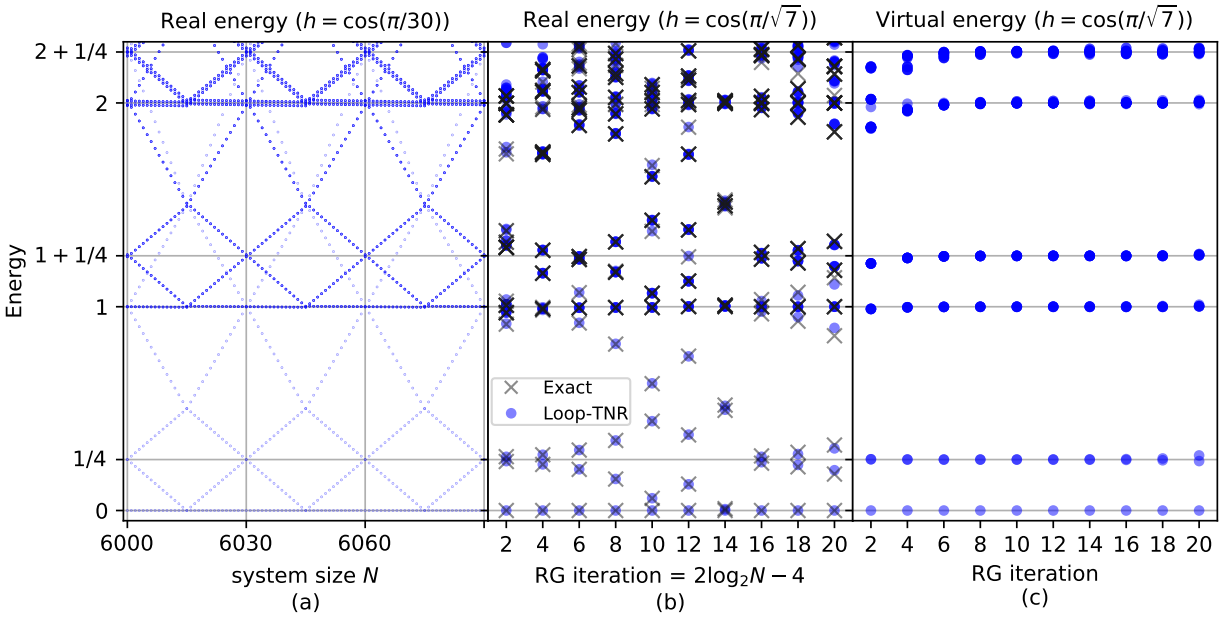

Figure 2.12: (a) Scaled energies NE of the XY model under transverse field $h = \cos(\pi/30)$, oscillating around exact CFT values marked by horizontal lines. (b) Scaled energies of the XY model at $h = \cos(\pi/\sqrt{7})$ plotted against loop-TNR iteration number (log scale in system size), jumping around exact CFT values marked by horizontal lines. (c) Scaled virtual energies of the XY model at $h = \cos(\pi/\sqrt{7})$, matching exact CFT values almost perfectly.

Using only virtual space transfer matrices to compute conformal data of a system with non-analytic finite size effects poses some limitations. First of all, the modular parameter $\widetilde{\tau}$ can no longer be computed straightforwardly, and central charge c and scaling dimensions Δ_i computed from a virtual space transfer matrix are all only determined up to a constant scaling factor $\mathrm{Im}(\widetilde{\tau})$. To workaround this problem, we must know c or at least one of non-zero Δ_i's a priori to set the correct scale. In principle, it is possible to extract central charge from renormalized entanglement entropy computed from real space transfer matrix $\mathcal{T}_{w,h}^{2m}$ at different widths, but we find it more efficient and accurate to use DMRG instead. Secondly, we can no longer compute conformal spins from an "oblique" transfer matrix $\mathcal{T}_{w,h}^{2m+1}$ in the way explained in Sec 2.3.2, because its length in the periodic direction does not satisfy the proper condition in general. Limited conformal spins may still be computed from a virtual-space transfer matrix with translation (like (2.16) but for $\widetilde{\mathcal{T}}$), but it comes with a much higher computational cost of at least $\mathcal{O}(n\chi^8)$, and is dependent on our knowledge of q, which can be hard to come by.

On the upside, using the virtual-space transfer matrix in loop-TNR together with DMRG, we can extract all the low lying scaling dimensions from a lattice model with non-analytic finite size effects. Going into the continuous virtual space circumvents the size constraint posed on the real-space lattice, avoiding computationally expensive operations that would be otherwise needed to accommodate such constraints. The computational cost of DMRG needed to extract an accurate central charge is no greater than a typical run of loop-TNR in practice.

2.6 Extension to fermionic systems

The loop-TNR algorithm, as first introduced in [97] and as discussed in this thesis so far, only applies to bosonic/spin systems. In this section, we discuss how it can be extended to fermionic systems by introducing Grassmann tensor networks. Grassmann tensor networks are originally introduced in [25, 27] as variational ansatz of 2D fermion wave functions. In this section, we will instead motivate Grassmann tensor networks from fermion coherent state path integral of 1+1D systems, and use slightly different formulation and conventions that are easier to understand and use in the current context.

2.6.1 Fermion coherent state path integral

Representing a fermionic system numerically in the Fock space has the problem of having the global dependency on the order of particles. Fermion coherent states can solve this

problem by using Grassmann numbers that handle sign changes locally.

An N-particle fermion coherent state $|\boldsymbol{\eta}\rangle \equiv |\eta_1, \ldots, \eta_N\rangle$ is defined as the eigenstate of fermionic annihilation operators $c_1, \ldots, c_N$, i.e.

$$c_n|\boldsymbol{\eta}\rangle = \eta_n|\boldsymbol{\eta}\rangle, \quad \langle\boldsymbol{\eta}|c_n^\dagger = \langle\boldsymbol{\eta}|\bar{\eta}_n \tag{2.31}$$

where $\bar{\eta}_n$ is the conjugate of η_n. It is constructed as

$$|\boldsymbol{\eta}\rangle = e^{-\sum_n \eta_n c_n^\dagger}|0\rangle = \prod_n (1 - \eta_n c_n^\dagger)|0\rangle, \tag{2.32}$$

where η_n's (and $\bar{\eta}_n$'s) are anti-commuting Grassmann numbers and $|0\rangle$ is the vacuum state.

By taking inner products, the coherent state acts as a map that maps all states in (and operators on) the Hilbert space into Grassmann numbers, which form a complex vector space themselves, with $\{\eta_n\}$ (and $\{\bar{\eta}_n\}$) as the basis. One can also show the resolution of the identity in fermion coherent states is

$$\mathbb{1} = \int \prod_n \left(\mathrm{d}\bar{\eta}_n \mathrm{d}\eta_n \, e^{-\bar{\eta}_n \eta_n}\right) |\boldsymbol{\eta}\rangle\langle\boldsymbol{\eta}| \equiv \int \mathrm{d}\bar{\boldsymbol{\eta}}\mathrm{d}\boldsymbol{\eta} \, e^{-\bar{\boldsymbol{\eta}}\cdot\boldsymbol{\eta}}|\boldsymbol{\eta}\rangle\langle\boldsymbol{\eta}|. \tag{2.33}$$

The fermion coherent state path integral is built by inserting the resolution of the identity into time slices of the Euclidean time evolution operator

$$\langle\boldsymbol{\eta}'|e^{-\beta H}|\boldsymbol{\eta}\rangle = \int \prod_{k=1}^{M} \mathrm{d}\bar{\boldsymbol{\eta}}^k \mathrm{d}\boldsymbol{\eta}^k e^{-\bar{\boldsymbol{\eta}}^k\cdot\boldsymbol{\eta}^k} \langle\boldsymbol{\eta}^k|e^{-\epsilon H}|\boldsymbol{\eta}^{k-1}\rangle, \tag{2.34}$$

where $\boldsymbol{\eta}_0 \equiv \boldsymbol{\eta}, \boldsymbol{\eta}_M \equiv \boldsymbol{\eta}'$ and $\epsilon \equiv \beta/M$. More details on Grassmann numbers and fermion coherent state path integral can be found in standard reference text, e.g. [2].

Assuming the system is 1+1D with only nearest-neighbour interactions $H = \sum_n H_{n,n+1}$, and using Suzuki-Trotter expansion just like in Sec. 2.2, we can rewrite the path integral as

$$\begin{aligned}\langle\boldsymbol{\eta}'|e^{-\beta H}|\boldsymbol{\eta}\rangle = \int \prod_{k=1}^{M} \Big(\prod_{n \text{ even}} & g_{\bar{\eta}_n^{2k}\eta_n^{2k}} \, g_{\bar{\eta}_{n+1}^{2k}\eta_{n+1}^{2k}} A_{(\eta_n^{2k}\eta_{n+1}^{2k}),(\eta_n^{2k-1}\eta_{n+1}^{2k-1})} \Big) \\ & \cdot \Big(\prod_{n \text{ odd}} g_{\bar{\eta}_n^{2k-1}\eta_n^{2k-1}} g_{\bar{\eta}_{n+1}^{2k-1}\eta_{n+1}^{2k-1}} A_{(\eta_n^{2k-1}\eta_{n+1}^{2k-1}),(\eta_n^{2k-2}\eta_{n+1}^{2k-2})} \Big)\end{aligned} \tag{2.35}$$

where $\boldsymbol{\eta}' \equiv \boldsymbol{\eta}_{2M}$, $g_{\bar{\eta}\eta} \equiv \mathrm{d}\bar{\eta}\mathrm{d}\eta \, e^{-\bar{\eta}\eta}$ and

$$A_{(\eta_n'\eta_{n+1}'),(\eta_n\eta_{n+1})} \equiv \langle\eta_n'\eta_{n+1}'|e^{-\epsilon H_{n,n+1}}|\eta_n\eta_{n+1}\rangle. \tag{2.36}$$

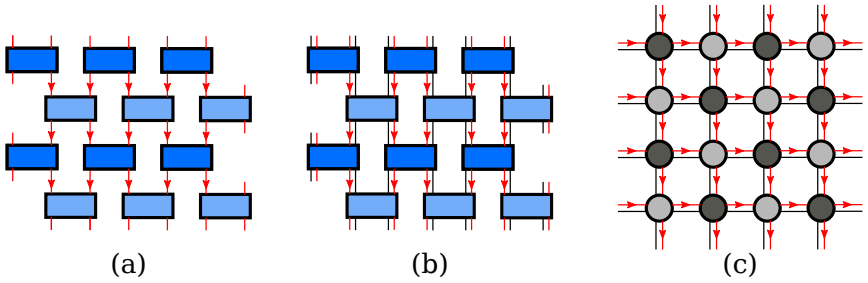

Figure 2.13: (a) The Grassmann tensor network representation of the path integral of a system with only fermionic degrees of freedom. (b) The Grassmann tensor network representation of the path integral of a system with both fermionic and spin/bosonic degrees of freedom. (c) An isotropic Grassmann tensor network representing the path integral of a general 1+1D quantum system.

This expression formally looks very similar to (2.5) and (2.6) in Sec. 2.2, where each $A_{(\eta'_n\eta'_{n+1}),(\eta_n\eta_{n+1})}$ is like a rank-4 local tensor, and $g_{\bar{\eta}\eta}$'s can serve as the metric of the tensor network living on the edges/links. We represent the coherent state path integral as a diagram in Fig. 2.13a just like a tensor network, where $g_{\bar{\eta}\eta}$'s are drawn as an arrow in the diagram to indicate the order of its two Grassmann numbers (because it only has this one binary degree of freedom). Note that each $A_{(\eta'_n\eta'_{n+1}),(\eta_n\eta_{n+1})}$ or $g_{\bar{\eta}\eta}$ always contains an even number of Grassmann numbers, hence there is no global dependency in their order.

2.6.2 Grassmann tensor network renormalization

To formalize the notion of a Grassmann tensor network representation, we write for every two-body fermionic operator O

$$\langle\eta_1\eta_2|O|\eta_3\eta_4\rangle = \sum_{\{n_a=0,1\}} O^{n_1n_2n_3n_4}(\eta_1)^{n_1}(\eta_2)^{n_2}(\eta_3)^{n_3}(\eta_4)^{n_4} \equiv \sum_{\{n_a=0,1\}} [\mathbf{O}(\boldsymbol{\eta})]^{n_1n_2n_3n_4}. \quad (2.37)$$

$\mathbf{O}$ is a Grassmann tensor with 16 sectors (8 of which are zero) labelled by Grassmann indices $(n_1n_2n_3n_4)$, with each sector being a unique combination of Grassmann numbers multiplied by a complex number $O^{n_1n_2n_3n_4}$. (2.35) is then a Grassmann tensor network of $\mathbf{O}$'s. More generally, the operator may have both fermionic and bosonic/spin degrees of freedom, so $\mathbf{O}$ may have sectors with non-trivial bond dimensions and spin indices $(i_1i_2i_3i_4)$, i.e.

$$[\mathbf{O}(\boldsymbol{\eta})]^{n_1n_2n_3n_4}_{i_1i_2i_3i_4} = O^{n_1n_2n_3n_4}_{i_1i_2i_3i_4}(\eta_1)^{n_1}(\eta_2)^{n_2}(\eta_3)^{n_3}(\eta_4)^{n_4}. \quad (2.38)$$

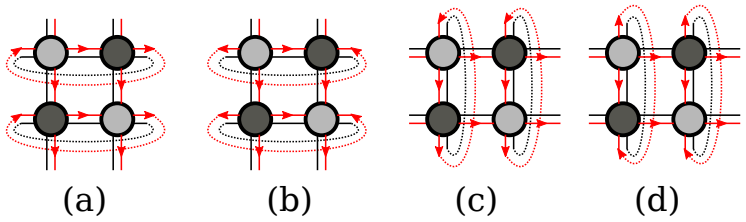

Figure 2.14: (a)(c) Real space and virtual space transfer matrix with periodic boundary condition. (b)(d) Real space and virtual space transfer matrix with anti-periodic boundary condition. Arrows on free legs indicate how they should be contracted with vectors they act on.

Such a Grassmann tensor has two indices on every leg, denoted by double lines in the corresponding diagram, and the network looks like Fig. 2.13b. We define Grassmann tensors and discuss its calculus more rigorously in Appendix B.

With the path integral of a fermionic system expressed as a proper Grassmann tensor network, and the calculus of Grassmann tensors properly defined, it is then straightforward to extend loop-TNR to fermionic systems, leading to what we call loop-GTNR. We transform the anisotropic Grassmann tensor network (2.35) into a more isotropic one (Fig. 2.13c) following the same steps in Sec. 2.2, and use loop optimization to coarse-grain this network just as described in Sec. 2.1 and Appendix A, with the only difference being replacing every contraction, SVD, QR decomposition and conjugation with the corresponding Grassmann tensor operation defined in Appendix B.

When constructing the transfer matrix from a Grassmann tensor network, extra care is needed in choosing the spin structure. Namely, when contracting the opposite ends of a block of tensors, the metric/arrows should either be all compatible with the rest of the network yielding periodic boundary condition (Fig. 2.14a, c), or be all opposite to the rest of the network yielding anti-periodic boundary condition (Fig. 2.14b, d). Under each boundary condition, we can find the eigenvalues for either parity even states or parity odd states. To compare the partition function or eigenvalues with a CFT's predictions, we need to look at different each boundary conditions and parity sectors separately, and choose the appropriate combinations.

2.6.3 Benchmark results

The t-V model is

$$H = \sum_n \left[-t(c_i^\dagger c_{i+1} + c_{i+1}^\dagger c_i) + V(n_i - \frac{1}{2})(n_{i+1} - \frac{1}{2}) \right], \tag{2.39}$$

where $c_i^\dagger, c_i$ are fermion creation and annihilation operators, and $n_i = c_i^\dagger c_i$ is the number operator. It is can be mapped to the XXZ model as

$$H = \sum_i \left[-2t(S_i^x S_{i+1}^x + S_i^y S_{i+1}^y) + V S_i^z S_{i+1}^z \right]. \tag{2.40}$$

We compute its energies under both periodic and anti-periodic boundary conditions using loop-GTNR with $\chi = 24$, and separate them into even and odd parity sectors. To compare results with a periodic XXZ model, we need to combine the parity even states with anti-periodic boundary condition and parity odd states with periodic boundary condition. Energies of all sectors are plotted in Fig. 2.15. Similar to the loop-TNR results for the XXZ model (Fig. 2.8), we see excellent agreement with CFT predictions when $g \equiv \arccos(-2t/V)$ is close to 0.5, which corresponds to $V = 0$, i.e. the free fermion model. Results get worse at close to $g = 0$ due to high state density, and at close to $g = 1$ due to slow convergence caused by marginally irrelevant operators.

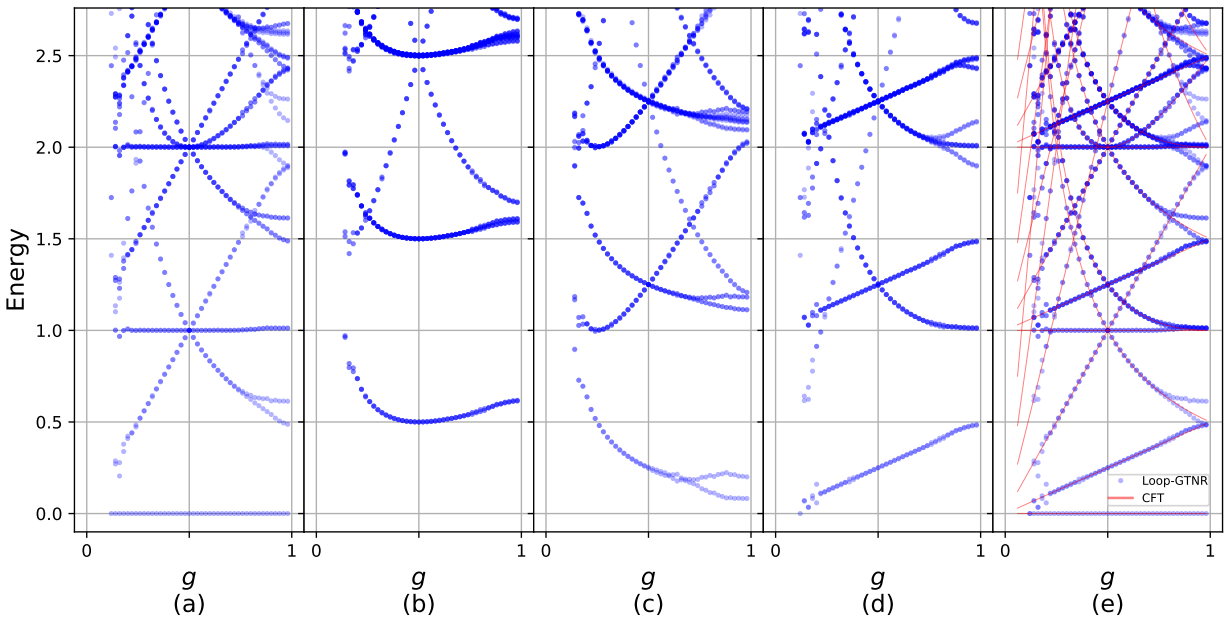

Figure 2.15: Scaled energies of the t-V model computed from $\mathcal{T}^{14}_{4,2}$ using loop-GTNR at $\chi = 24$, plotted against $g \equiv \arccos(-V/2t)$. (a) Parity even states with anti-periodic boundary condition. (b) Parity odd states with anti-periodic boundary condition. (c) Parity even states with periodic boundary condition. (d) Parity odd states with periodic boundary condition. (e) Combining states in (a) and (d), and compare with exact CFT predictions.

Chapter 3

Application: Gapless domain walls between topological phases

3.1 Introduction

Classification and construction of topological states of quantum matter have become an extremely important and intriguing direction in modern condensed matter physics recently. In the past decade, great achievements have been made toward establishing a complete paradigm for understanding topological phases of quantum matter, from the concept of long range entanglement to the classification of topological phases in interacting boson and fermion systems, with or without global symmetries [6, 9–11, 13, 22, 23, 28, 30, 41, 45, 64, 83, 86]. Nevertheless, our understanding of topological phase transitions is still very limited, especially in higher dimensions. Until very recently, it has been realized that a certain class of topological phase transitions in d_{sp} spatial dimensions can be realized as gapless domain walls between topological phases in $d_{sp}+1$ spatial dimensions [74, 75]. Such a holographic principle is very attractive since the properties of gapless domain walls are closely related to the bulk topological phases. It is even possible to establish a generic paradigm towards understanding these gapless phases systematically.

It has been known for a long time that domain walls between two topological states usually exhibit extremely interesting and intriguing properties. At the very basic level, there are two types of fundamental domain walls: gapped domain walls and gapless domain walls. The properties of gapped domain walls can be systematically studied based on the mathematical framework of unitary modular tensor category theory (UMTC) and the corresponding tunnelling matrix technique. The nature of gapped domain walls are well

understood by using the physical picture of anyon condensation [4, 38, 42, 46, 48]. On the contrary, the gapless domain walls are much more complicated and harder to understand in general.

In addition, it would be very useful to distinguish two types of gapless domain walls according to their thermal hall conductance K_H: those with $K_H \neq 0$, and those with $K_H = 0$. The edge modes of various fractional quantum hall (FQH) states are natural realizations of the former kind of gapless domain walls. (Throughout the whole chapter, we will regard vacuum as a trivial topological state. Thus, the boundary of a topological state can be regarded as a special kind of domain walls.) On the other hand, gapless domain walls with $K_H = 0$ are rather unexpected from simple physical intuitions. Very recently, the gapless conditions for $K_H = 0$ domain walls among different Abelian FQHs are established in terms of the mathematical structure of Lagrangian subsets [48]. The underlying physical nature of these gapless domain walls can be explained by global gravitational anomalies (in contrast, those domain walls with $K_H \neq 0$ carry perturbative gravitational anomalies).

In the presence of global symmetries, gaplessness may also be enforced to domain walls, even in the absence of gravitational anomalies. Most notably, gapless domains walls can be constructed between different symmetry protected topological (SPT) states [11, 34, 47, 56, 63]. For example, gapless domain walls for free fermion topological insulators/superconductors are well understood in terms of massless free Dirac/Majorana fermions, which are under intensive study both theoretically and experimentally recently. Gapless domain walls for interacting SPT states are much harder to construct and only very few special examples are known so far [12, 30, 49, 55].

Another motivation to construct and study gapless domain walls of topological phases is the novel concept of bulk-edge correspondence between topological quantum field theory (TQFT) and conformal field theory (CFT). The first concrete example is the correspondence between the 3D bulk Chern-Simons theory and the 2D boundary Wess-Zumino-Witten (WZW) model, where the space of quantum states in the bulk TQFT is identified with the space of conformal blocks of the boundary CFT [93]. Such correspondence can be viewed as an implementation of the holographic principle [68, 71] and serves as the best known example of AdS-CFT duality. (It is well known that (2+1)D quantum gravity is dual to a Chern-Simons theory by taking the phase space to be the moduli space of all flat connections [92] and a more rigorous study comparing Chern-Simon/WZW and AdS_3/CFT_2 dualities shows that the former correspondence appears as a sector inside the latter one [31].)

Experimentally, the discovery of fractional quantum Hall effect (FQHE) gives rise to much deeper physical understanding of the bulk-edge correspondence, where the appear-

ance of boundary exclusion statistics is associated with the corresponding CFT [58] which have their origin from anyonic excitations [3, 32] with fractional statistics. Mathematically, UMTC provides a general framework for describing anyons and fractionalization [43], and can also be used to construct TQFT [76]. A natural setup to further study this bulk-edge correspondence is the interface of different topological orders. Apparently, the interface is particularly interesting, since it is where different anyons in the two bulk topological phases meet. Understanding the dynamics of such "anyon meetings" can give us insights into the structure of tensor category theory and topological orders.

In this chapter, we systematically construct lattice models of gapless domain walls with $K_H = 0$ and vanishing of global gravitational anomaly between twisted and untwisted gauge theories. Such kind of gapless domain walls are closely related to bulk topological phase transitions and can be constructed in arbitaray dimensions. (Gapless domain walls with gravitational anolamly can only be realized as a surface theory, thus they have nothing to do with bulk phase transition theories.) As a simple example, we illustrate the major steps of constructing such a gapless domain wall between the toric code model and double semion model. Then we study the domain wall model using loop-TNR algorithm. Surprisingly, we find that the low energy spectrum of the domain wall model is consistent with the $su(2)_1$ Wess-Zumino-Witten model even in the absence of global $SU(2)$ symmetry. We also find a bulk picture to understand the emergence of the $su(2)_1$ CFT on the domain wall. We further study such kind of gapless domain walls between twisted and untwisted $\mathbb{Z}_N$(with $N < 6$) gauge models in $2+1$D and find all of them perfectly agree with Luttinger liquid theory. Finally, we show how to generalize such constructions of gapless domain walls between twisted and untwisted gauge theory models with arbitrary gauge group G and in higher dimensions.

On the other hand, according to the correspondence between twisted gauge theories and SPT models [49], such kind of gapless domain walls also naturally arises on the interface between the trivial and non-trivial SPT states, provided the global symmetry on the domain wall is not broken spontaneously. From SPT point of view, the gapless nature of the domain walls is closely related to gauge anomaly which can be systematically classified and constructed via group cohomology theory in arbitrary dimensions [11, 30]. We conjecture that some universal properties of these gapless domain walls could are also related to group cohomology theory.

The rest of the chapter is organized as follows. In Sec. 3.2, we start with a simple example - the gapless domain walls between toric code model and double semion model. We find a conformal field theory (CFT) described by the orbifold double $su(2)_1$ Wess-Zumino-Witten model even in the absence of global $SU(2)$ symmetry for such a gapless domain wall. We also study the physical mechanism for the gapless nature of domain wall models.

In Sec. 3.3, we review group cohomology and its role in the systematic classification and construction of domain walls between twisted and untwisted gauge theories. We further study examples with $\mathbb{Z}_N$ ($N < 6$) gauge group and find all these gapless domain wall models can be described by Luttinger liquid theory with suitable parameters. Finally, there will be a conclusion and a discussion on how to generalize these gapless domain wall models into higher dimensions.

3.2 A simple example: gapless domain wall between $\mathbb{Z}_2$ gauge model and twisted $\mathbb{Z}_2$ gauge model

3.2.1 $\mathbb{Z}_2$ gauge model and twisted $\mathbb{Z}_2$ gauge model

Let us begin with the $\mathbb{Z}_2$ quantum double model and twisted quantum double model, namely, the toric code model [44] and the doubled semion model [51]. They can be defined as spin-1/2 systems on a honeycomb lattice where spins live on links. The Hamiltonians are (Fig. 3.1)

$$\begin{aligned} H_{\text{t.c.}} &= -\sum_v Q_v - \sum_p \left(\prod_{l\in p} \tau_l^x \right) P_p \\ H_{\text{d.s.}} &= -\sum_v Q_v - \sum_p \left(\prod_{l\in p} \tau_l^x \prod_{l\in \text{legs of } p} i^{\frac{1+\tau_l^z}{2}} \right) P_p \end{aligned} \tag{3.1}$$

where v, p, l denote a vertex, a plaquette, and a link respectively, and

$$Q_v = \prod_{l\in v} \tau_l^z, \qquad P_p = \prod_{v\in p} \frac{1+Q_v}{2} \tag{3.2}$$

Here $\prod_{l\in p} \tau_l^x$ is the product of the τ_l^x around a plaquette p and $\prod_{l\in v} \tau_l^z$ is the product of the τ_l^z around a vertex v. These two models are simplest examples of string-net models [51].

The ground state $|\Psi_{\text{t.c.}}\rangle$ of $H_{\text{t.c.}}$ is exactly known since all the plaquette terms and vertex terms commute with each other. The string language provides us with a very intuitive way to understand the ground state wave function: we interpret the $\tau_l^z = -1$ and $\tau_l^z = 1$ states on a single link as the presence or absence of a string. (This string is literally an electric flux line in the $\mathbb{Z}_2$ gauge theory.) The appropriate low energy Hilbert space is made up of

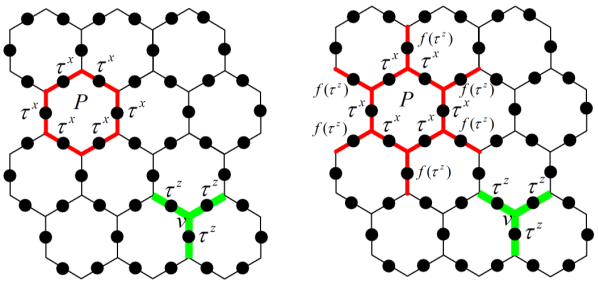

Figure 3.1: The toric code model and doubled semion model $H_{\text{t.c.}}$, $H_{\text{d.s.}}$ (3.1). For both models, the first term Q_v is a product of τ_l^z on the three links connected to the vertex v, the second term is a product of τ_l^x on the six links in the plaquette, functions $f(\tau_l^z)$ on the six links connected to the plaquette, and projector P_p. (a) $f(x) = 1$ (trivial) for the toric code model. (b) $f(x) = i^{(1+x)/2}$ for the doubled semion model.

closed string states that satisfy $\prod_{l\in v} \tau_l^z = 1$ at every vertex. The ground state is simply a superposition of all closed string states:

$$|\Psi_{\text{t.c.}}\rangle = \sum_{X\text{closed}} |X\rangle, \tag{3.3}$$

Such a model realizes the simplest topologically ordered state in 2D. If we put the ground state wave function Eq. (3.3) on a torus, there are four different topological sectors, characterized by even/odd number of large strings wrapping around a torus in both directions. Moreover, the $\mathbb{Z}_2$ electric charge e can be described as the ends of a string, which are bosons and are created/annihilated in pairs.

$H_{\text{d.s.}}$ is a less well-known model, which has the same number of ground state degeneracy on torus, but exhibits a different kind of topological order. The low energy Hilbert space of the model is again made up of closed string states. However, the ground state wavefunction of this model is very similar to the toric code wavefunction except that different closed string states are weighted by different phase factors:

$$|\Psi_{\text{d.s.}}\rangle = \sum_{X\text{closed}} (-)^{n(X)} |X\rangle \tag{3.4}$$

where n is the number of closed loops in the closed-string state X. The $(-)^{n(X)}$ phase factor makes the $\mathbb{Z}_2$ electric charge(described as the ends of string) carry semion statistics.

The above two models can be mapped to $\mathbb{Z}_2$ gauge models and twisted $\mathbb{Z}_2$ gauge models on dual triangular lattices [49]. Edges of the triangular lattice are perpendicular to edges

of the original honeycomb lattice. Spins on the edges are mapped accordingly. Centers of hexagonal plaquettes in the honeycomb lattice correspond to vertices of the triangular lattice. We put additional spins on these vertices. For each new spin, associate a gauge transformation

$$W_p = \sigma_p^x \prod_q \mu_{pq}^x \tag{3.5}$$

where p labels a vertex in the triangular lattice and pq labels the edge connecting p and q, so that dimension of the physical Hilbert space remains the same. Operator mapping compatible with the gauge transformation is then found to be

$$\tau_l^z = \sigma_p^z \sigma_q^z \mu_{pq}^z, \quad \tau_l^x = \mu_{pq}^x. \tag{3.6}$$

The resulting Hamiltonians reads (see Fig. 3.2)

$$\begin{aligned} H_0 &= -\sum_{\langle pqr \rangle} \mu_{pq}^z \mu_{qr}^z \mu_{rp}^z - \sum_p \sigma_p^x O_p \\ H_1 &= -\sum_{\langle pqr \rangle} \mu_{pq}^z \mu_{qr}^z \mu_{rp}^z - \sum_p B_p O_p \\ O_p = \prod_{\langle pqr \rangle} \frac{1 + \mu_{pq}^z \mu_{qr}^z \mu_{rp}^z}{2}, &\quad B_p = \sigma_p^x \prod_{\langle pqq' \rangle} i^{\frac{1+\sigma_q^z \mu_{qq'}^z \sigma_{q'}^z}{2}} \end{aligned} \tag{3.7}$$

where the product runs over six triangles adjacent to the vertex p. Apparently, μ_{pq}^z can be regarded as the $\mathbb{Z}_2$ gauge connection. Both H_0 and H_1 are invariant under the $\mathbb{Z}_2$ gauge transformation.

3.2.2 Operator algebra for the domain wall between toric code model and double semion model

We now consider a system whose upper half plane is described by the toric code model and lower half plane is described by the doubled semion model. All local terms of the Hamiltonian commute with each other except on the domain wall. Denote the plaquette operators in the Hamiltonian Eq. (3.1) as

$$\begin{aligned} B_p^{\text{t.c.}} &= \prod_{l \in p} \tau_l^x \\ B_p^{\text{d.s.}} &= \prod_{l \in p} \tau_l^x \prod_{l \in \text{legs of } p} i^{\frac{1+\tau_l^z}{2}} \end{aligned} \tag{3.8}$$

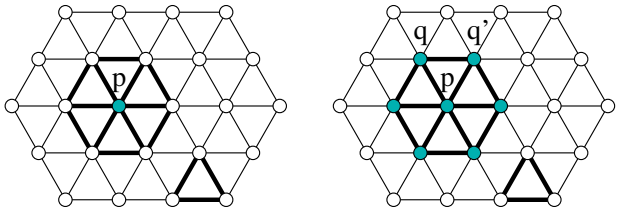

Figure 3.2: $\mathbb{Z}_2$ gauge models H_0, H_1 (3.7). (a) For H_0, the first term of the Hamiltonian is a gauge flux term $\mu^z_{pq}\mu^z_{qr}\mu^z_{rp}$ on the three links of the triangle $\langle pqr\rangle$, and the second term is a product of σ^x_p and a projector O_p that acts on the six triangles adjacent to p. (b) For H_1, the first term is the same gauge flux term, and the second term is more complex B_pO_p.

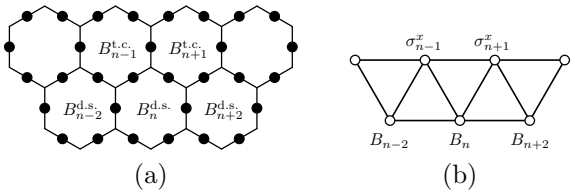

Figure 3.3: (a) Domain wall between the toric code and doubled semion model; (b) Effective domain wall between H_0 and H_1.

and label the plaquettes on the domain wall in a sequential order as shown in Fig. 3.3a. The nontrivial Hamiltonian algebra on the domain wall can be written as

$$\begin{aligned} \left(B^{\text{t.c.}}_n\right)^2 = 1, \quad \left(B^{\text{d.s.}}_n\right)^2 = 1 \\ \left[B^{\text{t.c.}}_m, B^{\text{d.s.}}_n\right] = 0, \quad \text{when } |m-n|>1 \\ B^{\text{t.c.}}_n B^{\text{d.s.}}_{n\pm1} = -B^{\text{d.s.}}_{n\pm1} B^{\text{t.c.}}_n \tau^z_{n-1,n+1}\tau^z_{n\pm1,n\pm2} \end{aligned} \tag{3.9}$$

where $\tau^z_{m,n}$ denotes the spin operator on the edge in between plaquettes m and n. Unfortunately, the above Hamiltonian algebra is very complicated and can not be solved in a easy way. On the other hand, this domain wall model and its operator algebra can be easily translated to the $\mathbb{Z}_2$ gauge models through mappings defined in the previous section (see Fig. 3.3b):

$$\begin{aligned} \left(\sigma^x_n\right)^2 = 1, \quad \left(B_n\right)^2 = 1 \\ \left[\sigma^x_m, B_n\right] = 0, \quad \text{when } |m-n|>1 \\ \sigma^x_n B_{n\pm1} = -B_{n\pm1}\sigma^x_n\sigma^z_{n\mp1}\sigma^z_{n\pm2}\mu^z_{n-1,n+1}\mu^z_{n\pm1,n\pm2} \end{aligned} \tag{3.10}$$

3.2.3 Gauge fixing and connections to domain wall models between SPT phases

We would like to simplify the Hamiltonian algebra Eq. (3.10) in the low energy sector by choosing a convenient gauge and fix all spins on edges. The $\mathbb{Z}_2$ flux terms $-\mu^z_{pq}\mu^z_{qr}\mu^z_{rp}$ commute with all other terms in both H_0 and H_1, hence always represent an independent finite energy change. Therefore, we expect the low energy physics of a gapless domain wall to be entirely captured in the subspace where $\mu^z_{pq}\mu^z_{qr}\mu^z_{rp} = 1$, i.e. no local $\mathbb{Z}_2$ flux. We will show later that the domain wall is indeed gapless. The simplest configuration with no local gauge flux is $\mu^z_{pq} \equiv 1$. Given any eigenstate of $\{\mu^z_p\}$ with no local gauge flux, the uniform $\mu^z_{pq} \equiv 1$ configuration can be achieved by applying gauge transformations if and only if there is no global gauge flux going through the domain wall, or equivalently in the string-net language, when there is no global string crossing the domain wall. We will henceforth assume this is the case and use the uniform gauge.

Under this uniform gauge, the domain wall Hamiltonian algebra simplifies to

$$\begin{gathered}(\sigma^x_n)^2 = 1, \quad (\bar{B}_n)^2 = 1 \\ \left[\sigma^x_m, \bar{B}_n\right] = 0, \quad \text{when } |m-n| > 1 \\ \sigma^x_n \bar{B}_{n\pm1} = -\bar{B}_{n\pm1}\sigma^x_n\sigma^z_{n\mp1}\sigma^z_{n\pm2}\end{gathered} \tag{3.11}$$

Such a Hamiltonian algebra can naturally arises on the domain wall between the trivial and non-trivial $\mathbb{Z}_2$ SPT phases. The corresponding bulk Hamiltonians are simply those of the gauge models H_0, H_1 with only spins on vertices and without gauge fields on edges (Fig. 3.4)

$$\begin{gathered}\bar{H}_0 = -\sum_p \sigma^x_p, \qquad \bar{H}_1 = -\sum_p \bar{B}_p \\ \bar{B}_p = \sigma^x_p \prod_{\langle pqq'\rangle} i^{\frac{1+\sigma^z_q\sigma^z_{q'}}{2}}.\end{gathered} \tag{3.12}$$

where the product runs over all six triangles $\langle pqq'\rangle$ containing p. Both systems have spin-flip $\mathbb{Z}_2$ global symmetry $S = \prod_p \sigma^x_p$ inherited from the gauge symmetry, and both have commuting local terms and unique ground states. Specifically, ground state wave functions are

$$\begin{aligned}|\Psi_0\rangle &= \sum_{\{\alpha_p\}} |\{\alpha_p\}\rangle \\ |\Psi_1\rangle &= \sum_{\{\alpha_p\}} (-1)^{N_{dw}} |\{\alpha_p\}\rangle\end{aligned} \tag{3.13}$$

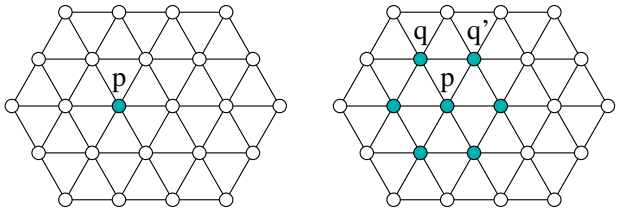

Figure 3.4: Spin models H_0, H_1 (3.12). (a) H_0 is a sum of all σ_p^x. (b) H_1 is a sum of $\bar{B}_p = \sigma_p^x \prod_{\langle pqq' \rangle} i^{\frac{1+\sigma_q^z \sigma_{q'}^z}{2}}$, where the product runs over six triangles $\langle pqq' \rangle$ adjacent to site p.

where $\{\alpha_p\}$ is a spin configuration in σ_p^z eigenbasis with $\alpha_p = \uparrow$ or $\downarrow$, and N_{dw} is the number of domain walls between spin up and down regions.

As shown in Ref. [49], these two spin models realize the only two short range entangled bosonic phases with onsite $\mathbb{Z}_2$ symmetry. We can, in fact, start from these two SPT models and follow the gauge coupling procedures specified in Ref. [49] to obtain the $\mathbb{Z}_2$ gauge models H_0, H_1. On the other hand, the domain wall models between the two SPT models $\bar{H}_0$ and $\bar{H}_1$ satisfy the Hamiltonian algebra Eq. (3.11) automatically.

3.2.4 Effective Hamiltonian with the same operator algebra

The Hamiltonian algebra of the gauge-fixed flux free domain wall decouples from the bulk terms, so it can be realized on a purely 1+1D spin model. We can straightforwardly check that the following mapping to virtual spin operators $\{\bar{\tau}_n^x, \bar{\tau}_n^y, \bar{\tau}_n^z\}$ preserves this algebra Eq. (3.11)

$$\begin{aligned} \sigma_n^x &= \frac{1}{\sqrt{2}} \left(\bar{\tau}_n^y + \bar{\tau}_{n-1}^z \bar{\tau}_n^x \bar{\tau}_{n+1}^z \right) \\ \bar{B}_n &= \frac{1}{\sqrt{2}} \left(\bar{\tau}_n^y - \bar{\tau}_{n-1}^z \bar{\tau}_n^x \bar{\tau}_{n+1}^z \right) \\ \sigma_n^z &= \bar{\tau}_n^z \end{aligned} \tag{3.14}$$

In particular, we verify that

$$\begin{aligned}
&\sigma_n^x \bar{B}_{n+1} \\
=&\frac{1}{2}\left(\bar{\tau}_{n+1}^y + \bar{\tau}_n^z \bar{\tau}_{n+1}^x \bar{\tau}_{n+2}^z\right)\left(\bar{\tau}_n^y - \bar{\tau}_{n-1}^z \bar{\tau}_n^x \bar{\tau}_{n+1}^z\right) \\
=&-\frac{1}{2}\left(\bar{\tau}_{n+1}^y - \bar{\tau}_n^z \bar{\tau}_{n+1}^x \bar{\tau}_{n+2}^z\right)\bar{\tau}_{n+2}^z \bar{\tau}_{n-1}^z \left(\bar{\tau}_{n-1}^z \bar{\tau}_n^x \bar{\tau}_{n+1}^z + \bar{\tau}_n^y\right) \\
=&-\bar{\tau}_{n-1}^z \bar{\tau}_{n+2}^z \bar{B}_{n+1} \sigma_n^x
\end{aligned} \tag{3.15}$$

We further unitarily transform the operators with $U = \prod' \bar{\tau}_n^y$, where the product runs over every other site on the domain wall. This makes all $\bar{B}_n$'s and σ_n's take the same form and enhances translational symmetry of the effective Hamiltonian, which takes the final form

$$H_{\mathrm{dw}} = -\frac{1}{\sqrt{2}} \sum_n \left(\bar{\tau}_n^y + \bar{\tau}_{n-1}^z \bar{\tau}_n^x \bar{\tau}_{n+1}^z\right) \tag{3.16}$$

We will henceforth refer to this model as the *Ising domain wall* model. This model has a $\mathbb{Z}_2$ symmetry

$$S_{\mathrm{dw}} = \prod_n \bar{\tau}_n^x \prod_n \exp\left[\frac{i\pi}{4}\left(\bar{\tau}_n^z \bar{\tau}_{n+1}^z - \bar{\tau}_n^z - 1\right)\right], \tag{3.17}$$

which we will show in Sec. 3.3 is indeed the $\mathbb{Z}_2$ symmetry inherited from the gauge symmetry in the bulk. This symmetry also acts as a self-dual transformation, as it transform the two terms $\bar{\tau}_n^y$ and $\bar{\tau}_{n-1}^z \bar{\tau}_n^x \bar{\tau}_{n+1}^z$ into each other. We introduce an adjustable parameter g into H_{dw} and transform this more general model with S_{dw}:

$$H_{\mathrm{dw}}(g) = -\frac{1}{\sqrt{2}} \sum_n \left(g\bar{\tau}_n^y + \bar{\tau}_{n-1}^z \bar{\tau}_n^x \bar{\tau}_{n+1}^z\right) \tag{3.18}$$

$$S_{\mathrm{dw}}^\dagger H_{\mathrm{dw}}(g) S_{\mathrm{dw}} = g H_{\mathrm{dw}}(1/g) \tag{3.19}$$

We see that the spectrum of $H_{\mathrm{dw}}(g)$ and $H_{\mathrm{dw}}(1/g)$ is the same up to a factor of g, which makes $g = 1$ a self-dual point. The spectrum of such a self-dual model is likely to be critical. On the other hand, since the flux free Hamiltonian algebra Eq. (3.11) is also realized as the domain wall between a trivial and a non-trivial $\mathbb{Z}_2$ SPT phases, it is natural to expect such a domain wall model to be gapless if the global $\mathbb{Z}_2$ symmetry is not spontaneously broken.

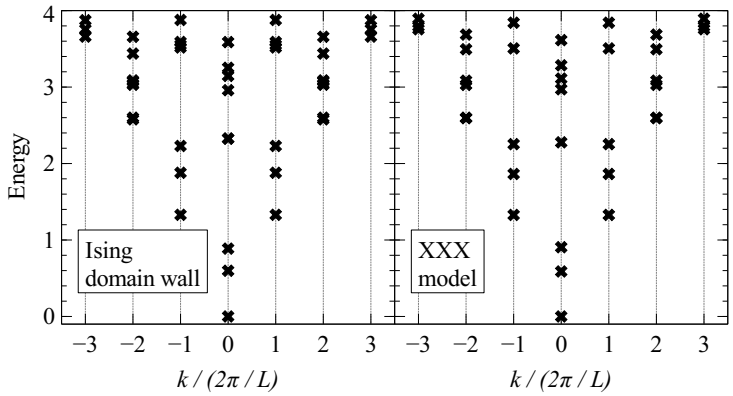

Figure 3.5: Low energy spectra of Ising domain wall and XXX model at size of 30 sites.

3.2.5 Numerical calculations

We now perform numerical calculations on the Ising domain wall model H_{dw} in Eq. (3.16). We show strong evidence that the model is indeed critical. More precisely, our numerical evidence shows that the low-energy physics is described by the $su(2)_1$ WZW theory, or equivalently the compactified free boson CFT at the self-dual radius.

We perform both exact diagonalization for small system size and loop-TNR calculation for larger system size. For comparison, we also perform numerical calculations on the spin-1/2 XXX Heisenberg chain

$$H_{XXX} = \sum_n \left(\sigma_n^x \sigma_{n+1}^x + \sigma_n^y \sigma_{n+1}^y + \sigma_n^z \sigma_{n+1}^z\right), \tag{3.20}$$

which is known to be described by the $su(2)_1$ WZW conformal field theory at low energy.

We first compute low energy spectra of both models H_{dw} and H_{XXX} by exact diagonalization. In Fig. 3.5, the lowest eigenenergies of the two models on a periodic spin chain at the size of 30 sites are plotted against corresponding lattice momenta. Both models have a typical CFT excitation tower with linear dispersion, and an identification of low energy states between the two models is clear. Starting from the ground state, degeneracies of the first few energy levels are $\{1, 3, 1, 6, 6, \dots\}$ in both models. When computing lattice momenta, we used only three-site translations for the Ising domain wall model and two-site translations for the XXX model. Using a finer translational symmetry in either model would cause the unique excitation tower at $k = 0$ to split into three/two towers at different momenta, making comparisons difficult.

The $su(2)_1$ WZW theory is equivalent to a free compactified boson at the self-dual radius. A general formula for scaling dimensions of the compactified free boson CFT is

$$\Delta_{m,n} = \frac{1}{2}\left(\rho^2 m^2 + \frac{n^2}{\rho^2}\right), \quad m, n \in \mathbb{Z}. \tag{3.21}$$

where m, n labels different primary fields and ρ is the compactification radius. In addition to states with the above scaling dimensions, there are also states corresponding to the current operator as well as its powers and derivatives. The scaling dimensions of the latter states are all integers. More discussions on free compactified boson is given in Appendix D. At self-dual radius $\rho = 1$, low lying scaling dimensions of all quasi-primaries are $\{0, 0.5, 1.0, 1.5, 2.0, 2.5, \dots\}$ with degeneracies $\{1, 4, 6, 8, 17, 28, \dots\}$. Finite size excitation energies should be proportional to scaling dimensions as $E_i = 2\pi v \Delta_i / L$, but this correspondence can hardly be observed in our exact diagonalization result (Fig. 3.5). This large deviation from CFT prediction is well understood for the XXX model, where marginally irrelevant fields cause strong finite size effects that fall off only logarithmically with increasing system size [1]. We expect a similar logarithmic convergence for the Ising domain wall.

To access larger system size, we next use loop-TNR to compute the central charge and scaling dimensions of both the Ising domain wall and the XXX model. Results are shown in Fig. 3.6. The system size grows exponentially with iteration steps in loop-TNR, hence the logarithmic convergence of the finite size effect is translated into a power law, which is indeed observed in Fig. 3.6 for both models. Even though full convergence cannot be reached before numerical errors drive the system away from the RG fixed point, we can still identify each scaling dimension's corresponding exact values based on their trend, and recover the correct degeneracies in the expected convergence limit.

Finally, we deform the Ising domain wall model without breaking its anomalous global $\mathbb{Z}_2$ symmetry (3.17), and see how scaling dimensions change with the deformation. To find such a suitable deformation, it is easier to first make a unitary transformation

$$U = \prod_n \exp\left[\frac{i\pi}{8}\left(\bar{\tau}_n^z - \bar{\tau}_n^z \bar{\tau}_{n+1}^z\right)\right] \prod_n \bar{\tau}_n^x. \tag{3.22}$$

The transformed Hamiltonian can then be written as a special case of a more general class

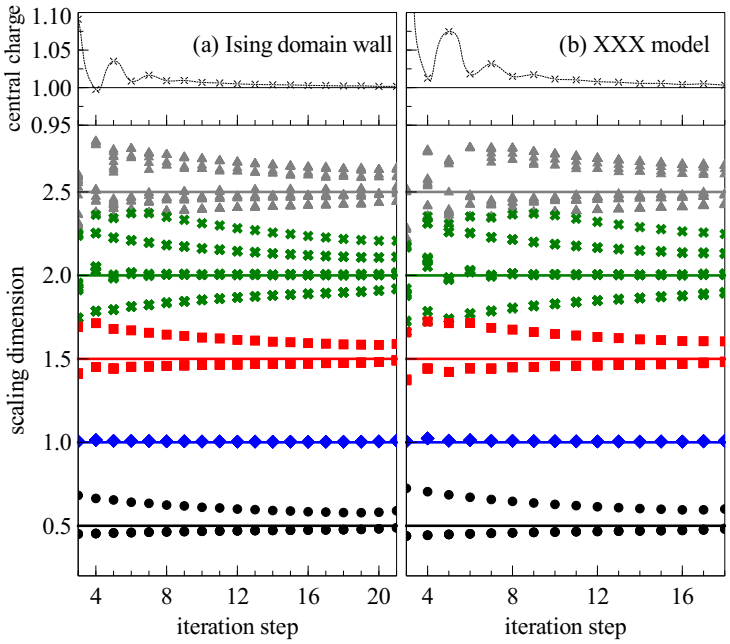

Figure 3.6: Central charge and first 63 nonzero scaling dimensions of Ising domain wall and XXX model computed using loop-TNR. The effective system size grows exponentially with iteration steps. Data points are marked with distinct markers and colors based on their expected converged values. Corresponding exact values of $su(2)_1$ WZW model are shown as solid lines. The correct degeneracies of $\{4, 6, 8, 17, 28\}$ are recovered in the expected convergence limit.

of Hamiltonians all sharing one $\mathbb{Z}_2$ symmetry:

$$H'_{\text{dw}}(g) = \frac{1}{2}\sum_n \left[1 - \bar{\tau}^z_{n-1}\bar{\tau}^z_{n+1} + g\left(\bar{\tau}^z_{n-1} + \bar{\tau}^z_{n+1}\right)\right]\bar{\tau}^x_n$$
$$S'_{\text{dw}} = \prod_n \bar{\tau}^x_n \prod_n \exp\left[\frac{i\pi}{4}\left(\bar{\tau}^z_n\bar{\tau}^z_{n+1} - 1\right)\right] \tag{3.23}$$

In particular, $H'_{\text{dw}}(g=1)$ is the transformed Ising domain wall model, and $H'_{\text{dw}}(g=0)$ is unitarily equivalent to the XY model

$$U' = \prod_n \bar{\tau}^x_{4n}\bar{\tau}^x_{4n+1} \prod_n e^{\frac{i\pi}{4}\left(\bar{\tau}^z_{2n}\bar{\tau}^z_{2n+1} - \bar{\tau}^z_{2n}\right)} e^{-\frac{i\pi}{4}\bar{\tau}^x_{2n}} e^{\frac{i\pi}{4}\bar{\tau}^y_{2n+1}}$$
$$U'^{\dagger} H'_{\text{dw}}(0) U' = \sum_n \left(\bar{\tau}^x_n\bar{\tau}^x_{n+1} + \bar{\tau}^y_n\bar{\tau}^y_{n+1}\right) \tag{3.24}$$

which is known to realize the $\rho = \frac{1}{\sqrt{2}}$ compactified free boson CFT. We compute scaling dimensions of this deformed Ising domain wall model for $0 \leq g \leq 1$, and find excellent agreement with compactified boson CFT with $\frac{1}{\sqrt{2}} \leq \rho \leq 1$ (Fig. 3.7). It is known that for a free boson CFT with $\rho \neq 0.5$, changing ρ is the only relevant direction that preserves both conformal symmetry and $c = 1$ [24]. We have therefore rather conclusively shown that the Ising domain wall indeed realizes the compactified free boson CFT at self-dual radius.

3.2.6 A physical picture for the gapless nature of the domain wall

The domain wall between the toric code and double semions can be alternatively viewed as the boundary of a stacking system of the two. It is then interesting to investigate the bulk properties of the stacking system and how they relate to the boundary domain wall.

We note that the toric code model has four types of anyons $1, e, m, f \equiv em$, where e, m are bosons and the bound state fm is a fermion. While the double semion model also has four types of anyons $1, s, \bar{s}, b \equiv s\bar{s}$, where s and $\bar{s}$ are semions and the bound state b is a boson. It is well known the toric code model admits a gapped boundary in general since we can condense the Lagrangian subset $(1, e)$ or $(1, m)$. Similarly, the double semion model also admits a gapped boundary since we can condense the Lagrangian subset $(1, b)$. Therefore, the stacking systems has sixteen types anyons described by $(1, e, m, f) \otimes (1, s, \bar{s}, b)$. In general, it also admits gapped boundary by condensing the Lagrangian subsets $(1, e) \otimes (1, b) = (1, e, b, eb)$ or $(1, m) \otimes (1, b) = (1, m, b, mb)$.

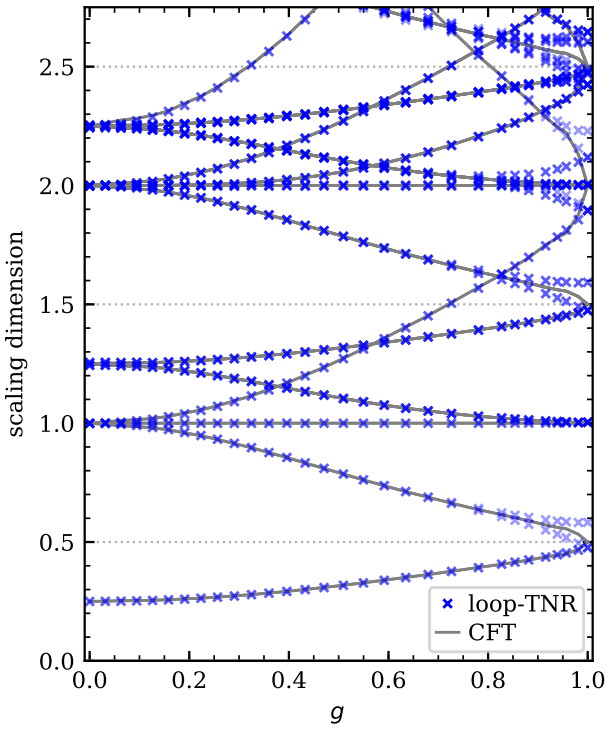

Figure 3.7: Scaling dimensions of deformed Ising domain wall models (3.23) and corresponding best fit compactified boson CFT predictions (3.21). Best fit compactification radius $\rho \in [\frac{1}{\sqrt{2}}, 1]$. Agreement is excellent except near $g = 1$ where convergence is poor, probably due to large marginally irrelevant operators.

Then what is the mechanism that protects the gapless nature of the domain wall? What makes the domain wall model so special such that it is an $su(2)_1$ WZW CFT? For the first question, a quick answer can be achieved by ungauging the $\mathbb{Z}_2$ gauge symmetry in both models and mapping the domain wall model back to a special boundary of $\mathbb{Z}_2$ SPT phase. Since both toric code model and double semion model can be regarded as the deconfinement phase of $\mathbb{Z}_2$ gauge theory, their domain wall is also in the deconfinement phase where the $\mathbb{Z}_2$ symmetry can not be spontaneously broken. Thus, the corresponding ungauged domain wall model must be a $\mathbb{Z}_2$ SPT boundary without spontaneously symmetry broken, which must be gapless. (It is well known that the boudary of $2+1$D SPT phase must be either gapless or symmetry breaking.) A more rigorous argument can be achieved by regarding the domain wall model as a specific boundary of toric code and double semion stacking systems with eb condensation while e and b are not condensed individually. Clearly, such a condition will exclude the condensation of Lagrangian subset $(1, e, b, eb)$ or $(1, m, b, mb)$ and protect the gapless nature of the boundary.

The second problem is much more subtle, and we need to analyze the anyon content for the stacking model after condensing eb. Since all the anyons with nontrivial statistics with eb are confined, the remaining anyons are consisting of one boson b (which is identified to e) and two semions $ms, m\bar{s}$ (which are identified with $f\bar{s}, fs$). Together with the identity particle, we end up with a new double semion model with four anyons $1, b, ms, m\bar{s}$, whose corresponding K matrix reads:

$$K = \begin{bmatrix} 2 & 0 \\ 0 & -2 \end{bmatrix} \tag{3.25}$$

Apparently, if it is not allowed to condense b in the deconfinement phase, there is no Lagrangian subset can be condensed in the above theory and we will end up with a $c = 1$ CFT. It is well known that the above K-matrix describes two layers of filling fraction $\nu = 1/2$ bosonic Laughlin states with opposite chirality. Since the edge theory of $\nu = 1/2$ bosonic Laughlin state is described by the chiral $su(2)_1$ WZW model, it is quite natural that the interface model can be described as the stacking of two chiral $su(2)_1$ WZW models with opposite chirality.

3.3 Constructing lattice models of general gapless domain walls

Interesting properties of the Ising domain wall motivates us to construct lattice models of domain walls between more general topological orders, and find their effective field theories. In the following, we are going to utilize the duality between string-net/gauge models and SPT phases as shown in the $\mathbb{Z}_2$ example, which can be explicitly generalized to arbitrary finite group G.

As with the $\mathbb{Z}_2$ case, a domain wall between SPT models captures the low energy physics of a corresponding domain wall between gauge models if it is gapless and has no global flux going through. For simplicity, we will focus on this flux-free case, and directly use the lattice construction of SPT phases to study domain walls between topological phases. We will see that domain walls we construct are all gapless for $G = \mathbb{Z}_N$ case.

3.3.1 Constructing SPT phases using group cocycles

We first briefly review the construction of a lattice model realizing a 2D SPT phase with finite on-site symmetry G [11].

We define our model on a triangular lattice. Each vertex is associated with a $|G|$-dim Hilbert space where local basis states $|g\rangle$ are labelled by group elements $g \in G$. The model is constructed with a branching structure on the lattice and a 3-cocycle in the group cohomology $\mathcal{H}^3(G, U(1))$. A branching structure is an assignment of arrows on all edges of the lattice such that there is no local oriented loops, which defines a natural ordering of vertices for each triangle. A 3-cocycle, for our purpose, is a function $\nu : G^4 \to U(1)$ that satisfies two conditions

$$\nu(gg_0, gg_1, gg_2, gg_3) = \nu(g_0, g_1, g_2, g_3) \tag{3.26a}$$

$$\frac{\nu(g_1, g_2, g_3, g_4)\nu(g_0, g_1, g_3, g_4)\nu(g_0, g_1, g_2, g_3)}{\nu(g_0, g_2, g_3, g_4)\nu(g_0, g_1, g_2, g_4)} = 1 \tag{3.26b}$$

for any $g, g_i \in G$. Two 3-cocycles ν, ν' are considered equivalent if they only differ by a 3-coboundary λ, i.e. $\nu' = \nu\lambda$. A 3-coboundary is a function $\lambda : G^4 \to U(1)$ that satisfies

$$\begin{gathered}\lambda(g_0, g_1, g_2, g_3) = \frac{\mu(g_1, g_2, g_3)\mu(g_0, g_1, g_3)}{\mu(g_0, g_2, g_3)\mu(g_0, g_1, g_2)} \\ \mu(gg_0, gg_1, gg_2) = \mu(g_0, g_1, g_2)\end{gathered} \tag{3.27}$$

The choice of coboundary can be thought of as a gauge freedom for cocycles. Equivalent classes of 3-cocycles form the third group cohomology $\mathcal{H}^3(G, U(1))$, which itself is an Abelian group. A more detailed introduction to group cohomology can be found in Appendix C.1.

Define a unitary transformation on the triangular lattice with a branching structure (Fig. 3.8)

$$U_\nu|\{g_i\}\rangle = \prod_{\{pqr\}} \nu^{s_{pqr}}(g_p, g_q, g_r, g^*)|\{g_i\}\rangle \tag{3.28}$$

where g^* is a fixed group element, the product runs over all triangles labelled by their three vertices pqr ordered according to the branching structure, and $s_{pqr} = \pm 1$ if the triangle has anticlockwise/clockwise orientation respectively. The Hamiltonian is defined as

$$\begin{aligned} H_\nu = -\sum_p H_p, \quad H_p = U_\nu|\phi_p\rangle\langle\phi_p|U_\nu^\dagger \\ |\phi_p\rangle = \sum_{g_p \in G} |g\rangle. \end{aligned} \tag{3.29}$$

Although U_ν acts on the entire lattice, each term of the Hamiltonian acts non-trivially only on seven neighbouring sites centred at p. Explicitly, with a branching structure as shown in Fig. 3.8,

$$\begin{aligned} &\langle g_p', g_1g_2g_3g_4g_5g_6|H_p|g_p, g_1g_2g_3g_4g_5g_6\rangle \\ =&\frac{\nu(g_4, g_5, g_p, g_p')\nu(g_5, g_p, g_p', g_6)\nu(g_p, g_p', g_6, g_1)}{\nu(g_p, g_p', g_2, g_1)\nu(g_3, g_p, g_p', g_2)\nu(g_4, g_3, g_p, g_p')}. \end{aligned} \tag{3.30}$$

This expression has been simplified using the cocycle condition (3.26b). All local terms commute, so the model is exactly solvable. It has a unique ground state

$$|\Psi_{\text{GS}}\rangle = \sum_{\{g_p\}} U_\nu|\{g_p\}\rangle. \tag{3.31}$$

Both the Hamiltonian and the ground state have the G symmetry $\{|g_p\rangle\} \to \{|gg_p\rangle\}$. Models realize distinct SPT phases if and only if they are defined by inequivalent 3-cocycles.

3.3.2 Domain walls between general SPT phases

We now use the construction in the previous section to derive domain wall models between different SPT phases with the same symmetry G.

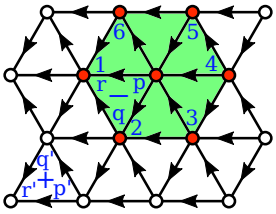

Figure 3.8: A triangular lattice with a branching structure. The ordering of vertices pqr and the orientation $s_{pqr} = \pm 1$ of a triangle are both in accordance with the branching structure. Each local term of the Hamiltonian acts on seven sites forming a hexagon.

Consider a system on a triangular lattice with the Hamiltonian

$$H = -\sum_{p\in\{\circ\}} H_p^a - \sum_{p\in\{\bullet\}} H_p^b \tag{3.32}$$

where $\{\circ\}$ and $\{\bullet\}$ denote vertices in the upper and lower half plane respectively (Fig. 3.9). Each local term $H_p^{a,b}$ acts on seven neighboring sites centered at p. H_p^a and H_p^b are defined similarly by Eq. (3.29), but use two inequivalent cocycles ν_a, ν_b. All H_p^a's commute and all H_p^b's commute, leaving the domain wall as the only nontrivial part of the system.

To explicitly decouple the domain wall from the bulk, we consider the unitary transformation

$$U_{ab} = \prod_{\{pqr\}\in\mathcal{A}} \nu_a^{s_{pqr}}(g_p, g_q, g_r, g^*) \prod_{\{p'q'r'\}\in\mathcal{B}} \nu_b^{s_{p'q'r'}}(g_{p'}, g_{q'}, g_{r'}, g^*) \tag{3.33}$$

where $\mathcal{A}$ and $\mathcal{B}$ are regions on the lattice, as shown in Fig. 3.9, that mostly represent upper and lower half planes respectively. Applying this transformation undoes most of the effect of U_ν in the construction of the bulk Hamiltonian (3.29). It changes local terms in the bulk into trivial one body interaction, leaving the domain wall explicitly decoupled. On the domain wall, the Hamiltonian transforms into

$$\begin{aligned} U_{ab}^\dagger H_p^a U_{ab} &= \sum_{g\in G} |gg_p\rangle\langle g_p| \frac{\nu_{ab}^{s_{ijk}}(g_i, g_j, g_k, g^*)}{\nu_{ab}^{s_{ijk}}(g_i, gg_j, g_k, g^*)}, \\ U_{ab}^\dagger H_p^b U_{ab} &= \sum_{g\in G} |gg_p\rangle\langle g_p| \frac{\nu_{ab}^{s_{ijk}}(g_i, gg_j, g_k, g^*)}{\nu_{ab}^{s_{ijk}}(g_i, g_j, g_k, g^*)}, \\ \nu_{ab} &\equiv \nu_a^{-1}\nu_b. \end{aligned} \tag{3.34}$$

i, j, k label a triangle whose top or bottom vertex is p, while which vertex each of them represents is assigned according to the branching structure (Fig. 3.9). Due to the group

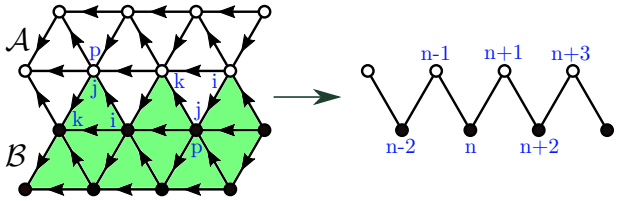

Figure 3.9: The domain wall of two SPT phases. H_p^a and H_p^b act on white and black vertices respectively. $\mathcal{A}$ denotes the white region, and $\mathcal{B}$ denotes the green shaded region.

structure of group cohomology $\mathcal{H}^3(G, U(1))$, we see that the domain wall is defined only by one 3-cocycle ν_{ab} rather than two.

In general, different branching structures lead to different domain wall models, and $H_p^{a,b}$'s can be different from one another. For concreteness, we will mostly focus on the specific branching structure shown in Fig. 3.9. This branching structure is particularly nice, since it gives us a fully translational invariant domain wall. The corresponding Hamiltonian reads

$$\begin{aligned} H &= -\sum_n H_n, \\ \langle g_n', g_{n-1}g_{n+1}|H_n|g_n, g_{n-1}g_{n+1}\rangle &= \frac{\nu_{ab}(g_{n+1}, g_n', g_{n-1}, g^*)}{\nu_{ab}(g_{n+1}, g_n, g_{n-1}, g^*)}. \end{aligned} \tag{3.35}$$

Its effective symmetry operator can also be computed

$$S_g|\{g_n\}\rangle = \prod_n \nu_{ab}^{-1}(g_{n+1}, g_n, g^{-1}g^*, g^*)|\{gg_n\}\rangle. \tag{3.36}$$

Now we have obtained a general domain wall model of 2D bosonic SPT phases. To construct an explicit model, we only need to find explicit expression of group 3-cocycles.

3.3.3 $\mathbb{Z}_N$ domain wall models

It is no coincidence that both $\mathbb{Z}_N$ gauge theories and SPT phases in 2+1D are classified by the group cohomology $\mathcal{H}^3(\mathbb{Z}_N, U(1)) \cong \mathbb{Z}_N$. We note that string-net realizations of all N distinct $\mathbb{Z}_N$ gauge theories can be constructed [53], and lattice models exist for any SPT phases with finite on-site symmetry [11].

The formula of $\mathbb{Z}_N$ 3-cocycles is well-known [59]

$$\nu_3(g_0,g_1,g_2,g_3) = \exp\left[i\frac{2\pi k}{N^2} g_{10}\left(g_{21}+g_{32}-g_{31}\right)\right] \tag{3.37}$$
$$g_{ij} \equiv (g_i - g_j) \bmod N$$
$$g_i, k \in \{0,1,\ldots,N-1\}$$

where g_i labels a group element and k labels the N different classes of 3-cocycles in $\mathcal{H}^3(\mathbb{Z}_N, U(1)) \cong \mathbb{Z}_N$. Using this formula in Eq. (3.35), we can define a $\mathbb{Z}_N$ domain wall model that is labeled by (N,k). Hamiltonians given by (N,k) and $(N,N-k)$ are related by complex conjugation, therefore there are effectively only $\lfloor N/2 \rfloor$ distinct nontrivial domain wall models for a given N.

Re-deriving the $\mathbb{Z}_2$ domain wall

The simplest nontrivial domain wall model defined by (3.35) is given by $(N,k) = (2,1)$. We expect this model to be equivalent to the Ising domain wall we studied in Sec. 3.2. The cocycle formula in this case simplifies to

$$\nu(\{g_i\}) = \begin{cases} -1, & \{g_i\} = \{0,1,0,1\} \text{ or } \{1,0,1,0\} \\ 1, & \text{otherwise} \end{cases} \tag{3.38}$$

Substituting this formula into Eq. (3.35), we find

$$H_n = \frac{1}{2}(1+\sigma^z_{n-1}+\sigma^z_{n+1}-\sigma^z_{n-1}\sigma^z_{n+1})\sigma^x_n,$$
$$S = \prod_n \sigma^x_n \prod_n \exp\left[\frac{i\pi}{4}\left(\sigma^z_n\sigma^z_{n+1}-1\right)\right], \tag{3.39}$$

which is exactly the same as Eq. (3.23) at $g=1$, hence equivalent to the Ising domain wall model.

$\mathbb{Z}_3, \mathbb{Z}_4$ and $\mathbb{Z}_5$

We numerically investigate all five distinct domain wall models as defined by (3.35) for $N = 3,4,5$.

Entanglement entropy scaling [8] of a 48-site periodic chain as computed by density matrix renormalization group (DMRG) [79, 87, 88] is plotted in Fig. 3.10. We find very

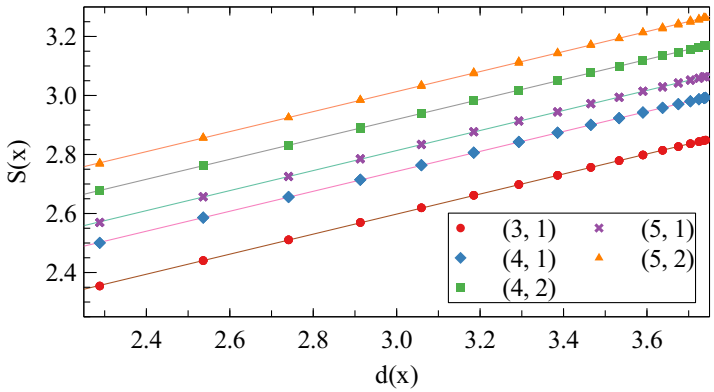

Figure 3.10: Entanglement entropy $S(x)$ of an interval of length x in the ground state of $L = 48$ periodic $\mathbb{Z}_N$ domain wall models labeled by (N, k), plotted against $d(x) = \log(\frac{L}{2\pi}\sin(\frac{x}{L}2\pi))$. Data is fitted with $S(x) = \frac{c}{3}d(x) + b$ and find $c = 1.014$–1.019 for all models.

precise logarithmic scaling that is fitted with central charge very close to 1 for all models, proving criticality of these models.

We next use loop-TNR to compute lowest virtual energies of these models, normalized such that ground state energy is $-1/12$, compatible with a $c = 1$ CFT. See Fig. 3.11. Here, we define *virtual energies* via the virtual-space transfer matrix [70] of the quantum lattice model. They are characterized by a theory relating to the original lattice model by an $\mathcal{S}$ modular transformation. See Sec. 2.5 for details.

The loop-TNR computation does not converge for the $(4, 2)$ model, but its converging behavior is very similar to that of the Ising domain wall model. We again see converging trends towards $\{0.5, 1.0, 1.5, 2.0, 2.5\}$ and degeneracies $\{4, 6, 8, 17, 28\}$ in the expected limit. We hence conjecture that it is also described by the compactified free boson CFT at self-dual radius.

The other four models' virtual energies do not match any known $c = 1$ CFT [24] (in the usual Euclidean space with the metric being the identity matrix). The gapless edge of an Abelian topological phase is expected to be described by a Luttinger liquid action [85]

$$S_{\text{edge}} = \frac{1}{4\pi}\int dtdx\,(K_{IJ}\partial_t\phi_I\partial_x\phi_J - V_{IJ}\partial_x\phi_I\partial_x\phi_J) \tag{3.40}$$

where K is an integer symmetric matrix, V is a positive definite symmetric matrix, and fields are compactified $\phi_I = \phi_I + 2\pi$. Our domain wall models can be viewed effectively

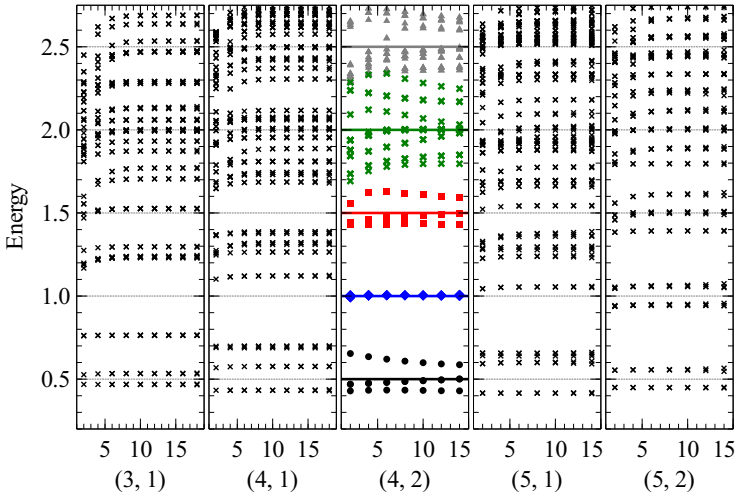

Figure 3.11: Low lying virtual energies of $\mathbb{Z}_N$ domain wall models labeled by (N, k), plotted against iteration step, which is logarithmic scale in system size. Data points for the $(4, 2)$ model are marked with different shapes and colors according to their expected convergence limits, whose values are marked with solid horizontal lines.

as special edge models. Since $c = 1$ from the entanglement entropy scaling, we expect K to be a 2×2 matrix with eigenvalues of opposite signs. In addition, since the domain wall models are effectively 1D lattice models, we required the edge theory to be modular invariant. Hence, we are led to the conclusion that by redefining the fields ϕ_I through a linear combination, we can simultaneously diagonalize both matrices with a congruent transformation such that

$$PKP^T = \begin{pmatrix} 1 & 0 \\ 0 & -1 \end{pmatrix}, \quad PVP^T = \begin{pmatrix} v_1 & 0 \\ 0 & v_2 \end{pmatrix}. \tag{3.41}$$

This diagonalized form is equivalent to two compactified massless free chiral bosons moving in opposite directions with velocities v_1 and v_2 respectively. In the usual CFT defined with the Euclidean metric, conformal invariance requires $v_1 = v_2$. In our case, $v_1 = v_2$ is in general not satisfied. For the general $v_1 \neq v_2$ case, we find that energies of highest weight states are (see Appendix D)

$$E_{m,n} = \frac{1}{2}\left(\rho^2 m^2 + \frac{n^2}{\rho^2}\right) + \frac{1 - v_r}{1 + v_r} mn, \tag{3.42a}$$

(N,k)	ρ	v_1/v_2
$(3,1)$	0.968	1.623
$(4,1)$	0.931	1.907
$(5,1)$	0.912	2.130
$(5,2)$	0.948	1.121

Table 3.1: Best fit parameters for non-conformal $\mathbb{Z}_N$ domain wall models as described by a chiral boson theory (3.42).

and energies of descendant states are

$$E_{m,n,\{n_{1,l}\},\{n_{2,l}\}} = E_{m,n} + \frac{2}{1+v_r}\sum_{l=1}^{\infty} l\left(n_{1,l} + v_r n_{2,l}\right) \tag{3.42b}$$

in units of $\pi(v_1+v_2)/L$, where $v_r = v_1/v_2$. We note that an $\mathcal{S}$ modular transformation has the effect of mapping $v_r \to 1/v_r$, which does not change the spectrum. Hence if virtual energies of a lattice model are characterized by Luttinger liquid, the lattice model itself should be described by the same theory. We proceed to fit the energies in Fig. 3.11 with Eq. (3.42) by adjusting the two free parameters ρ and v_r, and find a perfect fit for all models. The fitted values are listed in Table 3.1.

To further confirm this field theoretic description, we continuously deform the $(3,1)$ domain wall model without breaking the effective $\mathbb{Z}_3$ symmetry defined by (3.36), and connect it with a compactified free boson CFT for which $v_1 = v_2$. One such deformation is found to be

$$H_{\text{deform}}(g) = g\left(H_{(3,1)} + I\right) + (1-g)H' \tag{3.43}$$

with

$$\begin{aligned} H' &= -\sum_i H'_i \\ H'_i &= |020\rangle\langle 010| + e^{i\frac{2\pi}{3}}|101\rangle\langle 121| + e^{-i\frac{2\pi}{3}}|212\rangle\langle 202| + \text{h.c.} \end{aligned} \tag{3.44}$$

where $H_{(3,1)}$ is the domain wall Hamiltonian, and H' is a fine tuned Hamiltoninan that realizes the $\rho = \sqrt{2}/3$ compactified free boson CFT. This deformed model realizes a CFT at $g = 0$, and recovers the $(3,1)$ domain wall model (up to a constant) at $g = 1$. Virtual energies of $H_{\text{deform}}(g)$ is computed with loop-TNR for $0 \le g \le 1$ (Fig. 3.12) and fitted with the field theoretic predictions Eq. (3.42) to excellent agreement.

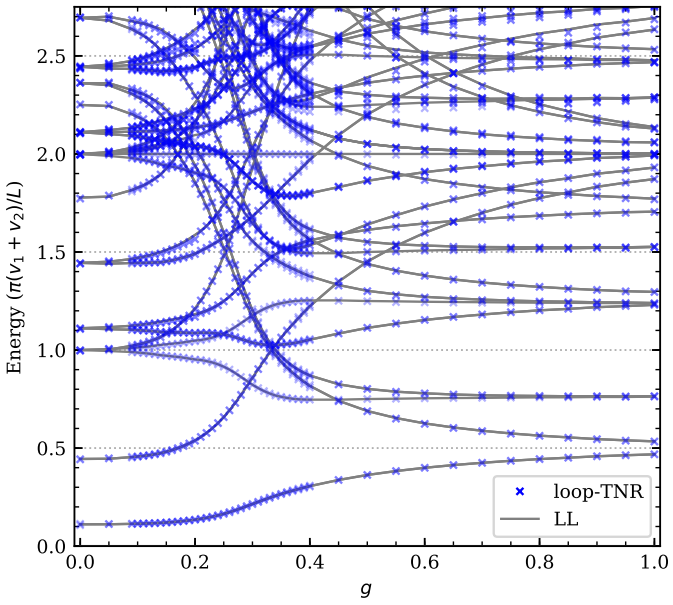

Figure 3.12: Virtual energies of $H_{\text{deform}}(g)$ and corresponding best fit Luttinger liquid (LL). States with the same quantum numbers m, n in (3.42) are connected by gray lines.

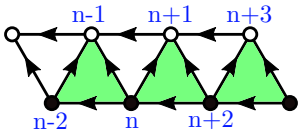

Figure 3.13: An alternative branching structure on the domain wall.

Alternative branching structure and cocycle gauges

Models we studied in the previous section all assumed a particular branching structure (Fig. 3.9) and cocycle gauge (3.37). Changing these choices amounts to a local unitary transformation in the bulk. This is inconsequential for the bulk physics, but can cause nontrivial changes on the domain wall, because the resulting local unitary transformations on the two sides may not be the same. It is important that our general conclusions remain valid for different choices of branching structures and cocycle gauges.

Consider an alternative branching structure on the domain wall, shown in Fig. 3.13. Applying this branching structure to Eq. (3.34), the new domain wall Hamiltonian for a

general group cocycle reads

$$
\begin{aligned}
H' &= -\sum_n \left(H^a_{2n} + H^b_{2n+1}\right), \\
\langle g'_n, g_{n-1}g_{n+1}|H^a_n|g_n, g_{n-1}g_{n+1}\rangle &= \frac{\nu_{ab}(g_{n+1}, g_{n-1}, g_n, g^*)}{\nu_{ab}(g_{n+1}, g_{n-1}, g'_n, g^*)}, \\
\langle g'_n, g_{n-1}g_{n+1}|H^b_n|g_n, g_{n-1}g_{n+1}\rangle &= \frac{\nu_{ab}(g_n, g_{n+1}, g_{n-1}, g^*)}{\nu_{ab}(g'_n, g_{n+1}, g_{n-1}, g^*)}.
\end{aligned}
\tag{3.45}
$$

Using the same cocycle gauge (3.37), the new $\mathbb{Z}_2$ domain wall Hamiltonian is

$$
\begin{aligned}
H^a_n &= \frac{1}{2}\left(1 - \sigma^z_{n-1} + \sigma^z_{n+1} + \sigma^z_{n-1}\sigma^z_{n+1}\right)\sigma^x_n, \\
H^b_n &= \frac{1}{2}\left(1 + \sigma^z_{n-1} - \sigma^z_{n+1} + \sigma^z_{n-1}\sigma^z_{n+1}\right)\sigma^x_n.
\end{aligned}
\tag{3.46}
$$

This is unitarily equivalent to the Ising domain wall. Explicit, Eq. (3.46) is related to Eq. (3.23) at $g = 1$ by

$$
U'' = \prod_n \exp\left(\frac{i\pi}{4}\sigma^z_{2n}\sigma^z_{2n+1}\right)\exp\left(-\frac{i\pi}{4}\sigma^z_n\right). \tag{3.47}
$$

The $\mathbb{Z}_3$ domain wall *is* changed by this new branching structure. We again compute its virtual energies, see Fig. 3.13, and find that it still fits the Luttinger liquid predictions perfectly at $\rho = 0.951, v_r = 1.416$.

Next, we keep the old branching structure in Fig. 3.9, but multiply each 3-cocycle in (3.35) with an arbitrary 3-coboundary, effectively changing the cocycle gauge. Any $\mathbb{Z}_N$ group coboundary is fully determined by N^2 independent parameters:

$$
\mu(0, m, n) = e^{i\theta_{mn}} \tag{3.48}
$$

For both $\mathbb{Z}_2$ and $\mathbb{Z}_3$, we generate 16 sets of random $\theta_{mn} \in [0, 2\pi)$, and compute virtual energies of resulting domain wall models with loop-TNR. All generated $\mathbb{Z}_2$ domain walls fit a free boson CFT with compactification radius $\rho \in [0.945, 1]$, and all generated $\mathbb{Z}_3$ domain walls fit a Luttinger liquid theory with appropriate ρ and v_1/v_2. Energies of a sample of these models are shown in Fig. 3.15 and Fig. 3.16. Best fit parameters for $\mathbb{Z}_3$ domain walls are listed in Table 3.2.

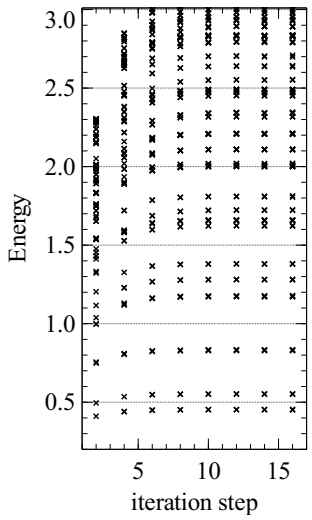

Figure 3.14: Virtual energies of the $\mathbb{Z}_3$ domain wall model with alternative branching structure (Fig. 3.13).

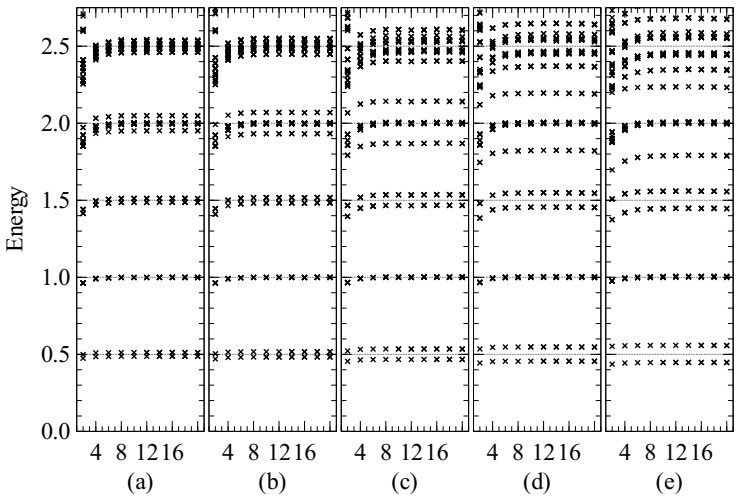

Figure 3.15: Virtual energies/scaling dimensions of $\mathbb{Z}_2$ domain walls defined with random 3-coboundaries, plotted against loop-TNR iteration number. All models match free boson CFT with compactification radius $\rho \in [0.945, 1.0]$.

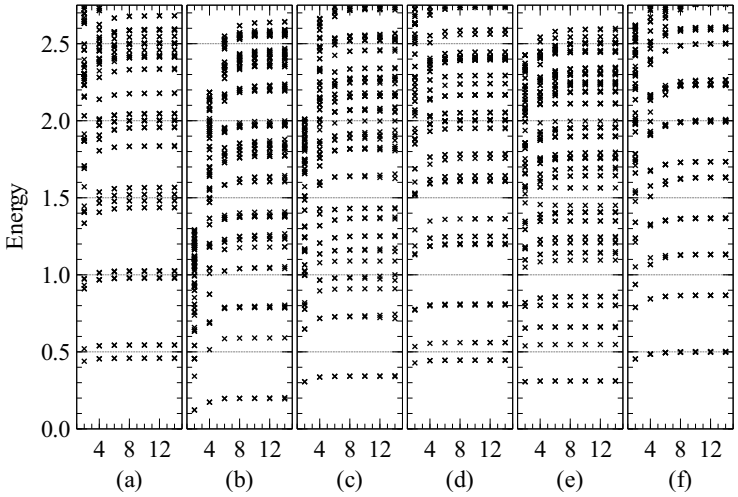

Figure 3.16: Virtual energies of $\mathbb{Z}_3$ domain walls defined with random 3-coboundaries, plotted against loop-TNR iteration number. All computed models match a Luttinger liquid/chiral boson theory with appropriate parameters (Table 3.2).

	ρ	v_1/v_2
(a)	0.958	1.045
(b)	0.631	2.391
(c)	0.827	1.201
(d)	0.945	1.490
(e)	0.789	2.652
(f)	0.998	1.307

Table 3.2: Best fit Luttinger liquid parameters for $\mathbb{Z}_3$ domain walls plotted in Fig. 3.16.

3.4 Conclusions and discussions

In conclusion, we systematically construct lattice models of gapless domain walls between twisted and untwisted gauge models with arbitrary finite group G in $2+1$D. We then use the state-of-art loop-TNR algorithm to study the $G = \mathbb{Z}_N$ case(with $N < 6$) and find all of them perfectly agree with the Luttinger liquid theory descriptions at low energy. We further provide a physical picture to understand the gapless nature of these domain walls based on the theory of Lagrangian subsets and anyon condensation.

It is straightforward to generalize our construction of gapless domain wall models into higher dimensions using the correspondence between SPT models and twisted gauge models. All we need is a branched triangulation on a higher dimensional manifold, and an appropriate region $\mathcal{A}$ (Fig. 3.9) to define the unitary transformation U'. It can be easily seen that for a higher dimensional domain wall Hamiltonian $H = -\sum_i H_i$, each local term H_i acts only on the site i and its nearest neighbors. But to write down an explicit model is rather tedious. The difficulty partly comes from the *reduced* translational and rotational symmetry when a branched triangulation is imposed on a higher dimensional manifold. Such reduced symmetry also increases the difficulty for numerical study of these models. Physically, we believe that these models still describe gapless phases since the anomalous symmetry cannot be broken on domain walls separating two deconfinement phases of gauge group G. Of course, we still need to exclude the possibility of anomalous symmetry enriched topological(SET) phases, and we will leave this interesting problem to our future works.

Outlook

In this thesis, we have discussed in details algorithms and applications of loop-TNR for the purpose of computing energies and momenta of gapless 1+1D quantum models. More generally, loop-TNR can be useful for any problem that involves optimization and contraction of 2D tensor networks. One notable area briefly discussed in [97] is the contraction of a 2D projected entangled pair state (PEPS) for the calculation of physical quantities. Loop-TNR is shown to quickly converge to an accurate value for the maximally frustrated J_1-J_2 antiferromagnetic Heisenberg model. We can straightforwardly extend this approach to fermionic systems using the loop-GTNR formalism developed in Sec. 2.6, serving as an improvement to the Grassmann tensor-entanglement renormalization group (GTERG) algorithm proposed in [27]. This generalization can serve as a new powerful numerical tool to study important 2D fermion models such as the Hubbard model.

Another exciting area where loop-TNR may shine is machine learning. It is pointed out in [57] that the Restricted Boltzmann Machine (RBM) for unsupervised deep learning can actually be regarded as a variational real-space RG scheme. It is also demonstrated that tensor networks can be effective tools for both supervised and unsupervised machine learning [33, 37, 54, 67]. Loop-TNR, being a powerful tensor network algorithm for real-space RG, may serve as a useful addition to the algorithmic toolbox of machine learning, especially for 2D image recognition or generation.

References

[1] I Affleck, D Gepner, H J Schulz, and T Ziman. Critical behaviour of spin-s heisenberg antiferromagnetic chains: analytic and numerical results. *J. Phys. A*, 22(5):511, 1989.

[2] Alexander Altland and Ben D Simons. *Condensed matter field theory*. Cambridge University Press, 2010.

[3] Daniel Arovas, J. R. Schrieffer, and Frank Wilczek. Fractional statistics and the quantum hall effect. *Phys. Rev. Lett.*, 53:722–723, Aug 1984.

[4] F. A. Bais and J. K. Slingerland. Condensate-induced transitions between topologically ordered phases. *Phys. Rev. B*, 79:045316, Jan 2009.

[5] Chenfeng Bao, Shuo Yang, Chenjie Wang, and Zheng-Cheng Gu. Lattice model constructions for gapless domain walls between topological phases. *arXiv preprint arXiv:1801.00719*, 2018.

[6] M. Barkeshli, P. Bonderson, M. Cheng, and Z. Wang. Symmetry, Defects, and Gauging of Topological Phases. *ArXiv e-prints*, October 2014.

[7] RJ Bursill, T Xiang, and GA Gehring. The density matrix renormalization group for a quantum spin chain at non-zero temperature. *Journal of Physics: Condensed Matter*, 8(40):L583, 1996.

[8] Pasquale Calabrese and John Cardy. Entanglement entropy and quantum field theory. *J. Stat. Mech. Theory Exp.*, 2004(06):P06002, 2004.

[9] X. Chen, Z.-C. Gu, and X.-G. Wen. Classification of gapped symmetric phases in one-dimensional spin systems. *Phys. Rev. B*, 83:035107, Jan 2011.

[10] X. Chen, Z.-C. Gu, and X.-G. Wen. Complete classification of one-dimensional gapped quantum phases in interacting spin systems. *Phys. Rev. B*, 84:235128, Dec 2011.

[11] Xie Chen, Zheng-Cheng Gu, Zheng-Xin Liu, and Xiao-Gang Wen. Symmetry protected topological orders and the group cohomology of their symmetry group. *Phys. Rev. B*, 87:155114, Apr 2013.

[12] Xie Chen and Xiao-Gang Wen. Chiral symmetry on the edge of 2d symmetry protected topological phases. *Phys. Rev. B*, 86:235135, 2012.

[13] M. Cheng, Z. Bi, Y.-Z. You, and Z.-C. Gu. Towards a Complete Classification of Symmetry-Protected Phases for Interacting Fermions in Two Dimensions. *arXiv e-prints*, January 2015.

[14] Clement Delcamp and Bianca Dittrich. Towards a phase diagram for spin foams. *Classical and Quantum Gravity*, 34(22):225006, 2017.

[15] Bianca Dittrich. The continuum limit of loop quantum gravity-a framework for solving the theory. *Loop quantum gravity: the first*, 30:153–179, 2017.

[16] Bianca Dittrich, Frank C Eckert, and Mercedes Martin-Benito. Coarse graining methods for spin net and spin foam models. *New Journal of Physics*, 14(3):035008, 2012.

[17] Bianca Dittrich, Sebastian Mizera, and Sebastian Steinhaus. Decorated tensor network renormalization for lattice gauge theories and spin foam models. *New Journal of Physics*, 18(5):053009, 2016.

[18] Bianca Dittrich and Sebastian Steinhaus. Time evolution as refining, coarse graining and entangling. *New Journal of Physics*, 16(12):123041, 2014.

[19] Jens Eisert, Marcus Cramer, and Martin B Plenio. Colloquium: Area laws for the entanglement entropy. *Reviews of Modern Physics*, 82(1):277, 2010.

[20] Glen Evenbly and Guifre Vidal. Tensor network renormalization. *Physical review letters*, 115(18):180405, 2015.

[21] P. Francesco, P. Mathieu, and D. Senechal. *Conformal Field Theory*. Island Press, 1996.

[22] D. S. Freed. Short-range entanglement and invertible field theories. *arXiv e-prints*, June 2014.

[23] Davide Gaiotto and Theo Johnson-Freyd. Symmetry Protected Topological phases and Generalized Cohomology. *arXiv e-prints*, December 2017.

[24] P Ginsparg. Curiosities at c= 1. *Nucl. Phys. B*, 295(2):153–170, 1988.

[25] Zheng-Cheng Gu. Efficient simulation of grassmann tensor product states. *Physical Review B*, 88(11):115139, 2013.

[26] Zheng-Cheng Gu, Hong-Chen Jiang, and G Baskaran. Emergence of $p + ip$ superconductivity in 2 d strongly correlated dirac fermions. *arXiv preprint arXiv:1408.6820*, 2014.

[27] Zheng-Cheng Gu, Frank Verstraete, and Xiao-Gang Wen. Grassmann tensor network states and its renormalization for strongly correlated fermionic and bosonic states. *arXiv preprint arXiv:1004.2563*, 2010.

[28] Zheng-Cheng Gu, Zhenghan Wang, and Xiao-Gang Wen. Classification of two-dimensional fermionic and bosonic topological orders. *Phys. Rev. B*, 91:125149, Mar 2015.

[29] Zheng-Cheng Gu and Xiao-Gang Wen. Tensor-entanglement-filtering renormalization approach and symmetry-protected topological order. *Phys. Rev. B*, 80:155131, Oct 2009.

[30] Zheng-Cheng Gu and Xiao-Gang Wen. Symmetry-protected topological orders for interacting fermions: fermionic topological nonlinear σ models and a special group supercohomology theory. *Phys. Rev. B*, 90(11):115141, 2014.

[31] Sergei Gukov, Emil Martinec, Gregory Moore, and Andrew Strominger. Chern-simons gauge theory and the ads(3)/cft(2) correspondence. *arXiv preprint hep-th/0403225*, 2004.

[32] B. I. Halperin. Statistics of quasiparticles and the hierarchy of fractional quantized hall states. *Phys. Rev. Lett.*, 52:2390–2390, Jun 1984.

[33] Zhao-Yu Han, Jun Wang, Heng Fan, Lei Wang, and Pan Zhang. Unsupervised generative modeling using matrix product states. *Physical Review X*, 8(3):031012, 2018.

[34] M. Z. Hasan and C. L. Kane. *Colloquium* : Topological insulators. *Rev. Mod. Phys.*, 82:3045–3067, Nov 2010.

[35] Markus Hauru, Clement Delcamp, and Sebastian Mizera. Renormalization of tensor networks using graph-independent local truncations. *Physical Review B*, 97(4):045111, 2018.

[36] Qi Hu, Adrian Franco-Rubio, and Guifre Vidal. Continuous tensor network renormalization for quantum fields. *arXiv preprint arXiv:1809.05176*, 2018.

[37] William James Huggins, Piyush Patil, Bradley Mitchell, K Birgitta Whaley, and Miles Stoudenmire. Towards quantum machine learning with tensor networks. *Quantum Science and Technology*, 2018.

[38] L.-Y. Hung and Y. Wan. Symmetry-enriched phases obtained via pseudo anyon condensation. *International Journal of Modern Physics B*, 28:1450172, July 2014.

[39] R Julien and F. D. M Haldane. *Bull. Am. Phys. Soc.*, 28:34, 1983.

[40] Leo P Kadanoff. Scaling laws for ising models near t c. *Physics Physique Fizika*, 2(6):263, 1966.

[41] A. Kapustin, R. Thorngren, A. Turzillo, and Z. Wang. Fermionic Symmetry Protected Topological Phases and Cobordisms. *arXiv e-prints*, June 2014.

[42] A. Kitaev and L. Kong. Models for Gapped Boundaries and Domain Walls. *Communications in Mathematical Physics*, 313:351–373, July 2012.

[43] Alexei Kitaev. Anyons in an exactly solved model and beyond. *Ann. Phys.*, 321(1):2 – 111, 2006. January Special Issue.

[44] A.Yu. Kitaev. Fault-tolerant quantum computation by anyons. *Ann. Phys.*, 303(1):2 – 30, 2003.

[45] T. Lan, L. Kong, and X.-G. Wen. Classification of 2+1D topological orders and SPT orders for bosonic and fermionic systems with on-site symmetries. *ArXiv e-prints*, February 2016.

[46] Tian Lan, Juven C. Wang, and Xiao-Gang Wen. Gapped domain walls, gapped boundaries, and topological degeneracy. *Phys. Rev. Lett.*, 114:076402, Feb 2015.

[47] M. Levin and A. Stern. Classification and analysis of two-dimensional abelian fractional topological insulators. *Phys. Rev. B*, 86:115131, Sep 2012.

[48] Michael Levin. Protected edge modes without symmetry. *Phys. Rev. X*, 3:021009, May 2013.

[49] Michael Levin and Zheng-Cheng Gu. Braiding statistics approach to symmetry-protected topological phases. *Phys. Rev. B*, 86:115109, Sep 2012.

[50] Michael Levin and Cody P Nave. Tensor renormalization group approach to two-dimensional classical lattice models. *Physical review letters*, 99(12):120601, 2007.

[51] Michael A. Levin and Xiao-Gang Wen. String-net condensation: a physical mechanism for topological phases. *Phys. Rev. B*, 71:045110, Jan 2005.

[52] Wei Li, Shou-Shu Gong, Yang Zhao, Shi-Ju Ran, Song Gao, and Gang Su. Phase transitions and thermodynamics of the two-dimensional ising model on a distorted kagome lattice. *Physical Review B*, 82(13):134434, 2010.

[53] Chien-Hung Lin and Michael Levin. Generalizations and limitations of string-net models. *Phys. Rev. B*, 89(19):195130, 2014.

[54] Ding Liu, Shi-Ju Ran, Peter Wittek, Cheng Peng, Raul Blázquez García, Gang Su, and Maciej Lewenstein. Machine learning by two-dimensional hierarchical tensor networks: A quantum information theoretic perspective on deep architectures. *arXiv preprint arXiv:1710.04833*, 2017.

[55] Zheng-Xin Liu and Xiao-Gang Wen. Symmetry protected spin quantum hall phases in 2-dimensions. *Phys. Rev. Lett.*, 110:067205, 2013.

[56] Y.-M. Lu and A. Vishwanath. Theory and classification of interacting integer topological phases in two dimensions: A chern-simons approach. *Phys. Rev. B*, 86:125119, Sep 2012.

[57] Pankaj Mehta and David J Schwab. An exact mapping between the variational renormalization group and deep learning. *arXiv preprint arXiv:1410.3831*, 2014.

[58] Gregory Moore and Nathan Seiberg. Classical and quantum conformal field theory. *Comm. Math. Phys.*, 123(2):177–254, 1989.

[59] Gregory Moore and Nathan Seiberg. Classical and quantum conformal field theory. *Communications in Mathematical Physics*, 123(2):177–254, 1989.

[60] Th Niemeijer and JMJ Van Leeuwen. Wilson theory for spin systems on a triangular lattice. *Physical Review Letters*, 31(23):1411, 1973.

[61] Román Orús. A practical introduction to tensor networks: Matrix product states and projected entangled pair states. *Annals of Physics*, 349:117–158, 2014.

[62] David Perez-Garcia, Frank Verstraete, Michael M Wolf, and J Ignacio Cirac. Matrix product state representations. *arXiv preprint quant-ph/0608197*, 2006.

[63] X.-L. Qi and S.-C. Zhang. Topological insulators and superconductors. *Rev. Mod. Phys.*, 83:1057–1110, Oct 2011.

[64] N. Schuch, D. Pérez-García, and I. Cirac. Classifying quantum phases using matrix product states and projected entangled pair states. *Phys. Rev. B*, 84:165139, Oct 2011.

[65] Yuya Shimizu and Yoshinobu Kuramashi. Critical behavior of the lattice schwinger model with a topological term at $\theta = \pi$ using the grassmann tensor renormalization group. *Physical Review D*, 90(7):074503, 2014.

[66] Yuya Shimizu and Yoshinobu Kuramashi. Grassmann tensor renormalization group approach to one-flavor lattice schwinger model. *Physical Review D*, 90(1):014508, 2014.

[67] Edwin Stoudenmire and David J Schwab. Supervised learning with tensor networks. In *Advances in Neural Information Processing Systems*, pages 4799–4807, 2016.

[68] Leonard Susskind. The world as a hologram. *J. Math. Phys.*, 36(11):6377–6396, 1995.

[69] Masuo Suzuki. Relationship between d-dimensional quantal spin systems and (d+ 1)-dimensional ising systems: Equivalence, critical exponents and systematic approximants of the partition function and spin correlations. *Progress of theoretical physics*, 56(5):1454–1469, 1976.

[70] Masuo Suzuki. Transfer-matrix method and monte carlo simulation in quantum spin systems. *Physical Review B*, 31(5):2957, 1985.

[71] Gerard 't Hooft. Dimensional reduction in quantum gravity. *arXiv preprint gr-qc/9310026*, 1993.

[72] Shinji Takeda and Yusuke Yoshimura. Grassmann tensor renormalization group for the one-flavor lattice gross–neveu model with finite chemical potential. *Progress of Theoretical and Experimental Physics*, 2015(4):043B01, 2015.

[73] Daniel C Tsui, Horst L Stormer, and Arthur C Gossard. Two-dimensional magnetotransport in the extreme quantum limit. *Physical Review Letters*, 48(22):1559, 1982.

[74] Lokman Tsui, Yen-Ta Huang, Hong-Chen Jiang, and Dung-Hai Lee. The phase transitions between $Z_n \times Z_n$ bosonic topological phases in $1+1$D, and a constraint on the central charge for the critical points between bosonic symmetry protected topological phases. *Nuclear Physics, B*, 919:470, 2017.

[75] Lokman Tsui, Fa Wang, and Dung-Hai Lee. Topological versus Landau-like phase transitions. *arXiv e-prints*, November 2015.

[76] Vladimir G. Turaev. Modular categories and 3-manifold invariants. *Int. J. Mod Phys B*, 06(11n12):1807–1824, 1992.

[77] Frank Verstraete and J Ignacio Cirac. Matrix product states represent ground states faithfully. *Physical Review B*, 73(9):094423, 2006.

[78] Frank Verstraete, Valentin Murg, and J Ignacio Cirac. Matrix product states, projected entangled pair states, and variational renormalization group methods for quantum spin systems. *Advances in Physics*, 57(2):143–224, 2008.

[79] Frank Verstraete, Diego Porras, and J Ignacio Cirac. Density matrix renormalization group and periodic boundary conditions: A quantum information perspective. *Phys. Rev. Lett.*, 93(22):227205, 2004.

[80] Guifre Vidal. Entanglement renormalization. *Physical review letters*, 99(22):220405, 2007.

[81] G Von Gehlen. Critical and off-critical conformal analysis of the ising quantum chain in an imaginary field. *Journal of Physics A: Mathematical and General*, 24(22):5371, 1991.

[82] Ling Wang, Zheng-Cheng Gu, Frank Verstraete, and Xiao-Gang Wen. Tensor-product state approach to spin-1 2 square j 1- j 2 antiferromagnetic heisenberg model: Evidence for deconfined quantum criticality. *Physical Review B*, 94(7):075143, 2016.

[83] Qing-Rui Wang and Zheng-Cheng Gu. Towards a complete classification of fermionic symmetry protected topological phases in 3D and a general group supercohomology theory. *arXiv e-prints*, March 2017.

[84] Xiaoqun Wang and Tao Xiang. Transfer-matrix density-matrix renormalization-group theory for thermodynamics of one-dimensional quantum systems. *Physical Review B*, 56(9):5061, 1997.

[85] Xiao-Gang Wen. Topological orders and edge excitations in fractional quantum hall states. *Adv. Phys.*, 44(5):405–473, 1995.

[86] Xiao-Gang Wen. Construction of bosonic symmetry-protected-trivial states and their topological invariants via $g \times so(\infty)$ nonlinear σ models. *Phys. Rev. B*, 91:205101, May 2015.

[87] Steven R White. Density matrix formulation for quantum renormalization groups. *Phys. Rev. Lett.*, 69(19):2863, 1992.

[88] Steven R White. Density-matrix algorithms for quantum renormalization groups. *Phys. Rev. B*, 48(14):10345, 1993.

[89] Steven R White and Reinhard M Noack. Real-space quantum renormalization groups. *Physical review letters*, 68(24):3487, 1992.

[90] Kenneth G Wilson. Renormalization group and critical phenomena. i. renormalization group and the kadanoff scaling picture. *Physical review B*, 4(9):3174, 1971.

[91] Kenneth G Wilson. The renormalization group: Critical phenomena and the kondo problem. *Reviews of modern physics*, 47(4):773, 1975.

[92] E. Witten. 2 + 1 dimensional gravity as an exactly soluble system. *Nucl. Phys. B*, 311:46–78, December 1988.

[93] Edward Witten. Quantum field theory and the jones polynomial. *Comm. Math. Phys.*, 121(3):351–399, 1989.

[94] F Woynarovich, H-P Eckle, and TT Truong. Non-analytic finite-size corrections in the one-dimensional bose gas and heisenberg chain. *Journal of Physics A: Mathematical and General*, 22(18):4027, 1989.

[95] Zhi-Yuan Xie, Jing Chen, Ming-Pu Qin, Jing W Zhu, Li-Ping Yang, and Tao Xiang. Coarse-graining renormalization by higher-order singular value decomposition. *Physical Review B*, 86(4):045139, 2012.

[96] Zhi-Yuan Xie, Hong-Chen Jiang, Qinjun N Chen, Zheng-Yu Weng, and Tao Xiang. Second renormalization of tensor-network states. *Physical review letters*, 103(16):160601, 2009.

[97] Shuo Yang, Zheng-Cheng Gu, and Xiao-Gang Wen. Loop optimization for tensor network renormalization. *Phys. Rev. Lett.*, 118(11):110504, 2017.

Appendix A

Review of MPS algorithms

An appealing feature of loop-TNR is that many of its steps map to well understood problems in MPS with known solutions. As such, we briefly review these relevant MPS algorithms.

An MPS is a decomposition of the coefficient tensor of a many body state (Fig. A.1a)

$$\langle\{l_n\}|\Psi\rangle \equiv \Psi_{\{l_n\}} = \sum_{\{i_n=1,\ldots,\chi_n\}} A^1_{i_0 l_1 i_1} A^2_{i_1 l_2 i_2} \cdots, \tag{A.1}$$

where l_n's are called physical legs, i_n's are called virtual legs/bonds, and χ_n's are the virtual bond dimensions. χ_n's determine the efficiency of this decomposition.

The MPS representation of a physical state is not unique due to the tensor network gauge freedom. We can exploit this freedom to put an MPS into a canonical form that is more efficient and better suited for approximations.

Open boundary condition

An N-body MPS with open boundary condition (OBC-MPS) has $n = 1, \ldots, N$ and fixed i_0, i_N in (A.1). In this case, finding the optimal bond dimension χ_n amounts to a Schmidt decomposition or a compact[1] singular value decomposition (SVD) on $\mathbf{\Psi}$.

$$\Psi_{(l_1 \ldots l_n),(l_{n+1} \ldots l_N)} \overset{\text{SVD}}{=\!=} \sum_{i=1}^{\chi_n} \Lambda^n_i \, \psi^{a,n}_{(l_1 \ldots l_n),i} \, \psi^{b,n}_{(l_{n+1} \ldots l_N),i} \tag{A.2}$$

[1] Compact SVD discards singular values that are zero and their corresponding singular vectors

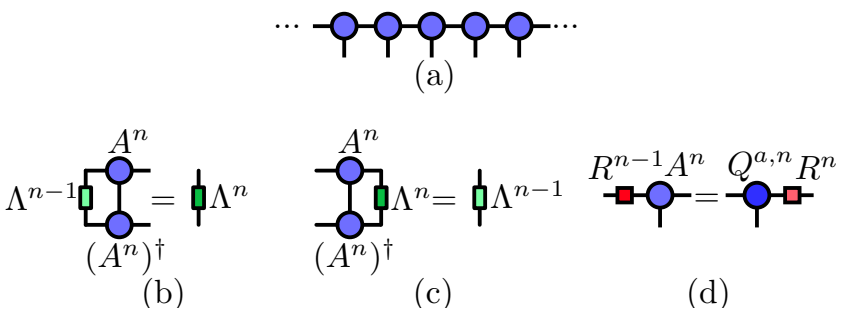

Figure A.1: (a) An MPS (A.1). (b)(c) Canonical conditions for an MPS (A.4). (d) Successive QR decompositions of MPS (A.5).

The most efficient OBC-MPS would have

$$\boldsymbol{\psi}^{a,n}\sqrt{\boldsymbol{\Lambda}^n} = \mathbf{A}^1 \dots \mathbf{A}^n, \quad \sqrt{\boldsymbol{\Lambda}^n}(\boldsymbol{\psi}^{b,n})^\dagger = \mathbf{A}^{n+1} \dots \mathbf{A}^N \tag{A.3}$$

for all $n = 1, \dots, N-1$. This condition can be translated into a more local form of (Fig. A.1b,c)

$$\begin{aligned} \sum_{kl} A^n_{klj}\, \Lambda^{n-1}_k (A^n_{kli})^* &= \delta_{ij}\Lambda^n_i \\ \sum_{kl} A^n_{jlk}\, \Lambda^n_k\, (A^n_{ilk})^* &= \delta_{ij}\Lambda^{n-1}_i \end{aligned} \tag{A.4}$$

for all n, with $\boldsymbol{\Lambda}^0 = \boldsymbol{\Lambda}^N = 1$. This is known as the canonical form MPS.

To transform a general MPS into the canonical form, we first perform successive reduced[2] QR and LQ decompositions (Fig. A.1d)

$$\begin{aligned} \sum_p R^{n-1}_{ip} A^n_{plj} \equiv C^{a,n}_{(il),j} &\overset{\text{QR}}{=\!=} \sum_p Q^{a,n}_{(il),p}\, R^n_{pj}, \\ \sum_p A^n_{ilp}\, L^n_{pj} \equiv C^{b,n}_{i,(lj)} &\overset{\text{LQ}}{=\!=} \sum_p L^{n-1}_{ip} Q^{b,n}_{p,(lj)}, \end{aligned} \tag{A.5}$$

starting from $\mathbf{R}^0 = \mathbf{L}^N = 1$. Next, perform a compact SVD on the matrix $\mathbf{R}^n\mathbf{L}^n = \mathbf{U}^n\boldsymbol{\Lambda}^n(\mathbf{V}^n)^\dagger$, and define "projectors"[3]

$$\mathbf{P}^{a,n} = \mathbf{L}^n\mathbf{V}^n\frac{1}{\sqrt{\boldsymbol{\Lambda}^n}}, \quad \mathbf{P}^{b,n} = \frac{1}{\sqrt{\boldsymbol{\Lambda}^n}}(\mathbf{U}^n)^\dagger\mathbf{R}^n. \tag{A.6}$$

[2]Reduced QR (LQ) decomposition produces square R (L) matrices, and does not compute unnecessary orthogonal vectors in Q.

[3]$\mathbf{P}^{a,n}$ and $\mathbf{P}^{b,n}$ are technically not projectors individually, but $\mathbf{P}^{a,n}\mathbf{P}^{b,n}$ is a projector.

We verify that insertion of the projector $\mathbf{P}^{a,n}\mathbf{P}^{b,n}$ does not change the MPS

$$\begin{aligned}
&\mathbf{\Psi} = (\mathbf{A}^1 \dots \mathbf{A}^n) \cdot (\mathbf{A}^{n+1} \dots \mathbf{A}^N) \\
=&\mathbf{Q}^{a,1} \dots \mathbf{Q}^{a,n}\, \mathbf{U}^n \mathbf{\Lambda}^n (\mathbf{V}^n)^\dagger \mathbf{Q}^{b,n+1} \dots \mathbf{Q}^{b,N} \\
=&\mathbf{Q}^{a,1} \dots \mathbf{Q}^{a,n}\, \mathbf{U}^n \mathbf{\Lambda}^n (\mathbf{V}^n)^\dagger \mathbf{V}^n \frac{1}{\mathbf{\Lambda}^n} (\mathbf{U}^n)^\dagger \mathbf{U}^n \mathbf{\Lambda}^n (\mathbf{V}^n)^\dagger \mathbf{Q}^{b,n+1} \dots \mathbf{Q}^{b,N} \\
=&(\mathbf{Q}^{a,1} \dots \mathbf{Q}^{a,n}\mathbf{R}^n)[\mathbf{L}^n\mathbf{V}^n \frac{1}{\sqrt{\mathbf{\Lambda}^n}}][\frac{1}{\sqrt{\mathbf{\Lambda}^n}}(\mathbf{U}^n)^\dagger \mathbf{R}^n](\mathbf{L}^n \mathbf{Q}^{b,n+1} \dots \mathbf{Q}^{b,N}) \\
=&(\mathbf{A}^1 \dots \mathbf{A}^n)(\mathbf{P}^{a,n}\mathbf{P}^{b,n})(\mathbf{A}^{n+1} \dots \mathbf{A}^N),
\end{aligned} \tag{A.7}$$

Define $\widetilde{\mathbf{A}}^n = \mathbf{P}^{b,n-1}\mathbf{A}^n\mathbf{P}^{a,n}$, and notice that

$$\begin{aligned}
\widetilde{\mathbf{A}}^n =& \frac{1}{\sqrt{\mathbf{\Lambda}^{n-1}}} (\mathbf{U}^{n-1})^\dagger \mathbf{R}^{n-1} \mathbf{A}^n \mathbf{L}^n \mathbf{V}^n \frac{1}{\sqrt{\mathbf{\Lambda}^n}} \\
=& \frac{1}{\sqrt{\mathbf{\Lambda}^{n-1}}} (\mathbf{U}^{n-1})^\dagger \mathbf{Q}^{a,n} \mathbf{R}^n \mathbf{L}^n \mathbf{V}^n \frac{1}{\sqrt{\mathbf{\Lambda}^n}} \\
=& \frac{1}{\sqrt{\mathbf{\Lambda}^{n-1}}} (\mathbf{U}^{n-1})^\dagger \mathbf{Q}^{a,n} \mathbf{U}^n \mathbf{\Lambda}^n (\mathbf{V}^n)^\dagger \mathbf{V}^n \frac{1}{\sqrt{\mathbf{\Lambda}^n}} \\
=& \frac{1}{\sqrt{\mathbf{\Lambda}^{n-1}}} (\mathbf{U}^{n-1})^\dagger \mathbf{Q}^{a,n} \mathbf{U}^n
\end{aligned} \tag{A.8}$$

and similarly

$$\widetilde{\mathbf{A}}^n = (\mathbf{U}^{n-1})^\dagger \mathbf{Q}^{b,n} \mathbf{U}^n \frac{1}{\sqrt{\mathbf{\Lambda}^n}}, \tag{A.9}$$

The canonical conditions (A.4) follow from the orthogonality (unitarity) of $\mathbf{Q}^{a,n}, \mathbf{Q}^{b,n}$ and $\mathbf{U}^n$. Therefore, $(\widetilde{\mathbf{A}}^1 \dots \widetilde{\mathbf{A}}^N)$ is the canonicalization of the original MPS.

By virtual of being an SVD at every bond dimension, the canonical form is not only the most memory efficient form of MPS, but also provides an easy way to find the best approximation with a single reduced bond dimension χ_n, simply by truncating the bond dimension to discard the smallest singular values Λ_i^n. However, the resulting truncated MPS is no long canonical, and further truncations of other bonds yield only suboptimal approximations. But as long as truncation errors (discarded singular values) are relatively small, the MPS should remain close to canonical, and truncating all bonds simultaneously should still yield a very good approximation.

Infinite MPS

An infinite MPS invariant under N-site translation (iMPS) is one with $n \in \mathbb{Z}$ and $\mathbf{A}^n = \mathbf{A}^{n+N}$ for all n in (A.1). Its canonical form is still defined by (A.4). We can obtain the

canonical form following a similar algorithm to the one for OBC-MPS, except we start the successive QR (LQ) decomposition from $\mathbf{R}^n = \mathbf{I}(= \mathbf{L}^n)$ for some n, and normalize all $\mathbf{R}^n$ ($\mathbf{L}^n$) (e.g. by setting the maximum diagonal element to 1). The successive QR (LQ) decompositions stop when convergence is reached, i.e. when $\mathbf{R}^n \approx \mathbf{R}^{n+N}$, $\forall n > M_1$ for some M_1 (and $\mathbf{L}^n \approx \mathbf{L}^{n-N}$, $\forall n < M_2$ for some M_2). The N converged $\mathbf{R}^n$'s and $\mathbf{L}^n$'s are used to construct N projectors $\mathbf{P}^{a,n}\mathbf{P}^{b,n}$ as in (A.6) and define $\widetilde{\mathbf{A}}^n = \mathbf{P}^{b,n-1}\mathbf{A}^n\mathbf{P}^{a,n}$ for all $n \in \mathbb{Z}$.

A good lower-bond-dimension approximation to a canonical iMPS can be obtained similarly by truncating bond dimensions to discard the smallest singular values.

Periodic boundary condition

An N-body MPS with periodic boundary condition (PBC-MPS) has $n = 1, \ldots, N$ and $i_0 \equiv i_N$ in (A.1). It unfortunately does not have a well-defined canonical form, because the two sides of a bond are always connected at the other end, making orthogonality ill-defined.

To find a good approximation to a PBC-MPS with lower bond dimensions, we can use the algorithm of alternating least squares [62]. Given a PBC-MPS $\mathbf{A}^1 \ldots \mathbf{A}^N$ and a suitable initial guess $\mathbf{B}^0 \ldots \mathbf{B}^N$ with $\chi_n^B \leq \chi_n^A$, we want to minimize the cost function $E(\{\mathbf{B}^n\}) = \left\|\mathbf{A}^1 \ldots \mathbf{A}^N - \mathbf{B}^1 \ldots \mathbf{B}^N\right\|^2$. Notice that the cost function $E(\{\mathbf{B}^n\})$ is quadratic in each $\mathbf{B}^n$, and can be minimized exactly with respect to each individual $\mathbf{B}^n$. Specifically, the optimal $\mathbf{B}^m$ (with all other $\mathbf{B}^n$ $(n \neq m)$ fixed) is one such that

$$\frac{\partial E}{\partial \mathbf{B}^m} = 0 \quad \Longrightarrow \quad \mathbf{N}^m\mathbf{B}^m = \mathbf{v}^m, \tag{A.10}$$

where

$$N^m_{(i_{m-1}l_m i_m),(j_{m-1}l_m j_m)} = \sum_{\{i_n\}\{j_n\}\{l_n\}} \Big(\prod_{n\neq m} B^n_{i_{n-1}l_n i_n}\Big)^* \Big(\prod_{n\neq m} B^n_{j_{n-1}l_n j_n}\Big), \tag{A.11a}$$

$$v^m_{j_{m-1}l_m j_m} = \sum_{\{i_n\}\{j_n\}\{l_n\}} \Big(\prod_{n} A^n_{i_{n-1}l_n i_n}\Big)^* \Big(\prod_{n\neq m} B^n_{j_{n-1}l_n j_n}\Big). \tag{A.11b}$$

Once $\mathbf{B}^m$ is optimized, we proceed to optimize $\mathbf{B}^{m+1}$ and so on. Repeat this process iteratively to sweep through all $\mathbf{B}^n$'s multiple times, until the cost function has converged to a small and stable value.

A good initial guess is important to the alternating least squares algorithm. In practice, we found that treating the PBC-MPS as an N-site translation invariant iMPS, and

canonicalize and truncate accordingly, usually produces a good initial guess. Alternatively (sometimes even better), canonicalize the OBC-MPS $(\mathbf{A}^1\mathbf{A}^2\dots\mathbf{A}^N\mathbf{A}^1)$[4], and use the obtained projectors $\mathbf{P}^{a,n}, \mathbf{P}^{b,n}$ to transform and truncate the original PBC-MPS. These pseudo-canonicalization procedures also helps to better condition the matrices $\mathbf{N}^m$'s, and prevent them from being (close to) singular. It is therefore also helpful to occasionally pseudo-canonicalize $\mathbf{B}^n$'s during the iterative optimization (e.g. once every 10 sweeps).

[4]The dangling virtual bond index of $\mathbf{A}^1$ on the two ends are merged into its physical leg.

Appendix B

Calculus of Grassmann tensors

Definition

A general rank-r Grassmann tensor $\mathbf{G}$ takes the form

$$[\mathbf{G}(\boldsymbol{\eta})]^{n_1\dots n_r}_{i_1\dots i_r} = G^{n_1\dots n_r}_{i_1\dots i_r}(\eta_1)^{n_1}\dots(\eta_r)^{n_r} \tag{B.1}$$

where $G^{n_1\dots n_r}_{i_1\dots i_r}$ is a rank-$2r$ complex valued coefficient tensor, $n_a = 0, 1$ are fermionic/Grassmann indices, $i_a = 1, 2, \dots, \chi_a$ are bosonic/spin indices, and η_a's are Grassmann numbers. (We note that n_a's on top of η_a's are exponents, not indices of η_a's.) Grassmann indices and spin indices always come in pairs $p_a = (n_a, i_a)$, so it is useful to think of the pair as a single index of the Grassmann tensor. A Grassmann tensor should have a definite parity. An even (odd) Grassmann tensor have non-zero values only when $\sum_a n_a$ is even (odd). For most of our purposes, including representing physical observables or the evolution operator, only even Grassmann tensors are used.

Contractions

The contraction between the a-th index of a rank-r Grassmann tensor $\mathbf{F}$ and the b-th index of a rank-s Grassmann tensor $\mathbf{G}$ is defined as

$$[\mathbf{F}\cdot\mathbf{G}]^{m_1\dots n_1\dots}_{i_1\dots j_1\dots} \equiv \int g_{\theta_a\eta_b}\sum_{i_a,j_b}\delta_{i_a j_b}[\mathbf{F}(\boldsymbol{\theta})]^{m_1\dots m_a\dots m_r}_{i_1\dots i_a\dots i_r}[\mathbf{G}(\boldsymbol{\eta})]^{n_1\dots n_b\dots n_s}_{j_1\dots j_b\dots j_s} \tag{B.2}$$

Fig. B.1a shows the diagrammatic representation of the contraction, where each bond has two lines each representing Grassmann index and spin index, and the arrow indicates the

Figure B.1: (a) Contraction between two general Grassmann tensors. Red/black lines denote Grassmann/spin indices. The arrow indicates the order/sign of the metric. (b) Contraction between a Grassmann tensor and its conjugate.

order of contraction as reflected in the Grassmann metric $g_{\theta_a \eta_b}$. The contraction can be simplified significantly when it is between the last index of the first tensor and the first index of the second tensor (i.e. $a = r, b = 1$)

$$[\mathbf{F} \cdot \mathbf{G}]^{m_1 \ldots m_{r-1}\, n_2 \ldots n_s}_{i_1 \ldots i_{r-1}\, j_2 \ldots j_s} = \sum_{m' i'} F^{m_1 \ldots m_{r-1}\, m'}_{i_1 \ldots i_{r-1}\, i'} G^{m' n_2 \ldots n_s}_{i' j_2 \ldots j_s} \prod_{a=1}^{r-1} (\theta_a)^{m_a} \prod_{b=2}^{s} (\eta_b)^{n_b}. \tag{B.3}$$

This property makes Grassmann tensor contractions very tractable in practice. All we need to do is to permute indices and Grassmann numbers so that indices to be contracted are correctly positioned, then we can contract two Grassmann tensors as if they are just normal complex-valued tensors. Sign changes only happen internally to each Grassmann tensor when permuting indices.

Decomposition

Matrix decompositions of an even Grassmann tensor $\mathbf{G}$ are defined by the requirement that they should be compatible with contractions. There are, in general, four steps

1. Permute indices and Grassmann numbers so that they are separated into two groups $I \equiv \binom{n_1 \ldots n_a}{i_1 \ldots i_a}$ and $J \equiv \binom{n_{a+1} \ldots n_r}{i_{a+1} \ldots i_r}$. Treat each index group as a large individual index, effectively turning the complex coefficient tensor $G^{n_1 \ldots n_r}_{i_1 \ldots i_r}$ into a matrix G_{IJ}. This is the only step that involves sign changes.

2. Divide the coefficient tensor/matrix into an even block and an odd block $G = G_e \oplus G_o$, such that the sum of Grassmann indices in each index group I and J is even (odd) in the even (odd) block.

3. Perform normal matrix decomposition on each block of the coefficient tensor/matrix $[G_e]_{IJ} = \sum_j [A_e]_{Ij} [B_e]_{jJ}$ and $[G_o]_{IJ} = \sum_j [A_o]_{Ij} [B_o]_{jJ}$.

4. Define Grassmann tensors $\mathbf{A}$ and $\mathbf{B}$ so that their coefficient tensors are

$$A^{n_1\ldots n_a 0}_{i_1\ldots i_a\, j} = [A_e]_{Ij}, \quad B^{0\, n_{a+1}\ldots n_r}_{j\, i_{a+1}\ldots i_r} = [B_e]_{jJ}, \tag{B.4}$$

$$A^{n_1\ldots n_a 1}_{i_1\ldots i_a\, j} = [A_o]_{Ij}, \quad B^{1\, n_{a+1}\ldots n_r}_{j\, i_{a+1}\ldots i_r} = [B_o]_{jJ}. \tag{B.5}$$

Both $\mathbf{A}$ and $\mathbf{B}$ are even Grassmann tensors, and they satisfy $\mathbf{A}\cdot\mathbf{B} = \mathbf{G}$.

As two important examples, the Grassmann-SVD (GSVD, first introduced in [27]) of a Grassmann tensor that splits between the a-th and the $(a+1)$-th indices $\mathbf{G} = \mathbf{U}\cdot\mathbf{s}\cdot\mathbf{V}$ is defined by

$$G^{\binom{n_1\ldots n_a}{i_1\ldots i_a}\binom{n_{a+1}\ldots n_r}{i_{a+1}\ldots i_r}} \overset{\text{SVD}}{=\!=} \sum_j U^{n_1\ldots n_a,0}_{i_1\ldots i_a,j} s^{00}_{jj} V^{0,n_{a+1}\ldots n_r}_{j,i_{a+1}\ldots i_r} \text{ for } \sum_{b=1}^{a} n_b = \sum_{b=a+1}^{r} n_b = 0 \bmod 2, \tag{B.6a}$$

$$G^{\binom{n_1\ldots n_a}{i_1\ldots i_a}\binom{n_{a+1}\ldots n_r}{i_{a+1}\ldots i_r}} \overset{\text{SVD}}{=\!=} \sum_j U^{n_1\ldots n_a,1}_{i_1\ldots i_a,j} s^{11}_{jj} V^{1,n_{a+1}\ldots n_r}_{j,i_{a+1}\ldots i_r} \text{ for } \sum_{b=1}^{a} n_b = \sum_{b=a+1}^{r} n_b = 1 \bmod 2; \tag{B.6b}$$

and the Grassmann-QR decomposition $\mathbf{G} = \mathbf{Q}\cdot\mathbf{R}$ is defined by

$$G^{\binom{n_1\ldots n_a}{i_1\ldots i_a}\binom{n_{a+1}\ldots n_r}{i_{a+1}\ldots i_r}} \overset{\text{QR}}{=\!=} \sum_j Q^{n_1\ldots n_a,0}_{i_1\ldots i_a,j} R^{0,n_{a+1}\ldots n_r}_{j,i_{a+1}\ldots i_r} \text{ for } \sum_{b=1}^{a} n_b = \sum_{b=a+1}^{r} n_b = 0 \bmod 2, \tag{B.7a}$$

$$G^{\binom{n_1\ldots n_a}{i_1\ldots i_a}\binom{n_{a+1}\ldots n_r}{i_{a+1}\ldots i_r}} \overset{\text{QR}}{=\!=} \sum_j Q^{n_1\ldots n_a,1}_{i_1\ldots i_a,j} R^{1,n_{a+1}\ldots n_r}_{j,i_{a+1}\ldots i_r} \text{ for } \sum_{b=1}^{a} n_b = \sum_{b=a+1}^{r} n_b = 1 \bmod 2. \tag{B.7b}$$

Conjugation

The conjugate of a Grassmann tensor is defined as

$$[\mathbf{G}^\dagger]^{n_1\ldots n_r}_{i_1\ldots i_r} \equiv (G^{n_1\ldots n_r}_{i_1\ldots i_r})^* (\bar{\eta}_r)^{n_r} \ldots (\bar{\eta}_1)^{n_1}, \tag{B.8}$$

so that the full contraction between $\mathbf{G}$ and $\mathbf{G}^\dagger$ (Fig. B.1b) gives the 2-norm

$$\mathbf{G}^\dagger\cdot\mathbf{G} = \sum_{\{n_a\}\{i_a\}} \left|G^{n_1\ldots n_r}_{i_1\ldots i_a}\right|^2. \tag{B.9}$$

Appendix C

Group cohomology and bosonic SPT phases

C.1 Algebraic definition of group cohomology

For a group G, a G-module M is itself an Abelian group on which the group G acts compatibly with its Abelian group structure, i.e.

$$g \cdot (ab) = (g \cdot a)(g \cdot b), \quad \forall g \in G, \quad \forall a, b \in M. \tag{C.1}$$

Define a n-cochain as a map $\nu_n : G^{n+1} \to M$ that satisfies[1]

$$g \cdot \nu_n(g_0, g_1, \ldots, g_n) = \nu_n(gg_0, gg_1, \ldots, gg_n). \tag{C.2}$$

The set of all n-cochains forms a group, denoted as $\mathcal{C}^n(G, M)$, whose group multiplication is simply the function multiplication of ν_n.

Define the coboundary operator as a map

$$\begin{aligned} d_n : \mathcal{C}^n(G, M) \quad &\to \quad \mathcal{C}^{n+1}(G, M) \\ (d_n\nu_n)(g_0, \ldots, g_n) &= \prod_{i=0}^{n+1} \nu^{(-1)^i}(g_0, \ldots, g_{i-1}, g_{i+1}, \ldots, g_n) \end{aligned} \tag{C.3}$$

[1] It is common to define n-cochains as an arbitrary function from G^n to M. Our definition involves one more group element and an constraint on the function, and is essentially equivalent. Such a definition, although with redundancy, allows more convenient definitions and intuitive geometric interpretations of many of the algebraic objects defined later.

An n-cochain ν_n is called an n-coboundary if $\nu_n = d_{n-1}\nu_{n-1}$ for some $\nu_{n-1} \in \mathcal{C}^{n-1}(G, M)$. It is called an n-cocycle if $d_n\nu_n = 1$. The set of all n-coboundaries $\mathcal{B}(G, M)$ and the set of all n-cocycles $\mathcal{Z}_n(G, M)$ form two subgroups of $\mathcal{C}^n(G, M)$, where we define $B^0(G, M) = 0$ in addition. More formally, we have

$$\mathcal{B}^n(G, M) = \begin{cases} 1, & n = 0; \\ d_{n-1}(\mathcal{C}^{n-1}(G, M)), & n \geq 1. \end{cases} \tag{C.4}$$

$$\mathcal{Z}^n(G, M) = \ker(d_n). \tag{C.5}$$

Finally, we define the group cohomology of (G, M) as the quotient group

$$\mathcal{H}^n(G, M) = \mathcal{Z}^n(G, M) \,/\, \mathcal{B}^n(G, M). \tag{C.6}$$

For our purposes, it is sufficient to consider $M = U(1)$ whose elements are simply phase factors, and G is the symmetry group of the system. G acts on $U(1)$ in the following way:

$$g \cdot a = a^{s(g)}, \quad \forall g \in G, \quad \forall a \in M, \tag{C.7}$$

where

$$s(g) = \begin{cases} 1, & \text{if } g \in G \text{ acts unitarily;} \\ -1, & \text{if } g \in G \text{ acts anti-unitarily.} \end{cases} \tag{C.8}$$

To explicitly indicate this nontrivial action of anti-unitary group elements, we shall from now on write $M = U_T(1)$.

C.2 Constructing bosonic SPT phases using group cohomology

Bosonic SPT phases can be systematically described by group cohomology theory [11]. Specifically, $(d+1)$-dimensional bosonic SPT phases with symmetry group G can be labeled by elements in $\mathcal{H}^{d+1}[G, U_T(1)]$. The identity element corresponds to a trivial phase (product state), and nontrivial elements correspond to nontrivial SPT phases.

Furthermore, we can construct exactly solvable lattice models of SPT phases for any finite symmetry group G and in any dimensions. Such a model is constructed on a d-dimensional simplicial complex M, which is itself the boundary of an extended $(d+1)$-dimensional complex M_{ext} with a branching structure, and we further assume that there

is only one internal vertex in M_{ext}. Each vertex in M is associated with a $|G|$-dimensional local Hilbert space, where basis vectors $|g_i\rangle$ are labeled by group elements $g_i \in G$. The internal vertex of M_{ext} is associated with a fixed group element $g^* \in G$. The ground state wave function is given by (Fig. C.1)

$$|\Psi_M\rangle = \sum_{\{g_i\}_M} \prod_{\{ij\cdots *\}} \nu_{d+1}^{s_{ij\cdots *}}(g_i, g_j, \ldots, g^*) \, |\{g_i\}_M\rangle \tag{C.9}$$

where the sum runs over all configurations $\{g_i\}_M$ of the vertices in M and the product runs over all simplices $\{ij\cdots *\}$ in M_{ext}, and ν_{d+1} is a group $(d+1)$-cocycle. The symmetry is on-site and acts in the following simple way:

$$g : |\{g_i\}_M\rangle \to |\{gg_i\}_M\rangle \, , \quad g \in G \tag{C.10}$$

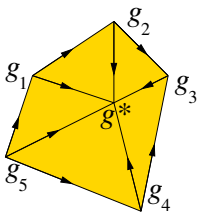

Figure C.1: The graphical representation of the ground state wave function (C.9) in the case of $d = 1$. The edge is M and the disk is M_{ext}.

The ground state is trivial a product state when the cocycle is trivial. Nontrivial ground states can be obtained from this trivial state by a unitary transformation

$$U = \prod_{\{ij\cdots *\}} \nu_{d+1}^{s_{ij\cdots *}}(g_i, g_j, \ldots, g^*) \tag{C.11}$$

An exactly solvable Hamiltonian can be constructed for this ground state as

$$H = -\sum_i H_i, \quad H_i = U|\phi_i\rangle\langle\phi_i|U^\dagger \tag{C.12}$$

where the sum runs over all vertices i and $|\phi_i\rangle = \sum_{g_i \in G} |g_i\rangle$. It is straightforward to check that all H_i's commute with each other, hence the solvability of this model.

In 2D, an explicit formula is given by (Fig. C.2):

$$\begin{aligned} &\langle g_i', g_1g_2g_3g_4g_5g_6|H_i|g_i, g_1g_2g_3g_4g_5g_6\rangle \\ =&\frac{\nu_3(g_4, g_5, g_i, g_i')\nu_3(g_5, g_i, g_i', g_6)\nu_3(g_i, g_i', g_6, g_1)}{\nu_3(g_i, g_i', g_2, g_1)\nu_3(g_3, g_i, g_i', g_2)\nu_3(g_4, g_3, g_i, g_i')} \end{aligned} \tag{C.13}$$

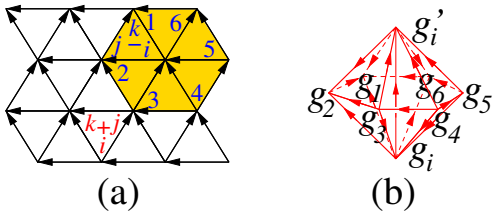

Figure C.2: A lattice model for 2-dimensional SPT phase. (a) H_i acts on seven spins centered around i, shown as the shaded region. Down triangles $\triangledown$ have orientation $s_{ijk} = +$, and up triangles $\triangle$ have orientation $s_{ijk} = -$. (b) A graphical representation of the phase factor, which is a product of 3-cocycles. The "internal" vertex associated with g^* was originally in the centre of the cage, but can be removed using cocycle condition (either graphically or algebraically).

For $G = \mathbb{Z}_2$, there are two elements in $\mathcal{H}^3[\mathbb{Z}_2, U_T(1)]$, corresponding to the two Hamiltonians defined by (3.12).

Finally, we note that elements in the group cohomology are equivalence classes. Two different cocycles ν_n and ν_n' describe the same SPT phase if they differ only by a coboundary:

$$\nu_n(g_0, g_1, \ldots, g_n) = (d_{n-1}\nu_{n-1})(g_0, g_1, \ldots, g_n) \cdot \nu_n'(g_0, g_1, \ldots, g_n) \tag{C.14}$$

The choice of the branching structure is also irrelevant in the classification of SPT phases, so we can always choose any branching structure that is most convenient for our purpose.

Appendix D

Energy spectrum of Luttinger liquid theory

In this appendix, we derive the energy spectrum (3.42) for the $c = 1$ Luttinger liquid theory whose action is given in Eq. (3.40). For convenience, we repeat the action here

$$S_{\text{edge}} = \frac{1}{4\pi} \int dt dx \left(K_{IJ} \partial_t \phi_I \partial_x \phi_J - V_{IJ} \partial_x \phi_I \partial_x \phi_J \right) \tag{D.1}$$

where ϕ_I is a compact boson with $\phi_I = \phi_I + 2\pi$. As discussed in the main text, we only need to consider the $c = 1$ two-component theory associated with

$$K = \begin{pmatrix} 0 & 1 \\ 1 & 0 \end{pmatrix}, \quad V = \begin{pmatrix} a & c \\ c & b \end{pmatrix} \tag{D.2}$$

where a, b, c are real numbers satisfying the conditions $a > 0$ and $ab > c^2$ such that V is positive definite. This is a free theory and it is well studied in the literature (see e.g. [21]). To be self-contained, we give a brief derivation on the relevant results used in the main text, with a focus on the case that the left and right movers have *different* velocities.

To find the spectrum, we perform the following change of variables:

$$\tilde{\phi} = U^{-1} \phi \tag{D.3}$$

where $\phi = (\phi_1, \phi_2)$ and

$$U = \frac{1}{\sqrt{2}} \begin{pmatrix} \rho & -\rho \\ 1/\rho & 1/\rho \end{pmatrix} \tag{D.4}$$

with $\rho = \sqrt[4]{b/a}$. Inserting (D.3) into (D.1), the action is rewritten as

$$S_{\text{edge}} = \frac{1}{4\pi}\int dtdx\ \partial_x\tilde{\phi}_1\left(\partial_t\tilde{\phi}_1 - v_1\partial_x\tilde{\phi}_1\right) - \frac{1}{4\pi}\int dtdx\ \partial_x\tilde{\phi}_2\left(\partial_t\tilde{\phi}_2 + v_2\partial_x\tilde{\phi}_2\right) \tag{D.5}$$

where $v_1 = \sqrt{ab} + c$ and $v_2 = \sqrt{ab} - c$. The two fields $\tilde{\phi}_1$ and $\tilde{\phi}_2$ completely decouple, each of which is a standard free chiral boson. The theory (D.5) can then be solved using the standard mode expansion; see e.g. [21]. Below we briefly state the main results.

The energy eigenstates consist of two types. First, there is a set of highest weight states, created by the corresponding vertex operators when acting on the ground state. This energy of these states depend on the compactification radii of the fields $\tilde{\phi}_1$ and $\tilde{\phi}_2$, which inherit from those of ϕ_1 and ϕ_2. In the current case that $\phi_I = \phi_I + 2\pi$, the general form of vertex operators are given by

$$V_{m,n} = e^{im\phi_1 + in\phi_2} \tag{D.6}$$

where m, n are integers. Acting $V_{m,n}$ on the ground state $|0\rangle$, it creates a highest weight state $|m,n\rangle \equiv V_{m,n}|0\rangle$. These states are the primary states of the $U(1)$ Kac-Moody algebra that one can read off from the action S_{edge}. We rewrite $V_{m,n} = e^{i\tilde{m}\tilde{\phi}_1 + i\tilde{n}\tilde{\phi}_2}$, where

$$\tilde{m} = \frac{1}{\sqrt{2}}(m\rho + n/\rho), \quad \tilde{n} = \frac{1}{\sqrt{2}}(-m\rho + n/\rho) \tag{D.7}$$

The energy of the state $|m,n\rangle$ (relative to the ground state) is given by

$$\begin{aligned}\Delta_{m,n} &= \frac{\pi v_1}{L}\tilde{m}^2 + \frac{\pi v_2}{L}\tilde{n}^2 \\ &= \frac{\pi(v_1+v_2)}{L}\left[\frac{1}{2}\left(\rho^2 m^2 + \frac{n^2}{\rho^2}\right) + \frac{1-v_r}{1+v_r}mn\right]\end{aligned} \tag{D.8}$$

where L is the system size and $v_r = v_2/v_1$.

Second, in the mode expansion of the fields $\tilde{\phi}_1$ and $\tilde{\phi}_2$, one introduces the Fourier coefficients $\tilde{a}_{1,l}$ and $\tilde{a}_{2,l}$, where l is integer. The highest weight states are annihilated by $\tilde{a}_{1,l}$ and $\tilde{a}_{2,l}$ with $l > 0$, i.e., $\tilde{a}_{1,l}|m,n\rangle = \tilde{a}_{2,l}|m,n\rangle = 0$. On the other hand, a Fork space is spanned by acting $\tilde{a}_{1,l}$ and $\tilde{a}_{2,l}$ with $l < 0$ on each primary state $|m,n\rangle$:

$$\tilde{a}_{1,-1}^{n_{1,1}}\tilde{a}_{1,-2}^{n_{1,2}}\ldots\tilde{a}_{2,-1}^{n_{2,1}}\tilde{a}_{2,-2}^{n_{2,2}}\ldots|m,n\rangle \tag{D.9}$$

where $n_{1,l}$ and $n_{2,l}$ are positive integers. The energy of these descendant states are

$$\begin{aligned}\Delta_{m,n,\{n_{1,l},n_{2,l}\}} &= \Delta_{m,n} + \sum_{l=1}^{\infty}\left(\frac{2\pi v_1 l}{L}n_{1,l} + \frac{2\pi v_2 l}{L}n_{2,l}\right) \\ &= \Delta_{m,n} + \frac{\pi(v_1+v_2)}{L}\frac{2}{1+v_r}\sum_{l=1}^{\infty} l(n_{1,l} + v_r n_{2,l}) \end{aligned} \tag{D.10}$$

Then, the whole spectrum is generated by varying the integers m, n, and $\{n_{1,l}, n_{2,l}\}$.

Finally, we comment that the ground state energy also depends on the system size L. For periodic boundary conditions, the ground state energy is given by

$$E_0 = -\frac{\pi c}{12L}(v_1 + v_2) \tag{D.11}$$

where c is the central charge. Since $c = 1$, Eq. (D.11) can be used to set the energy unit $\pi(v_1 + v_2)/L$ in numerical calculations.